ABSTRACT

Title of dissertation: STRUCTURE AND PROPERTIES OF ALLOYED CHALCOGENIDES WITH THE $ThCr_2Si_2$ TYPE STRUCTURE

Austin Virtue
Doctor of Philosophy, 2019

Dissertation directed by: Professor Efrain E. Rodriguez
Department of Chemistry and Biochemistry

The $ThCr_2Si_2$-type structure has proven itself to be an incredibly robust structure type. Its ability to incorporate elements from the majority of the periodic table has earned it the moniker of "The perovskite of intermetallics". This layered structural motif has the nominal formula of AM_2X_2, where typically, A is an electropositive atom, M is a transition metal, and X is a main group element. They are ordered as a layered structure of layers of two-dimensional MX_4^{n-} edge sharing tetrahedra separated by layers of A^{n+} cations. The wide variety of different compounds that have been characterized with this structure has resulted in almost as wide a variety of properties, including superconductivity.

This dissertation demonstrates the affects that having a mixed metal site has on the properties of these compounds. Powder and single crystal samples are prepared for a series of compounds so that these effects can be compared for different X atom chalcogenides. We demonstrate that increasing the bond distances through changing the X atom from sulfur to selenium has a pronounced effect on the mag-

netic and electrical properties. Possible magnetic structures for $KCuMnS_2$ are proposed for the first time. Different methods at tuning the structure to obtain new compounds are discussed.

Structure and Properties of Alloyed Chalcogenides with the $ThCr_2Si_2$ Type Structure

by

Austin Virtue

Dissertation submitted to the Faculty of the Graduate School of the
University of Maryland, College Park in partial fulfillment
of the requirements for the degree of
Doctor of Philosophy
2019

Advisory Committee:
Professor Efrain E. Rodriguez, Chair/Advisor
Professor Bryan Eichhorn
Professor Nicholas Butch
Professor Johnpierre Paglione
Professor Andrei Vedernikov

Dedication

To all of my friends who have seen me through this grad school journey. I should probably include family and coworkers, but I feel that that would just be redundant.

Acknowledgments

I would like to thank my adviser Professor Efrain Rodriguez for everything he has done to help me understand solid state chemistry. I would also like to thank my other committee members, Professors Byran Eichhorn, Andrei Vedernikov, Nicholas Butch, and Johnpierre Paglione for their time in reviewing this manuscript. I would like to thank all the current and former members of the Rodriguez group, particularly Dr. Xiuquan Zhou and Brandon Wilfong, for all of their help with the various physical properties measurements performed at the Center for Nanophysics and Advanced Materials (CNAM) for our various collaborations over the years.

I would like to thank Dr. Peter Zavalij for all of his assistance in the X-ray crystallography center here at the University of Maryland, and allowing me to work there as the small angle X-ray scattering assistant, even when there was low demand for it. I would like to thank Drs. Craig Brown and Jeff Lynn for showing me around and helping me out at the National Institute of Standards and Technology (NIST) Center for Neutron Research (NCNR). I would like to thank Dr. Keith Taddei for all the help he provided while collecting data at the HB-2A High Flux Isotope Reactor (HFIR) at Oak Ridge National Lab (ORNL), particularly with working around a temperamental heating coil.

Research at the University of Maryland was supported by the NSF Career DMR-1455118, and the Department of Commerce under the NIST award 70NANB12H238. We also acknowledge support from the Maryland Nanocenter and Center for Nanophysics and Advanced Materials. I would like to acknowledge the support of the National

Institute of Standards and Technology, U. S. Department of Commerce, in providing the neutron research facilities used in this work. The part of the research that was conducted at ORNLs High Flux Isotope Reactor was sponsored by the Scientific User Facilities Division, Office of Basic Energy Sciences, US Department of Energy. I would also like to acknowledge the University of Maryland supercomputing resources made available for conducting the research reported in this work.

Finally, I need to thank all of my family for their support of me working so far away for so long. With only a little bit of nagging me to come back.

Table of Contents

List of Tables

List of Figures

List of Abbreviations

χ	magnetic susceptibility
λ	wavelength
μ_B	Bohr magneton
θ	angle of diffraction
AFM	antiferromagnetic
Ch	chalcogenide
CNAM	the Center for Nanophysics and Advanced Materials
DOS	density of state
DFT	density functional theory
FC	field cooled
FM	ferromagnetic
HFIR	High Flux Isotope Reactor
MPMS	magnetic properties measurement system
MACS	Multi Axis Crystal Spectrometer
NIST	National Institute of Standards and Technology
NCNR	NIST Center for Neutron Research
NPD	neutron powder diffraction
ORNL	Oak Ridge National Laboratory
PAW	projector augmented wave
Pn	pnictide
PPMS	physical property measurement system
PXRD	powder X-ray diffraction
Q	scattering vector
SPINS	Spin Polarized Inelastic Neutron Spectrometer
T_C	Curie temperature
T_N	Néel temperature
UMD	University of Maryland
VASP	Vienna Abinitio Simulation Package
ZFC	zero field-cooled

Chapter 1: Introduction

The discovery of superconductivity in $LaO_{1-x}F_xFeAs$ (x = 0.05-0.12) [1] in 2008 was the dawn of a new age in the research of metal pnictides and chalcogenides. More specifically, it launched a wave of new research into the tetrahedral FeX_4 structure motif possessing superconductivity, where X is a pnictide or a chalcogenide. These include the ZrCuSiAs structure (of which the parent compound LaOFeAs is a member), [1–20] the PbFCl structure type (where AFeAs, A = Li, Na, is a parent compound), [21–23] the PbO structure (where a parent compound is β-FeCh), [24,25] and finally the $ThCr_2Si_2$-type structure (with $BaFe_2As_2$ as a primary parent compound) [20,26–30]. This wide range of study has revealed some similarities between these structure types. These structures are all tetragonal, though some compounds have been shown to undergo a tetragonal to orthorhombic transition at low temperatures. [3–5,22,25,29] Modifications through electron or hole doping can suppress this transition along with the possibly associated antiferromagnetism and promote superconductivity, if not already present. [1,6–19,21,24,25,27,28,30] This work focuses on the $ThCr_2Si_2$-type structure, and the various properties that arise from the MX_4 structural motif, when the M position is jointly occupied by more than one element.

1.1 122 compounds

The number of 122 compounds that have the $ThCr_2Si_2$-type structure are legion. Since the characterization of $ThCr_2Si_2$ in 1965, the list of compounds that share its structure has grown tremendously. [31] While there are numerous compounds that share this structure, their properties are incredibly varied. An immense amount of thought has gone into the different aspects of these materials. So many different compounds sharing the same structure has necessitated general reviews of the overall crystal structure. [32,33] In 1985, the general bonding of 122 compounds was discussed by Hoffmann and Zheng, generally with respect to the pnictides known at the time. [34] Others have gone on to review the electronic structures of these 122, $ThCr_2Si_2$-type compounds, [35, 36] as well as the thermoelectric, [37] or the various magnetic properties that these compounds can exhibit. [38–40] This is all without including the most interesting property of all that these compounds can poses, superconductivity. [41–44]

As the name of this family of $ThCr_2Si_2$-type compounds might suggest, there are three distinct sites in this structure type, those occupied by the thorium, chromium, and silicon. The root cause for this wide variety of properties that this one structure-type can exhibit is pretty clear. Each of these sites can be occupied by a number of different elements to the point where mixing and matching all of the possibilities leads to a staggering amount of compounds. A list compiled by Shatruk this year, even an admittedly incomplete one, contains roughly 700 different compounds with this structure type composed from elements, as Figure 1.1 shows, from all over the

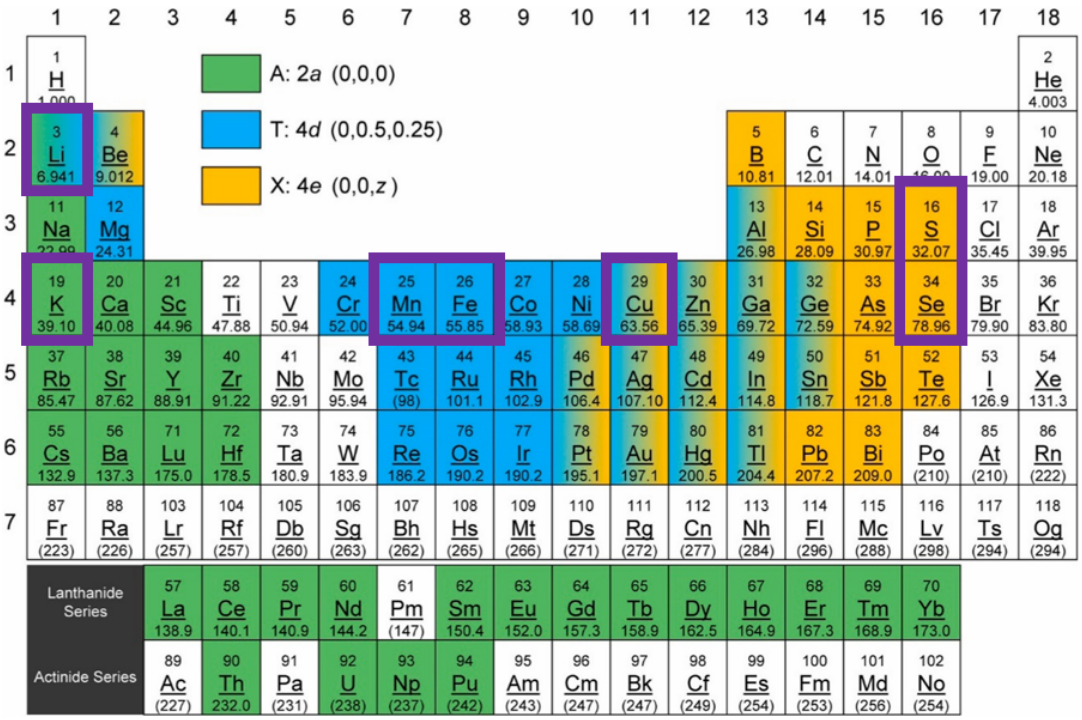

Figure 1.1: The periodic table of $ThCr_2Si_2$-type structures, showing the elements known to occupy the $2a$ (Th), $4d$ (Cr), and $4e$ (Si) positions of the space group $I4/mmm$. The mixed color of an element indicates that it has been observed to occupy one of two of these sites, depending on the compound. The primary elements discussed in this work are outlined in purple. Modified from reference [45]

periodic table. [45] With all of these possibilities to chose from, it was necessary to limit the scope of this work to only the elements outlined in Figure 1.1 of lithium, potassium, manganese, iron, copper, sulfur, and selenium. Though the possibility of expansion is an exciting one.

1.2 122 crystal structure

As stated before, there are three different sites in the $ThCr_2Si_2$-type structure. The overall structure is actually identical of that of $BaAl_4$, if one does not take into account the two different crystallographic sites of Al in this compound. [46] When one does differentiate between these sites, for example, occupying one with Cr, and the other with Si, (and if the Ba was replaced by Th) you end up with a crystal structure inherently different from the original $BaAl_4$, and which is now know as the $ThCr_2Si_2$-type structure. There are a few different types of notation for this structure and its components, such as the $ThCr_2Si_2$-type structure, or the 122-type structure. AT_2X_2, or AM_2X_2, is a general notation used for this series of compounds where A is an electropositive atom, M is a transition metal, and X is a main-group element. Crystallographically, they occupy the $2a$, $4d$, and $4e$ Wyckoff positions of the $I4/mmm$ (No. 139) space group.

There are multiple ways to conceptually think about this crystal structure. One is that it is comprised of layers of MX_4 edge-sharing tetrahedra extending in the ab-plane separated by layers of the A cation along the c-axis. The bonding between these two layers appears largely ionic. [34] Another is that it is comprised of a series of square lattices of A, M, and X layered X-(-A-X-M-X-)-A. Figure 1.2 shows this structure as these MX_4 tetrahedra, and highlights these square lattices, showing the structure along the a axis (left), and c axis (middle and right). It should be noted, that the X position forms two square lattices on opposite sides of the tetrahedra, and that they are aligned along the c-axis with the A cation square

lattice on the opposite side of the tetrahedra layer.

This ionic bonding between the A cation and the MX_4 edge-sharing tetrahedra layers helps to make this structure type so robust. The charge balancing that occurs between these layers allows for a large number of combinations and oxidation states, be they $M_2X_2^{2-}$ and A^{2+} layers, or $M_2X_2^{1-}$ and A^{1+}. Specifically for this work, we are holding the A cation to be A^{1+}, necessitating a $M_2X_2^{1-}$ layer. When $X = Ch$, the average oxidation state of the M site needs to be +1.5. This can be from a single metal with an average oxidation state of +1.5, or from two distinct metals where one has an oxidation state of +1, with the other possessing an oxidation state of +2. This latter situation is what this work will focus on. While there are a number of examples of a mixed metal site in literature, of particular interest for this work is a series of papers from Greenblatt. [39, 47–51]

It is important to note that while the conventional naming scheme has electropositive, transition metal, and main-group elements, the mixed color of some elements in Figure 1.1 indicates that those elements will occupy different sites depending on the compound. It has demonstrated that where an element is located in the 122-type structure is primarily influenced by electronegativities. [52–55] The compound $CaZn_2Al_2$, has what is described as "inverted" positioning of the Zn and Al. [54] For this work, only the conventional distribution of atoms is obtained even though lithium, and copper have been known to occupy multiple sites, using potassium as the electropositive atom, and an electronegative chalcogen as the main-group element, dictates their positioning in the structure. Copper for example is only know to occupy the 4e site when paired with electropositive main-group

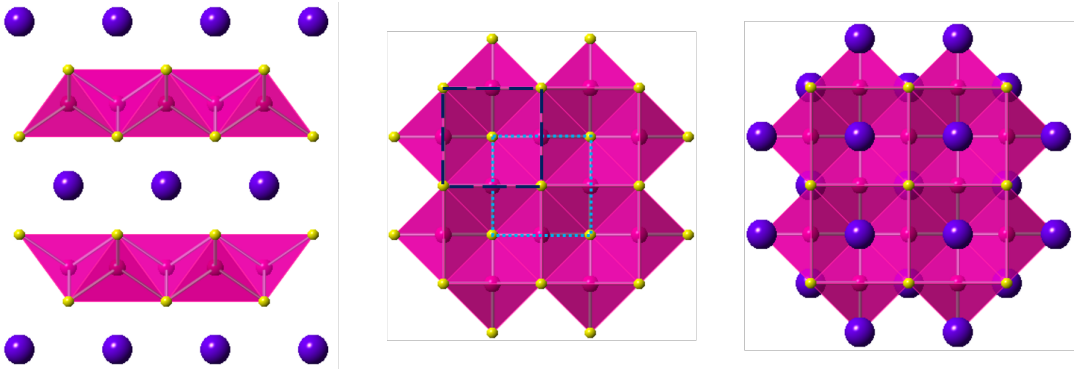

Figure 1.2: Crystal structure of the $ThCr_2Si_2$-type system. The Th position is in purple, the Cr position is in magenta, and the Si position is in yellow. Viewed along the a direction (left), and along the c direction with (center) and without (right) the Th position. The Si positions form two square lattices above and below the Cr position square lattice indicated by the light blue short dashed square, and the dark blue long dashed square (center). The Th position also forms two square lattices superimposed on the Si positions, but on the opposite side of the Cr plane (left).

elements such as aluminum. [55]

While the focus of this work is on the $ThCr_2Si_2$-type structure, that does not necessarily mean that the compounds discussed herein will remain that structure. Some 122-type compounds can undergo structural phase transitions, sometimes retaining a compressed $ThCr_2Si_2$-type structure, sometimes becoming orthorhombic. The layered nature of these compounds makes them inherently susceptible to compressability. Huhnt *etal*. demonstrated that compressing $SrRh_2P_2$ along the c-axis by 6GPa decreased the c-axis by 14.6% while increasing the a-axis by 4.1%. [56] This reduced the interlayer P-P distance from 3.284 Åto an estimated 2.227 Å, which is about the size of a single P-P bond. There can also be a structural phase

transition brought about through temperature. AFe$_2$As$_2$ undergoes an orthorhombic distortion to the F_{mmm} space group upon cooling. [29, 57–59] Compression of BaFe$_2$As$_2$ above 20 GPa not only causes an orthorhombic collapse the structure, but also suppresses the antiferromagnetic (AFM) ordering of the Fe moments. [60]

An additional variable in the composition of these compounds is non-stoichiometry. First reported for ACu$_1$.75P$_2$, the ThCr$_2$Si$_2$-type structure is capable of handling rather large amounts of vacancies in the right situations. [61] It is proposed that the structural stability of the compound is actually helped in certain cases by the vacancies removing valence electrons weakening the $M - X$ bonding, but strengthening the $X - X$ bonding. [62] In the case of the iron-122 compounds, non-stoichiometry leading to electron or hole doping can lead to very interesting properties, namely, superconductivity.

1.3 Superconductivity and magnetic ordering in the 122-type system

While the largest family of high-temperature superconductors remains the superconducting cuprates after their discovery in 1986, [63] the family of high temperature iron superconductors is the steadily growing as the second largest. Along the famous example of those based off of LaOFeAs, [1, 7, 64] are a number of high temperature superconductors based on BaFe$_2$As$_2$, [26–28] and FeSe. [24] Noticably for this work, BaFe$_2$As$_2$ has the ThCr$_2$Si$_2$-type structure. So does the superconducting cuprate LiCu$_2$P$_2$. [65] While it is possible to achieve superconductivity through hole doping of the BaFe$_2$As$_2$ system, [26, 27] it is also possible to achieve superconduc-

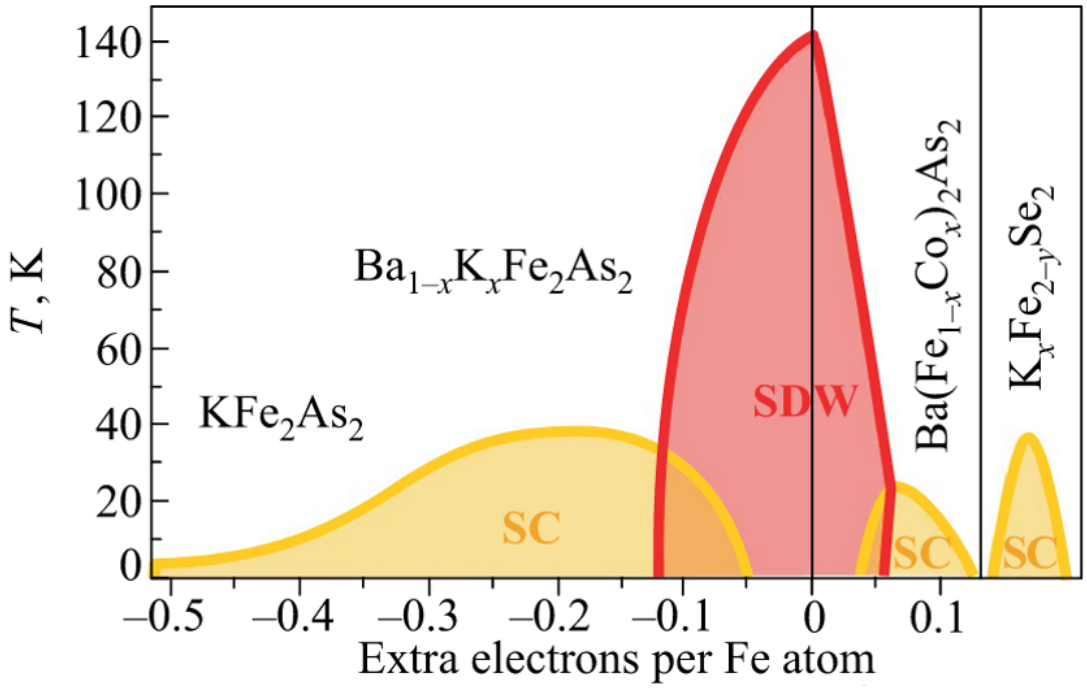

Figure 1.3: General phase diagram for $BaFe_2As_2$ with either electron or hole doping in the form of $Ba_{1-x}K_xFe_2As_2$ and $BaFe_{2-x}Co_xAs_2$. Modified from reference [67]

tivity through electron doping as well, such as for $BaFe_{2-x}Co_xAs_2$. [28] A 122-type superconductor can also be achieved using FeSe as a parent compound. Though it originally has the PbO type structure, intercalation of potassium between the layers of FeSe, creates a KFe_2Se_2 parent 122-type system, where superconductivity is obtained for $K_xFe_{2-y}Se_2$ peaking at 32 K for $K_{0.8}Fe_{1.6}Se_2$. [66]

The addition of the doping to the $BaFe_2As_2$ system not only creates the onset of superconductivity, but also inhibits the spin-density-wave (SDW) and resulting orthorhombic structural phase transition and AFM ordering at 140 K. [59] The effect of doping on the system can be seen in Figure 1.3 which shows the effect of different amounts of "extra" electrons per iron atom on the superconducting temperature and the suppression of the spin-density-wave, and AFM ordering. [67]

This suppression of the magnetic moment for superconductivity makes the magnetism of these compounds of particular interest. They have been known to exhibit both ferromagnetism and antiferromagnetism, sometimes even in the same compound. $SmMn_2Ge_2$, for example has four different transition temperatures. [68] The moments on the manganese atoms order as an AFM below 385 K, as a FM below 348 K, as an AFM again at 196 K, and then the moments on the manganese and samarium align as a FM below 64 K. It is suggested that the ordering on the manganese atoms depends on the Mn-Mn distances, with FM preferred at longer distances (2.85-2.87 Å), and AFM ordering preferred at shorter distances. [68, 69] Understanding this magnetism is the first step in learning how to suppress it, and hopefully, promote superconductivity.

1.4 Objectives and outline of the dissertation

In this dissertation, several different compounds with the $ThCr_2Si_2$-type structure with mixed metal occupancy will be presented along with their magnetic and electrical properties. It is still difficult to predict the properties of these compounds as the mixed metal occupancy shows no ordering of the site. This dissertation will focus on understanding the different effects that having a mixed metal site for these 122-type compounds can achieve.

In chapter 2, some of the characterization techniques for these compounds are discussed in relation to these particular compounds, as well as the basic principles behind them. Crystallography is heavily emphasized but property determination

such as magnetism, and transport are also covered.

In chapter 3 we study the relationship between antiferromagnetic order and the electronic properties of $KCuMnS_2$ with the $ThCr_2Si_2$-type structure. We propose two magnetic structures for $KCuMnS_2$ with the $ThCr_2Si_2$-type structure. Powder samples of $KCuMnS_2$ and $KLiMnS_2$ were prepared for structural studies and magnetization measurements. In both compounds, the Mn^{2+} site is alloyed by either Cu^+ or Li^+. We also prepared single crystals of $KCuMnS_2$ for x-ray and neutron diffraction studies and resistivity measurements. We relate these properties to the electronic structure calculated with density functional theory. Neutron diffraction studies reveal that $KCuMnS_2$ exhibits long-range magnetic ordering with a Néel temperature near 160 K and a moment of 0.92(2) μ_B/ Mn^{2+} at 6 K. In contrast, $KLiMnS_2$ never exhibits long-range magnetic ordering down to 3.5 K. Both sulfides never display a crystallographic phase transition from our temperature-dependent x-ray and neutron diffraction studies. We discuss the magnetic phases in detail and how they relate to isostructural phases such as iron-based superconductors and related chalcogenides. Electrical resistance measurements indicate that while $KCuMnS_2$ is semiconducting, there is an anomaly around the Néel temperature, which indicates that long range magnetism influences its electronic structure. We also discuss the onset of a competing magnetic moment with an onset temperature around 210 K.

In chapter 4 we discuss the effects of changing the Ch composition to the larger selenium. Powder samples of $KCuMnSe_2$ and $KLiMnSe_2$ were prepared for structural studies and magnetization measurements. We also prepared single crystals of

$KCuMnS_2$ for x-ray diffraction studies. Neutron diffraction studies reveal some long range magnetic ordering for $KCuMnSe_2$, but not for $KLiMnSe_2$, through the appearance of temperature dependent peaks. We discuss the temperature dependence of these peaks, and the possible onset temperatures for them. We discuss the magnetic susceptibility of both compounds and how there divergence between their FC and ZFC curves could be related to a spin-glassiness type behavior. We show with resistance measurements that $KLiMnSe_2$ is an insulator whereas $KCuMnSe_2$ behaves as a degenerate semiconductor between 150 and 290 K, below which it behaves as a classic semiconductor. These properties are related to their DFT calculations and localized density of states to discuss how the copper *d*-orbitals play a large role in the conductance of the sample.

In chapter 5 samples of $KCuFeS_2$ and $KCuFeSe_2$ are prepared to study the effects of changing the magnetic ion in the system from Mn^{2+} to Fe^{2+}. Powder samples were prepared for structural studies, NPD, and magnetic susceptibility measurements were performed on $KCuFeSe_2$. These properties are discussed in relation to their DFT calculations. Neutron diffraction at 6.5 K and 70 K reveals no strong indication of long range magnetic ordering through the onset of additional peaks, however some peaks, particularly the (002) and the (020) do show some increase in intensity at lower temperature. Magnetic susceptibility of $KCuFeSe_2$, shows signs of a spin glass transition through the divergence of its FC and ZFC curves. Another indication of spin-glassiness is that this divergence is also suppressed with increasing field, and the temperature at which the divergence occures is also lowered with increasing field. The DFT calculations for these compounds is presented and how

they relate to the properties displayed. The attempted synthesis of additional compounds with three transition metals sharing the M site is also discussed and what their success, or lack thereof, indicates about the M position for these KM_2Ch_2 compounds.

In chapter 6 we provide a conclusion to this dissertation. Future work that has yet to be done on these compounds is discussed, as well as additional compounds that could be inspired based off of this work.

Chapter 2: Theory and Techniques

2.1 Overview

Here we will provide an overview of the general synthetic techniques and characterization methods used for the materials reported within this thesis.

2.2 Synthesis

2.2.1 Solid State

All of the chalcogenides reported in this thesis are able to be synthesized in their powder forms through a simple solid state procedure. This entails combining the respective metals desired in the final product, before heating the mixture under a flow of the desired chalcogenide. For any of the following $AMM'Ch_2$ desired products, with A being the cation in between layers of substitutionally alloyed M and M' metal Ch_2 layers, various powder forms of A, M, and M' can be used for the synthesis.

A_2CO_3 was universally used as the source of the A cation, which predominantly means K_2CO_3, as the A cation is largely held constant throughout this work. This solid state synthesis has also shown to be accepting of multiple forms of M, and

M'. Li_2CO_3 was utilized as the sole source of Li metal, however for the other metals in this series, both the pure metals, and their oxides can be utilized. This has demonstrated an impressive acceptance of the initial oxidation state of the for the desired +1 and +2 state metals, as long as the metal used is not in a more oxidized state than desired in the final product. These metals were mixed with in stoichiometric amounts of M, and M' with roughly a 10 % excess of the A_2CO_3 (a 5% excess of lithium carbonate to account for some Li evaporation).

In order to achieve the Ch flow under temperature, two different methods were used to incorporate either sulfur or selenium. For Ch = S, the previously prepared powder was heated under Ar flow in a furnace up to 800 °C before charging the Ar flow with carbon disulfide. Due to the possible formation H_2S, the exhaust of the flow was passed through a bleach bubbler as a safety precaution. The setup for this can be seen in Figure 2.1. For Ch = Se, selenium powder is added to the original powder mixture, also in a 10 % excess. To facilitate the formation of H_2Se, the mixture was heated under a 5 % H_2 in nitrogen flow at the elevated temperature when compared to the sulfide synthesis of 900 °C. A bleach bubbler was also used for this synthetic procedure due to the presence of H_2Se.

After cooling, the samples can then be manually retrieved. By mass, even mechanical recovery can routinely produce yields over 100 %. The excesses of the A cation and the chalcogenide results in the presence of A_2Ch_x, in these cases, either potassium polysulfide and potassium polyselenide. This impurity can either be washed away using small amounts of methanol, though this may hurt crystallinity, or left with the powder to facilitate single crystal growth.

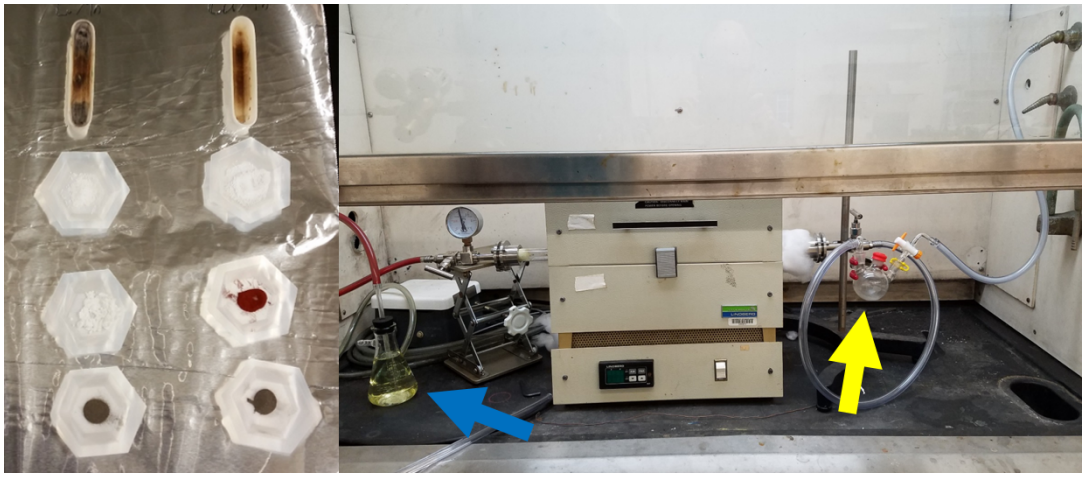

Figure 2.1: General synthetic setup showing the pre-mixed powders (left), and furnace setup used for CS_2 flow (right). The 3-neck flask used to charge the Ar flow with CS_2 is shown with the yellow arrow, and the bleach bubbler is emphasized by the blue arrow.

2.2.2 Single Crystal

The method used to grow all of the single crystals presented in this manuscript is a simple flux growth in a double sealed ampule. Small amounts of powders that contained the potassium polychalcogenide impurity were placed in a quartz ampule and sealed under vacuum. This ampule was then placed in a second quartz ampule, and sealed under vacuum. These ampules were then placed in a furnace and heated at 1000 °C for 10 h, before being slowly cooled at a rate of 6 °C per hour to 500 °C to facilitate the formation of a single crystal from the melt. The ampules could then be broken open, and the single crystals could be recovered manually removing any impurities. Images from this process can be seen in Figure 2.2

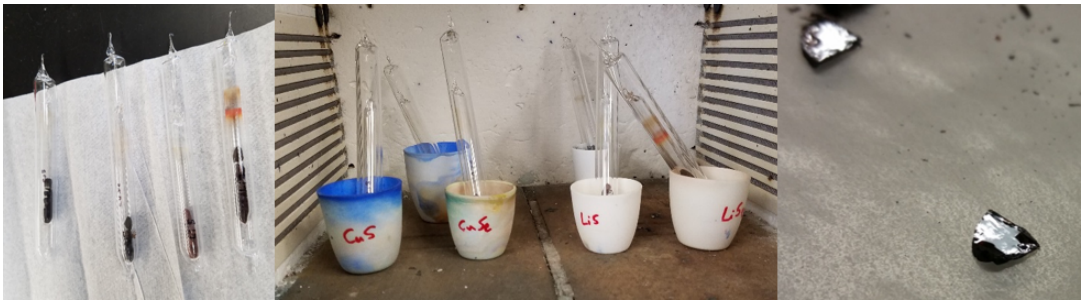

Figure 2.2: Single crystal growth, from powders being sealed in double quartz ampules (left), to being placed in a furnace (center), to being recovered as single crystals (right).

2.3 Crystallography and Diffraction

All of the materials presented in this work crystallize in the $ThCr_2Si_2$-type structure. By definition, this means that they have a basic unit cell that is the smallest repeating unit that retains the full symmetry of the overall crystal structure, which is repeated, indefinitely, in three dimensions. Of the seven possible crystal systems, the $ThCr_2Si_2$-type structure has the tetragonal crystal system, possessing a unique fourfold axis, either through rotation, or inversion. The cell for this system is a rectangular cube, with edges (or cell axis) a, b, and c, where $a = b \neq c$, with angles α, β, and γ, where all angles are 90 degrees. Getting a bit more specific, it is a body-centered tetragonal system with lattice points on each corner of the unit cell, as well as an addition lattice point in the center of the cell. The addition of mirror planes halfway through each of the three axis, gives the space group $I4/mmm$ (No. 139).

With this unit cell in mind, we can then go on to indicate, points, directions

with respect to the unit cell, and planes that extend in two dimensions through the unit cell and others that form the parent crystal. Points are characterized using u, v, and w to represent fractional positions along one unit cell of a, b, and c. Directions are indicated in the format of $[abc]$, where [100] indicates the direction one unit cell away from the origin along the a axis and [111] indicates the direction diagonal across the cell. Planes that bisect the unit cell are depicted by Miller indices, (hkl). The depiction is with respect to where the plane intercepts the individual axis, specifically its' inverse. If a lattice plane intersects the c axis at position of $w = 0.5$, or halfway through the unit cell along the c axis, then the Miller indices for w would be (1/0.5) 2 giving $(hl2)$. If there is no intercept, then the Miller indices would be 0. This plane can be seen in Figure 2.3 along with other important planes for the $ThCr_2Si_2$-type structure. In the case of the (200) plane, it is comprised of only thorium atoms in the $ThCr_2Si_2$, though this is replaced by potassium for the work herein. It is important to note, that the planes continue throughout the crystal, meaning that there can be more than one plane of any given indices transecting a unit cell with a very specific distance between these planes. In the example of the (0 1 3) plane, the plane shown intersects the b axis in the following unit cell. [70]

2.3.1 Diffraction Theory

Once these compounds have been (hopefully) made, we need some way to confirm that they are, in fact, what we were trying to make. As the compounds we are trying to make should be crystalline in nature, we utilize the workhorse of

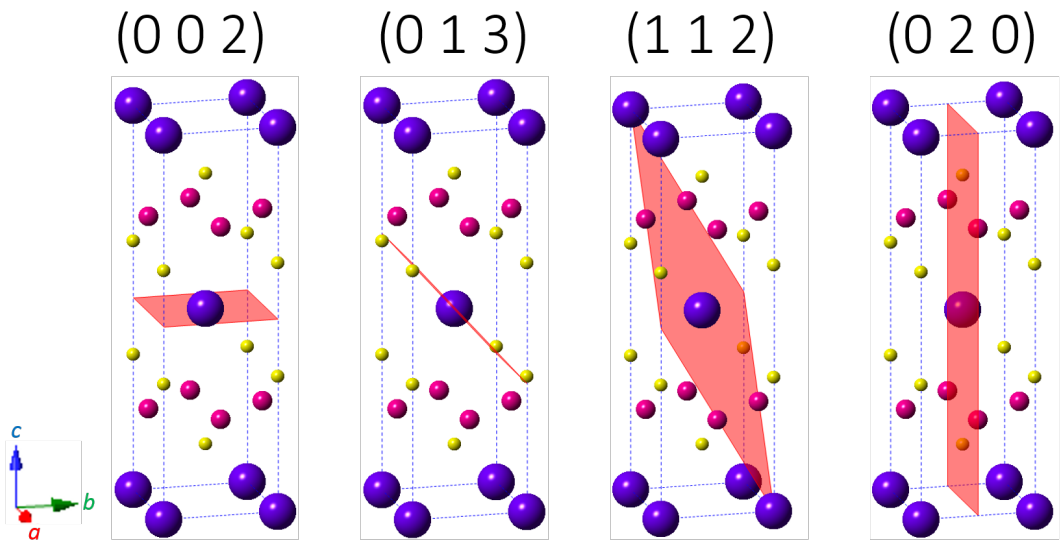

Figure 2.3: Examples of important Miller indices in the $ThCr_2Si_2$. Thorium is in purple, chromium is in magenta, and silicon is in yellow. Though these are replaced with potassium, various metals, and a chalcogenide, respectively in this work.

the materials characterization techniques. Just as the organic chemist has Nuclear Magnetic Resonance (NMR), the materials chemist has powder X-ray diffraction (PXRD). While a single crystal is usually the ultimate goal for characterization, the fact that powders are much easier to produce, PXRD is generally easier and faster to take than a single crystal X-ray pattern, and the fact that single crystals can be ground down into powders to obtain a PXRD if necessary, makes PXRD the go-to characterization method for crystalline materials.

It is necessary for the materials characterized to be crystalline for X-ray diffraction, as it is the very nature of crystallinity or more specifically, the Miller indices, which tell us about our compound through PXRD. The interaction of these planes with incoming monochromatic radiation with waves that are all in phase is repre-

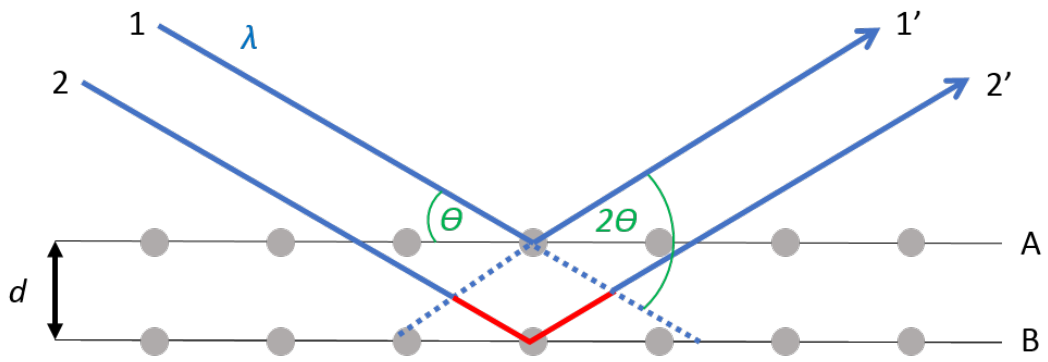

Figure 2.4: Depiction of the conditions required for Bragg's law. Indecent beams of radiation (1 and 2) with wavelength λ diffracting off of planes of atoms (A and B) separated by distance d at angle θ. Diffracted beams 1' and 2' scattered from their original beams by an angle of 2θ, with beam 2' ultimately traveling an additional distance in red.

sented in Figure 2.4. Two waves of radiation with wavelength λ (1 and 2), scatter off of two atoms in planes A and B separated by distance d. As plane B is farther away from the source of the radiation, wave 2 travels farther than wave 1. Likewise, the resultant scattered wave 2' travels farther than wave 1'. This additional distance is represented in red in Figure 2.4. When the angle of attack of the incoming radiation is θ, the additional distance traveled by wave 2 is $d\sin(\theta)$ with the overall additional distance traveled by waves 2 and 2' is $2d\sin(\theta)$ represented in red in Figure 2.4. When this additional distance is equal to an integer of the wavelength λ, the resulting waves remain in phase. When this Bragg condition is met, it is this constructive interference when the waves remain in phase that give the response on a given instruments detector. This provides Bragg's law for this constructive

interference.

$$n\lambda = 2d\ \sin\theta \tag{2.1}$$

However, when the additional distance by a wave is half of the wavelength, or some integer thereof, this will lead to destructive interference, and no signal will be seen. Given a known crystal structure, and the relationships between the Miller indices inherent for that crystal system, we can predict which indices will produce constructive interference, and which will produce destructive interference. For the case of the $I4/mmm$ crystal system, the general reflection conditions are

$$hkl : h + k + l = 2n \tag{2.2}$$

where n is an integer. [71] That is to say, we will not see a Bragg condition for (0 0 1), but we will for (0 0 2) *etc.*

This general principle of Bragg's law can apply to any form of radiation with some wavelength λ. Specifically for this work, that means X-ray radiation and neutron radiation. While the interaction with the Miller indices is consistent with regards to Bragg's law for different types of radiation, the ability for any given atom to scatter that radiation is not. X-ray radiation reacts with the electron cloud of

individual atoms, and thus is generally proportional to the atomic number Z of the atoms involved. As a result, not only is it difficult for X-rays to perceive small atoms which is problematic for the Li containing compounds, but it becomes difficult to discern atoms with close atomic numbers. The scattering ability for X-rays also decreases with increasing angle, reducing the intensity at higher values of 2θ.

Neutrons have neither of these problems. Their coherent scattering (b_i) by the nuclei of the atoms occurs independently of Bragg angle, and follows no particular trend, even among varying isotopes of individual elements. The values of neutron scattering for some relevant atoms are included in Table 2.1. The first thing to note with this Table is that elemental lithium has a large absorption cross section of 70.5 barns. This is due to the very large absorption cross section of 940(4) barns for ^{6}Li. In order to avoid this, lithium containing samples prepared for neutron diffraction were prepared with isotopically pure ^{7}Li. There is also a significant difference between the scattering cross sections for the various elements sharing a site in the created compounds of copper, manganese, and iron of 8.03, 2.15, and 11.26 barns respectively. As neutrons themselves have a magnetic moment being spin-$\frac{1}{2}$ particles, they can also interact with the magnetic moments of compounds through dipole-dipole interactions of unpaired electrons, though the scattering, like X-rays, declines with θ. When these electrons align to create a magnetic moment, they can create their own magnetic unit cell with Miller indices, often separate and larger than the crystal unit cell.

Table 2.1: Neutron scattering lengths and cross sections for elements used for neutron diffraction, or for select isotopes when specified. With coherent (Coh) and incoherent (Inc) bound scattering lengths in fm (b) and scattering cross sections in barns (xs), with the total scattering cross section (Scatt xs), and absorption cross section (Abs xs) for neutrons with a wavelength λ = 1.798 Å, E = 25.30 meV, or a velocity of v = 2200 m/s. 1 fm = 1×10^{-15} m, 1 barn = 1×10^{-24} cm^2 or 100 fm^2. [72]

Isotope	Coh b	Inc b	Coh xs	Inc xs	Scatt xs	Abs xs
Li	-1.90	—	0.454	0.92	1.37	70.5
^{6}Li	2.00-0.261i	-1.89+0.26i	0.51	0.46	0.97	940(4)
^{7}Li	-2.22	-2.49	0.619	0.78	1.4	1.4
K	3.67	—	1.69	0.27	1.96	2.1
Cu	7.718	—	7.485	0.55	8.03	3.78
Mn	-3.73	1.79	1.75	0.4	2.15	13.3
Fe	9.45	—	11.22	0.4	11.62	2.56
S	2.847	—	1.0186	0.007	1.026	0.53
Se	7.97	—	7.98	0.32	8.3	11.7

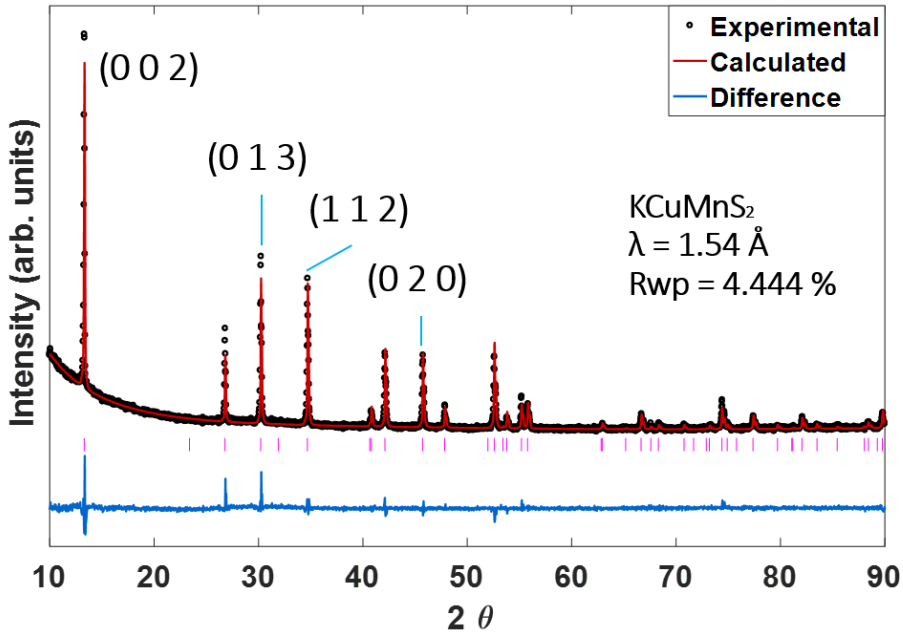

Figure 2.5: An example of a PXRD pattern for KCuMnS2. Reflections from the (002), (013), (112), and (020) indices are shown. Cu Kα radiation, $\lambda = 1.5418$ Åwas used, and an R_{wp} of 4.444 from Rietveld Refinement.

2.4 Diffraction techniques

2.4.1 X-ray (Powder)

For PXRD, the powder samples need to be ground thoroughly so that there are crystalline domains distributed over all possible orientations. While every reflection will be at their own value of 2θ, in three dimensions, there is an additional angle ϕ which is the orientation of that plane around the 360° possible while still maintaining 2θ. All of these orientations creates a cone of diffraction for every reflection. With powder samples, there are crystalline domains over all values of ϕ, thus detecting

over a single line along the radius of the cone of diffraction will provide all available reflections for 2θ. The difficulty here is that multiple reflections throughout the crystal can have different ϕ values, but still have similar or identical 2θ angles whose cones of diffraction will overlap.

These cones of diffraction allow a flat sample to be held in place while the beam source and detector scan over a linear 2θ. The sample needs to be flattened as any changes in placement will affect the actual 2θ value. An example of a typical powder pattern obtained from PXRD is in Figure 2.5. Over a scan of 2θ, where the $I4/mmm$ system satisfies Bragg's law, there is an increased intensity of the scattered beam. For the PXRD patterns in this work, the y-axis is in arbitrary units. It is the relative intensity between peaks in a powder pattern that are indicative of the crystal structure, while overall intensity varies largely on the bulk sample properties, and length of the scan. For this work, room temperature powder X-ray diffraction (PXRD) data were collected on a Bruker D8 X-ray dffractometer (Cu Kα radiation, $\lambda = 1.5418$ Å) at the University of Maryland X-ray Crystallographic Center (XCC). For a routine measurement, data were collected with a step size of 0.02° between 7° and 90°C 2 θ.

2.4.2 Neutron (Powder) NCNR

Neutron powder diffraction (NPD) utilizes the same principles of PXRD, with the differences in radiation mentioned prior. One technical difference is that while laboratory X-rays are conventionally Cu Kα radiation with a $\lambda = 1.5418$ Å(Though

other commercial options like molybdenum with Mo Kα radiation with a $\lambda = 0.71073$ Åare not unheard of) neutrons come in a variety of different wavelengths depending on the source and monochometer. Thus, instead of reporting Bragg reflections with respect to 2θ, which is λ dependent, it can be represented by the scattering vector q or Q.

$$Q = \frac{4\pi sin(\theta)}{\lambda} \tag{2.3}$$

This removes the wavelength dependence of the scattering condition, and reports Q in either $Å^{-1}$ or nm^{-1}. Plugging in Bragg's law for λ, and rearrainging the equation, gives a real space value of $d = \frac{2\pi}{q}$.

Neutron powder measurements performed at the NIST (National Institute of Standards and Technology) Center for Neutron Research (NCNR) on the BT-1 diffractometer with wavelength $\lambda = 2.079$ Å (Ge 311 monochromator) at a base temperature of 6 K. The samples were loaded into He-filled vanadium cans and subsequently into a closed cycle refrigerator for low temperature measurements (6-300 K).

2.4.3 Neutron (Powder) HFIR

Neutron powder measurements performed at Oak Ridge National Laboratory (ORNL), High Flux Isotope Reactor (HFIR) on the HB-2A diffractometer with

wavelength $\lambda = 2.4103$ Å (Ge 113 monochromator). The samples were loaded into He-filled vanadium cans and subsequently into a closed cycle refrigerator for low temperature measurements (3.5-200 K).

2.4.4 X-ray (Single Crystal Diffraction)

For single crystals, the random orientation of powder samples no longer exists. Here, ϕ becomes an important value, as the cone of diffraction is now no longer a cone, but single spots from the incident beam scattering off of different Bragg reflections. By taking into account the intensities of these reflections, we are able to determine not only the planes that create each reflection, but also the orientation of those planes with respect to one another, and the occupancies of those planes. With enough reflections, single crystal XRD becomes significantly more accurate at determining the site occupancy of a given crystal.

X-ray data was collected on a $KCuMnS_2$ single crystal of approximate dimensions 0.29 mm $\times$ 0.13 mm $\times$ 0.04 mm in size with Mo Kα radiation of λ=0.71073 Å. The crystal was measured every 20 degrees from 110 K to 250 K using the Bruker Smart Apex-II CCD system to uncover any possible crystallographic phase transitions coinciding with the onset of long-range magnetic order. The structure was solved and refined with the SHELX Software Package. [73]

2.4.5 Neutron (Single Crystal Diffraction)

Temperature dependence of the magnetic peak centered at approximately 1.24 $Å^{-1}$ was carried out on a single crystal with the position sensitive detector on the BT-7 triple-axis spectrometer (NCNR) [74] with a wavelength $\lambda = 2.359$ Å from 10 to 220 K.

2.5 Powder Diffraction Data Analysis

While not as straight forward as single crystal analysis, there are still many ways to perform an analysis on PXRD. Due to the overlap of Bragg reflections with the same 2θ regardless of ϕ makes direct interpretation of the intensities incredibly difficult. What can interpreted is peak position, these can be indexed to determine likely unit cell or lattice parameters, followed by possible space groups. Either the Le Bail or Pawley methods can be used to extract peak intensities from overlapping peaks and refine unit cells. This is very useful when attempting to determine the identity of unknown impurity phases in a product. For true identification however, a predicted model is needed to compare to the raw data.

2.5.1 Rietveld Refinement

The Rietveld method of refinement, like the Le Bail and Pawley methods refines the unit cell of a powder pattern. Where it differs in the fact that it is refining these parameters based on a comparison of a calculated spectra against the raw data. This means that in order to perform a Rietveld refinement, a prediction of

the compound must be made. In the case of a successful synthesis, this isn't an issue as the product will be the known, desired one. By using a predicted crystal structure, with all site occupancies and lattice parameters, a Rietveld refinement creates a predicted powder pattern for that crystal. It then compares this predicted powder pattern to the actual powder pattern and determines goodness of fit factors R_{wp} (weighted profile), R_p (profile R-factor), and R_{exp} (expected goodness of fit). The model is then "corrected" by systematically refining the different crystallographic and structural parameters using a least squares method to obtain a model with the calculated powder pattern with the best fit to the experimental data.

Rietveld refinements of the PXRD and NPD data was carried out using the TOPAS 5.0 software. [75]

2.6 Additional Neutron Techniques

2.6.1 MACS and SPINS

MACS data was collected on the Multi Axis Crystal Spectrometer (MACS) at the NCNR, using 5 meV elastic scan at 1.5 K. [76] Elastic neutron scattering experiments were conducted on $KCuMnS_2$ single crystals aligned in the (HK0) plane. All elastic measurements were done at 1.5 K and 180 K above the ordering transition observed in BT-7 elastic data. All scans were done with a fixed Ef = 5 meV using a Be filter with flat horizontal focusing of the monochromotor. Additional elastic scattering data was collected on the Spin Polarized Inelastic Neutron Spectrometer (SPINS) on the same $KCuMnS_2$ single crystal aligned to observe the temperature

evolution of the (0.5, 0.5, 0) reflection observed in MACS data. Longitudinal and transverse scans were done about the (0.5, 0.5, 0) reflection at temperatures from 100 - 220 K using the point detector system at SPINS with Ef = 5 meV fixed analyzer.

2.7 Magnetism

2.7.1 Squid

As we will have some compounds containing atoms with unpaired electrons, they will inherently have some form of magnetism. In order to help determine if this magnetism comes in the form of paramagnetism, ferromagnetism, antiferromagnetism, or ferrimagnetism, we can determine how these unpaired electrons react to an external field. This magnetic susceptibility should give an indication if, in the absence of thermal energy upon cooling, if the disordered moments of paramagnetism align uniformly for ferromagnetism, uniformly anti to cancel each other out in antiferromagnetism, or nonuniform anti to each other for ferrimagnetism. Under the influence of a magnetic field upon cooling, a paramagnet will steadily align itself to the field, a ferromagnet will strongly align itself to the field once its' individual moments start aligning with each other at its Curie temperature T_C, and an antiferromagnet will lose its' alignment to the field once its' magnetic moments orient themselves against one another at the Néel temperature T_N.

Typical temperature dependent DC (direct current) magnetic susceptibility measurements were carried out using a Quantum Design Magnetic Property Mea-

surement System (MPMS) on powder. Field-cooled (FC) and zero field-cooled (ZFC) measurements were taken from 1.8 K to 300 K with an applied magnetic field of 500 Oe. Magnetization versus field loops were carried out using the MPMS from -7 T to 7 T on the powder samples at 2 K and 50 K.

2.7.2 Neutron

When a crystal structure has magnetism, this magnetism can possess some ordering, such as for ferromagnetism, antiferromagnetism, or ferrimagnetism. This magnetic ordering will form its own unit cell, its magnetic cell, with is possibly different than that of the structural unit cell. As previously stated, neutrons have the ability to scatter off of magnetic moments, and thus when scattering off of a magnetic ordering, can produce their own magnetic Bragg reflections.

Symmetry analysis was performed using ISODISTORT from the ISOTROPY web-based software suite. [77] ISODISTORT is web-based program that is used to explore the physical distortions (atomic displacements, atomic orderings, strains, rotational moments, and magnetic moments) based off of crystallographic information provided by the user. ISODISTORT was used in this work to determine possible magnetic structures that could then be used as a model for Rietveld refinement. Rietveld refinements of the neutron diffraction data was carried out using the TOPAS 5.0 software. [75]

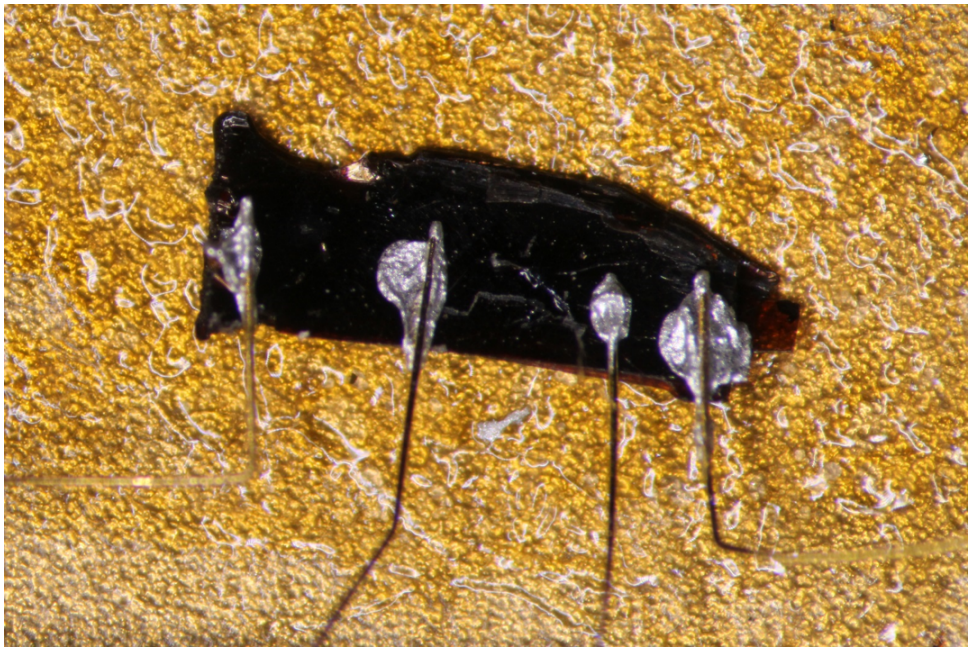

Figure 2.6: $KCuMnS_2$ single crystal wired for electrical transport measurements.

2.8 Transport

2.8.1 PPMS 4-point probe

Electrical transport measurements were preformed using a 9 T Quantum Design Physical Property Measurement System (PPMS-9) with polycrystalline or single crystal samples. Polycrystalline samples were ground into a powder and pressed into pellets utilizing < 2 ton uniaxial load without sintering. Electrical resistivity was measured using the four-probe method with gold wire and contacts made with silver paste. The temperature and field dependence of longitudinal electrical resistivity was measured in a range from 300 K to 1.8 K with applied current of 0.1 mA and frequencies near 17 Hz.

2.9 Band Structure and Density of States

All density functional theory (DFT) [78, 79] calculations were performed by using the Vienna Abinitio Simulation Package (VASP) [80–83] software package with potentials using the projector augmented wave (PAW) [84] method. The exchange and correlation functional were treated by the generalized gradient approximation (PBE-GGA). [85] The cutoff energy, 450 eV, was applied to the valence electronic wave functions expanded in a plane-wave basis set for all chalcogenides. A Monkhorst-Pack [86] generated $21 \times 21 \times 7$ k-point grid was used for the Brillouin-zone integration to obtain accurate electronic structures.

To start, structural optimization calculations were performed for each K$M'M''Ch_2$ (M', M'' = Li, Mn, Cu, Fe; Ch = S, Se) composition whereby previously reported lattice constants were used as the starting point for the calculations. Due to the mixed occupancy of the metal site in these compounds, a 2x2 superstructure of the body-centered tetragonal cell was required in order to represent this occupancy. However, it should be noted that this does impose artificial ordering of the metal site which may not occur in the synthesized compounds. Through the structural optimization calculations, all ions were allowed to relax to their lowest energy positions.

From the optimized structure, a self-consistent calculation was done in order to accurately calculate the electronic charge density corresponding to the optimized structure. This self-consistent charge density was then used for subsequent non-self-consistent density of state and band structure calculations. Density of state

calculations were performed using the tetrahedron method with Blöchl corrections for partial occupancy of each electronic orbital with a smearing width fixed at 0.02 eV with an orbital angular momentum decomposition so each sub-orbital can be evaluated in the system. For band structure calculations, partial occupancy was changed to Gaussian smearing with a smearing width of 0.1 eV as required for band structure calculations as only high-symmetry points in the Brillouin zone are calculated. Band structure calculations were also performed with an orbital angular momentum decomposition.

All the above calculations were performed allowing spin polarized degrees of freedom. Various starting magnetic structure were chosen based on the composition of the metals in the metal sub-lattice. Optimized magnetic states were calculated along with the structural optimization and then fixed for the self-consistent calculation as well as density of state and band structure calculations. A summary of optimized lattice parameters, starting magnetic structure, optimized magnetic structure and corresponding moment, and ground state energies of each calculated phase are displayed in Table A.1.

Chapter 3: The Magnetic Structure of $KCuMnS_2$ and its Comparison to $KLiMnS_2$

This chapter contains work that was published in *PhysicalReviewMaterials* **2019**, 3, pg. 044411. Xiuquan Zhou, Brandon Wilfong, Jeffrey W. Lynn, Keith Taddei, Peter Zavalij, Limin Wang, and Efrain E. Rodriguez were contributing authors on the manuscript.

Dr. Peter Zavalij performed the single crystal analysis for this work, Brandon Wilfong performed properties measurements and accompanying Curie-Weiss fits, density functional theory and band structure calculations, and Dr. Limin Wang performed additional density functional theory and band structure calculations. Austin Virtue carried out sample preparation and powder diffraction measurements.

3.1 Introduction

The $ThCr_2Si_2$-structure type (Figure 3.1), also known as the 122-type in the condensed matter physics literature, represents a large collection of layered compounds that can incorporate much of the periodic table and therefore exhibit a variety of physical phenomena. [34, 87] For example, the 122-type pnictides (Pn) and chalcogenides (Ch) with iron have attracted significant amount of attention

because of their superconducting properties. The $BaFe_2As_2$ parent compound can be either aliovalently or isovalently doped to a superconductor from an antiferromagnetic semimetal. [60,88–90] The structurally related $K_xFe_{2-y}Se_2$ can also express superconductivity, although it is always mixed with an antiferromagnetic, insulating phase due to the distribution of iron vacancies. [91–93]. The origin of superconductivity in both pnictides and chalcogenides is still on-going research, and several implied mechanisms including spin fluctuations and nematic electronic states have been proposed. [94–98]

Due to the proximity to Fe, we first explore Mn chalcogenides in the 122-type structure to find similar ground states. The ACo_2X_2 series (where $X = Pn$ or Ch and A is an alkali or alkaline earth metal) tend to express long-range ferromagnetic order. [49, 99, 100, 100, 101] For Mn, the magnetism of its 122-type pnictides, such as $BaMn_2As_2$, has been well studied, included by neutron diffraction. [102–104] However, the ternary 122-type Mn chalcogenides are unknown. Likely, this arises from charge balance arguments. By replacing As^{3-} with Se^{2-}, one must reduce Mn below the +2 oxidation state, which is difficult to do for the stable d^5 transition metal. However, Mn^{2+} can be incorporated into quaternary 122-type chalcogenides by alloying it with a monovalent cation such as Cu^+ or Li^+. [105] Indeed, ACuMnCh_2 and ALiMnCh_2 have been reported in the pioneering work of Greenblatt [47, 48, 50, 51, 106] and Bronger, [107, 108] respectively. Unlike the ternary 122-type pnictides, no long-range magnetic ordering was found for ACuMnCh_2 compounds in earlier studies, [47, 48] and no physical property measurements carried out for ALiMnCh_2. [107]

Due to the lack of neutron diffraction data for these quaternary Mn chalcogenides in previous studies, their underlying magnetic order remains unknown. Hence, more comprehensive studies are needed to elucidate their relationship to structurally related Fe-based superconductors. This is crucial for any attempt to find a new non-Fe based system that can exhibit superconductivity. We focus here on the sulfides of Mn with the A cation being K^+. Any future studies on tuning the properties of quaternary Mn sulfides through doping would require an understanding of 1) the underlying magnetic order, 2) the ideal synthetic and crystal growth conditions, and 3) the electronic and transport properties. We therefore reinvestigate and present the preparation, single crystal growth, chemical and magnetic structures, and ground state properties of these 122-type quaternary phases.

3.2 Synthesis and experimental details

3.2.1 Sample preparation

The quaternary sulfides were prepared by heating a mixture of pure metals with alkali metal carbonates under a flow of argon charged with carbon disulfide (99.9% ACS reagent grade, Aldrich). Depending on the desired product, stoichiometric amounts of Mn metal (99.95% -325 mesh, Alfa Aesar) were mixed with either Cu metal (99.5% -200 +325 mesh, CERAC inc.) or a 5% excess of lithium carbonate (98%, Honeywell) to account for some Li evaporation, along with a 10% excess of potassium carbonate (99% anhydrous, Alfa Aesar). Powders were ground together in an agate mortar and pestle as an acetone slurry to a homogeneous mixture and

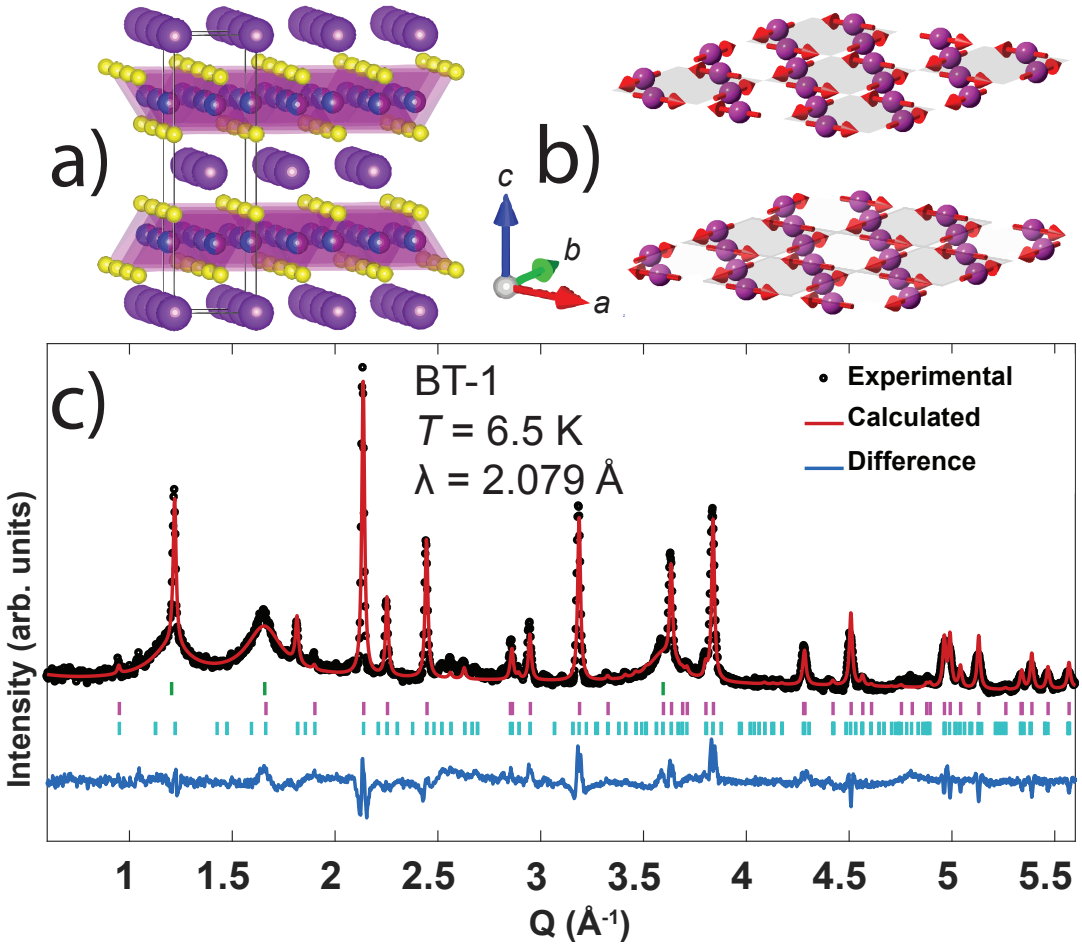

Figure 3.1: Chemical and plausible magnetic structure of $KCuMnS_2$ from neutron powder diffraction. (a) Atomic structure with equal occupancy of Cu/Mn sites (blue and magenta) forming two-dimensional sulfide (yellow) tetrahedral layers separated by potassium (purple) cations. b) Canted from (a), a proposed antiferromagnetic pinwheel structure of $KCuMnS_2$ with the moment in the ab-plane. (c) Rietveld refinement fit to neutron powder diffraction data (R_{wp} = 7.211 %) with magnetic phase (bottom ticks), structural phase (middle ticks), and impurity peaks (top ticks) indicated.

allowed to dry. A typical synthesis of 12.5 mmol would consist of 0.9502 g K_2CO_3, 0.4849 g Li_2CO_3, 0.7943 g Cu, 0.6867 g Mn, and approximately 15 mL of CS_2.

The mixture was loaded as a powder into an alumina crucible which was then placed into a tube furnace under a flow of argon. The mixed gas flow pathway was set up to flow into and out of a three neck flask before entering the furnace, exiting the tube furnace through a bleach solution. The furnace was then heated at a rate of 180 °C per hour up to 800 °C. Once the temperature was reached, a fifteen fold excess of carbon disulfide was added via syringe to the three neck flask as a liquid and allowed to evaporate into the argon flow. Following complete evaporation of the carbon disulfide, the sample was cooled to room temperature at 180 °C per hour.

Single crystal growth was achieved by placing roughly 0.25 g of the unwashed powder into an evacuated quartz ampule, which was then placed in a second evacuated quartz ampule, heated at a rate of 50 °C per hour to 1000 °C. This temperature was held for 10 hours before cooling at a rate of 6 °C per hour to 500 °C. The ampule was then cooled at a rate of 30 °C per hour to room temperature. Single crystals were then recovered manually.

3.2.2 Diffraction, Magnetization, Resistivity, and DFT

Neutron powder measurements for $KCuMnS_2$ were performed on the BT-1 diffractometer at the NIST Center for Neutron Research (NCNR) with wavelength $\lambda = 2.079$ Å (Ge 311 monochromator) at a base temperature of 6 K. Temperature dependence of the magnetic peak centered at approximately 1.24 $Å^{-1}$ was carried

out on a single crystal with the position sensitive detector on the BT-7 triple-axis spectrometer (NCNR) [74] with a wavelength $\lambda = 2.359$ Å from 10 to 220 K. Neutron powder measurements for $KLiMnS_2$ were performed on the HB-2A diffractometer at the Oak Ridge National Laboratory, High Flux Isotope Reactor (HFIR), with wavelength $\lambda = 2.4103$ Å (Ge 113 monochromator). Temperature dependent powder diffraction patterns were take starting from a base temperature of 3.5 K. Symmetry analysis was perfomred using ISODISTORT from the ISOTROPY web-based software suite. [77] Rietveld refinements of the neutron diffraction data was carried out using the TOPAS 5.0 software. [75]

X-ray data was collected on a $KCuMnS_2$ single crystal of approximate dimensions 0.29 mm × 0.13 mm × 0.04 mm in size with Mo Kα radiation of $\lambda = 0.71073$ Å. The crystal was measured every 20 degrees from 110 K to 250 K using the Bruker Smart Apex-II CCD system to uncover any possible crystallographic phase transitions coinciding with the onset of long-range magnetic order. The structure was solved and refined with the SHELX Software Package. [73]

Electrical transport measurements were preformed using a 9 T Quantum Design Physical Property Measurement System (PPMS-9) with polycrystalline and single crystal samples of $KCuMnS_2$. Polycrystalline samples were ground into a powder and pressed into pellets utilizing < 2 ton uniaxial load without sintering. Electrical resistivity was measured using the four-probe method with gold wire and contacts made with silver paste. The temperature and field dependence of longitudinal electrical resistivity was measured in a range from 300 K to 1.8 K with applied current of 0.1 mA and frequencies near 17 Hz.

Temperature dependent DC (direct current) magnetic susceptibility measurements were carried out using a Quantum Design Magnetic Property Measurement System (MPMS) on powder samples of $KCuMnS_2$ and $KLiMnS_2$. Field-cooled (FC) and zero field-cooled (ZFC) measurements were taken from 1.8 K to 300 K with an applied magnetic field of 500 Oe. Magnetization versus field loops were carried out using the MPMS from -7 T to 7 T on the powder samples at 2 K and 50 K.

Initial density functional theory (DFT) [78,79] calculations for a simple layered Néel type magnetic structure were performed by using the Vienna Abinitio Simulation Package (VASP) [80–83] software package with potentials using the projector augmented wave (PAW) [84] method. The exchange and correlation functional were treated by the generalized gradient approximation (PBE-GGA). [85] The cutoff energy, 450 eV, was applied to the valence electronic wave functions expanded in a plane-wave basis set for all chalcogenides. A Monkhorst-Pack [86] generated 21 $\times$ 21 $\times$ 7 k-point grid was used for the Brillouin-zone integration to obtain accurate electronic structures.

In order to demonstrate the effects of the AFM order on the electronic structure for $KCuMnS_2$, the nonmagnetic and magnetic DFT calculations are conducted using VASP with the projector-augmented wave basis in the generalized gradient approximation. The enlarged 2 $\times$ 2 magnetic unit cells are shown in Figure 3.13, which correspond to the stripe-like and non-collinear AFM order suggested by our neutron experiment. The cut-off energy, 450eV, was applied and the gamma-centered k mesh was taken to be 9 $\times$ 9 $\times$ 7 and 21 $\times$ 21 $\times$ 7 for the magnetic and nonmagnetic cases, respectively.

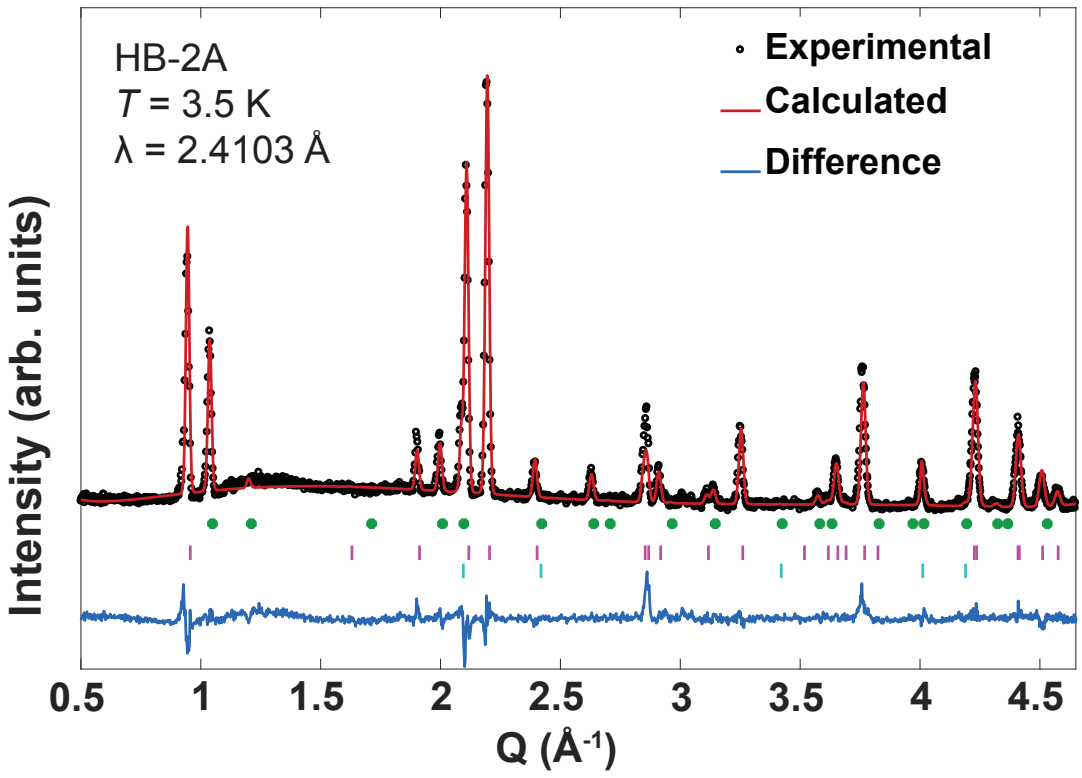

Figure 3.2: Rietveld refinement of the structure of $KLiMnS_2$ with neutron diffraction powder diffraction data at 3.5 K, R_{wp} = 7.019 %. Top tick marks are for $KLiMnS_2$ and bottom tick marks for the MnS alabandite impurity with its magnetic peaks indicated by asterisks.

3.3 Results and discussion

Details of the X-ray measurement results on the $KCuMnS_2$ single crystal are gathered in Table 3.1, which shows that the sample crystallizes in a body-centered tetragonal crystal system. The lattice constants are a = 3.9442(8) Å and c = 13.239(3) Å at 110 K in space group $I4/mmm$ (No. 139). Structural parameters are presented in Table 3.2. All occupancies refined to unity. The Cu and Mn atoms share half of the $4d$ Wyckoff position, which has a site symmetry of $-4m2$. No

superlattice reflections that would imply any ordering of the Mn and Cu atoms on the $4d$ site were observed. The crystal was found to retain tetragonal symmetry at all temperatures measured. Temperature dependence of the lattice parameters from single crystal data did not reveal any structural anomaly from 110 K to 250 K shown in Figure 3.3.

The structure obtained from the single crystal X-ray results (Tables 3.1 and 3.2) was used to model and fit the neutron powder diffraction (NPD) data. The NPD pattern revealed extra reflections at base temperature, which we attribute to antiferromagnetic ordering. These satellite reflections were indexed with a propagation vector of $\mathbf{k} = (\frac{1}{2}, \frac{1}{2}, 1)$, and are discussed in the next section.

The $KCuMnS_2$ neutron powder sample contained an unknown impurity causing three broad background peaks in the BT-1 data. Likely, the impurity in the powder sample is a either a poorly crystalline sulfide or elemental sulfur that could not be washed away. These broad, and likely amorphous, peaks were fit with three Gaussian peak profiles that may be attributed to the same impurity as they all possessed the same peak profile parameters. Refinement of the structural model shown in Figure 3.1c with an $R_{wp} = 7.211$ % indicates full occupancy of all sites in the structure. From NPD, the lattice constants were refined to $a = 3.9405(2)$ Å, $c = 13.215(1)$ Å at 6 K. From temperature dependent NPD measurements, we did not detect any break of the tetragonal symmetry.

Changing the monovalent cation from Cu to Li subtly effects the crystal structure as obtained from Rietveld refinement with the NPD data at 3.5 K (Figure 3.2) . The compound retains the tetragonal structure but the a parameter lengthens to

4.0312(2) Å (from 3.9405(2) Å in Cu) while the c parameter contracts to 13.1453(8) Å. Using isotopically pure ^{7}Li the NPD is fit nicely with the 122-structure along with a less than 5 wt. % MnS alabandite impurity. At 200 K, without the additional magnetic peaks to index, the occupancy of the 4d site refines to 0.489(6) with Mn and 0.48(1) with Li, leading to a site roughly 97 % occupied. Likely, the loss of Li from evaporation leads to the alabandite impurity. Nevertheless, increasing the initial amounts of Li carbonate did not diminish the amount of alabandite impurity.

3.3.1 Crystal Structure

3.3.2 Magnetism and Magnetic Structure

First, we report the results from the magnetization measurements. For both powder and single crystal samples of $KCuMnS_2$, the magnetic susceptibilities display similar features. The susceptibility in Figure 3.6a decreases as the temperature is lowered and no clear cusp in the curve is observed down to 2 K. At 40 K, a Curie tail appears. However, the derivative of the fits to both the zero-field cooled (ZFC) and field cooled (FC) curves, reveals a subtle feature near 160 K. When fit to a polynomial between 100 and 250 K, the first-derivative (Figure 3.6a inset) of temperature-dependent magnetic susceptibility remained fairly constant (above 40 K). Therefore, it is likely that the system displays some low dimensional magnetic coupling or competition between multiple magnetic structures that almost completely flatten the cusp-type feature typical of 3D antiferromagnets. [109–112]

In order to elucidate any possible magnetic ordering in $KCuMnS_2$, we per-

formed temperature dependent NPD and single crystal neutron diffraction (BT-7). As shown in Figure 3.8, the onset of long-range order occurs around 160 K from the magnetic peak centered around 1.24 Å^{-1}. The peak was fit to a Gaussian, and the parameters of the profile shape were analyzed as a function of temperature. The integrated intensity (II) *vs.* T is shown in the inset of Figure 3.8. Fitting the order parameter of magnetization M, which scales with $\sqrt{II}$, yielded a Néel temperature

Table 3.1: Single-crystal X-ray diffraction data for $KCuMnS_2$.

Space Group	$I4/mmm$ (no.139)
a (Å)	3.9442(8)
c (Å)	13.239(3)
Crystal system	Tetragonal
Volume (Å^3)	205.96(9)
Z	2
Calculated density (g cm^{-3})	3.575
λ, Mo Kα Å	0.71073
No. of reflections collected	1080
No. of independent reflections	133
$F(000)$	210.0
R_1, wR_2 (%)	2.01, 4.31
Temperature	110 K

Table 3.2: Structural, lattice, and anisotropic displacement parameters for $I4/mmm$ $KCuMnS_2$ from single crystal data at 110 K. All off-diagonal terms are equal to zero.

Atom	Wyckoff Site	x	y	z	$U_{11}(\text{Å}^2) = U_{22}(\text{Å}^2)$	$U_{33}(\text{Å}^2)$
K	2a	0	0	0.5	0.0118(4)	0.0158(7)
Cu/Mn	4d	0.5	0	0.75	0.0071(2)	0.0153(3)
S	4e	0.5	0.5	0.35607(9)	0.0071(3)	0.0121(5)

$T_N = 160.5(1)$ K and a critical exponent of $\beta = 0.334(3)$, which is close to the β of a 3D Ising system (0.3264).

From the propagation vector of $\mathbf{k} = (\frac{1}{2}, \frac{1}{2}, 1)$, three plausible space groups for the antiferromagnetic order were proposed. First, the so-called striped phase is presented in Figure 3.4. Here, the moments on the Mn^{+2} ions align in a stripe pattern with alternating layers oriented antiferromagnetically. This magnetic structure can be fit with magnetic space group C_A/mmm (65.489). A view of the magnetic moments and Mn sites from the c axis (Figure 3.4) shows that the magnetic unit cell (large, blue dashes) can be thought of as a $2a \times 2a$ cell of the chemical unit cell (small green dashes). A further simplified magnetic cell can be adjusted to a $\sqrt{2}a \times \sqrt{2}a$ cell, which then has the symmetry of magnetic space group C_A/mmm.

The other two possible magnetic symmetries are non-collinear ones and are presented in Figure 3.5. Interestingly, these two models give an identical fit to the NPD

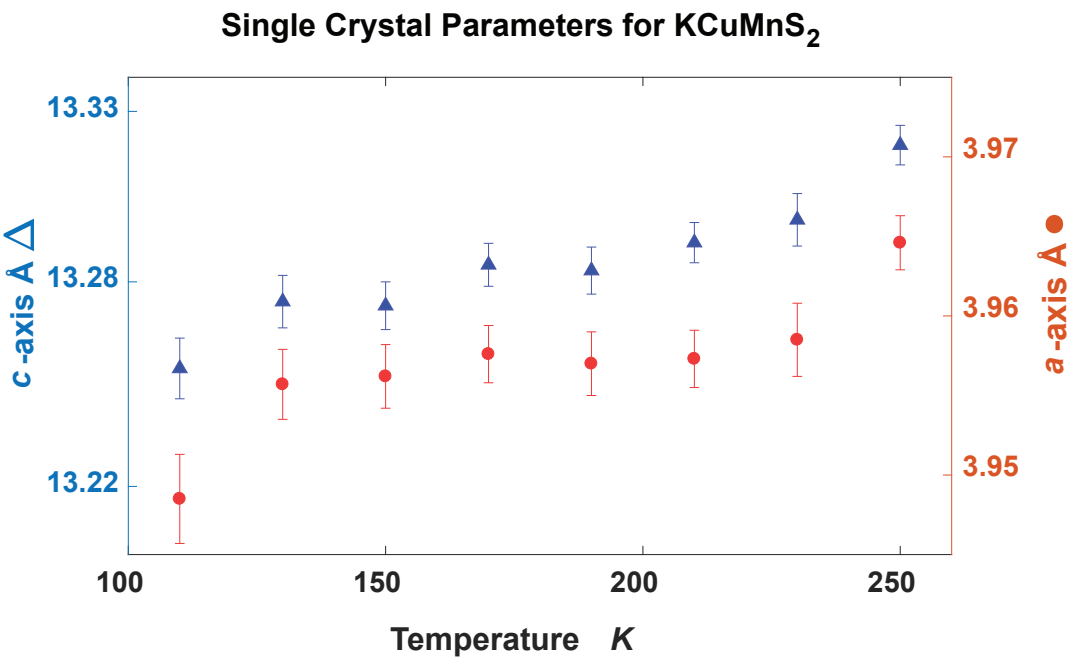

Figure 3.3: Lattice cell parameters for tetragonal $KCuMnS_2$ with respect to temperature from single crystal refinement. Error from standard uncertanties for a 68% confidence interval.

data to that of the striped phase. Magnetic space groups P_C4mmm (123.349) and P_Cmmm (47.255) retain the same unit cell ($\sqrt{2}a \times \sqrt{2}a$) as the proposed C_A/mmm structure detailed above but lead to a non-collinear arrangement of the moments. The structures for P_C4mmm and P_Cmmm provide identically good fits to the NPD data, which is to be expected as they are ultimately the same magnetic structure displaced by $\frac{a}{2} + \frac{a}{2}$. However, P_C4mmm does preserve 4-fold symmetry within the unit cell whereas the other does not. As with the striped structure, the magnetic moments of the Mn cations lie only in the *ab*-plane and are antiferromagnetically coupled between the alternating layers (*i.e.* along the *c*-axis) as shown in Figure 3.1b. When comparing the two possible magnetic structures to one another, it is

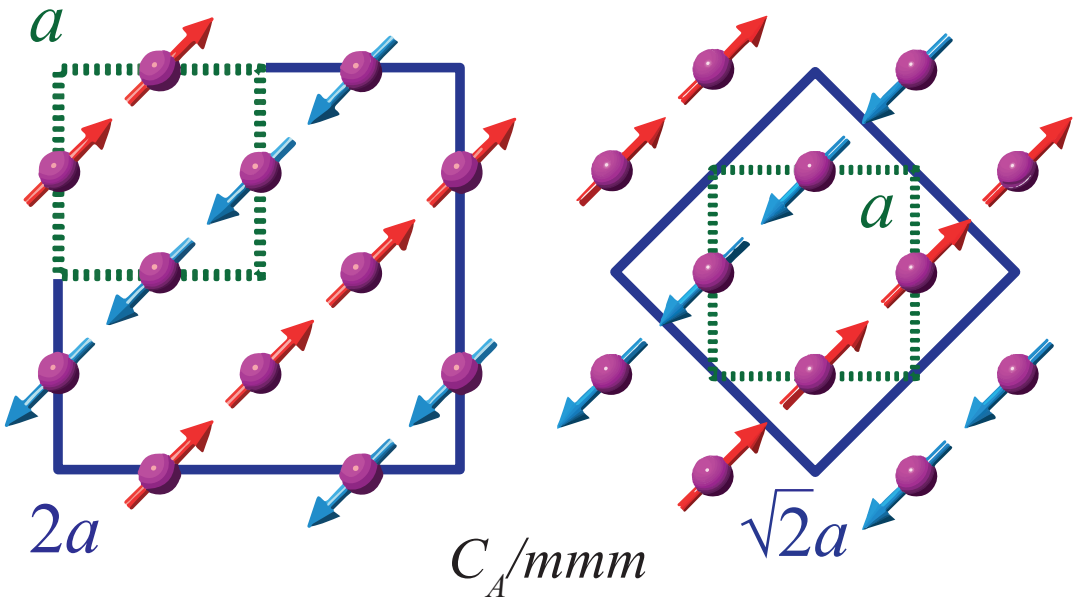

Figure 3.4: Proposed striped phase, C_A/mmm magnetic structure of $KCuMnS_2$ with Mn atoms. Structural lattice is shown with green short dashed line, magnetic cell is shown as both the $2a \times 2a$ (left) and the $\sqrt{2}a \times \sqrt{2}a$ (right) of the structural cell with blue solid line.

important to recall that the occupancy of the magnetic site is only half Mn with no evidence of long-range ordering of Mn and Cu cations.

Since the system remains tetragonal below the magnetic transition temperature, we can only measure the directional cosine angle of the magnetic moment with respect to the *ab*-plane. For all three models, however, the moment is only along the *ab*-plane. At 3.5 K, the moment size refined to 0.462(9) μ_B for the Cu/Mn site. Given that Cu^+ is a d^{10} cation, we can infer that the moment is solely from the Mn cation. Attributing for the occupancy of the site, the moment therefore refines to 0.92(2) μ_B/ Mn^{2+}. This moment size is still approximately 20 % of that anticipated

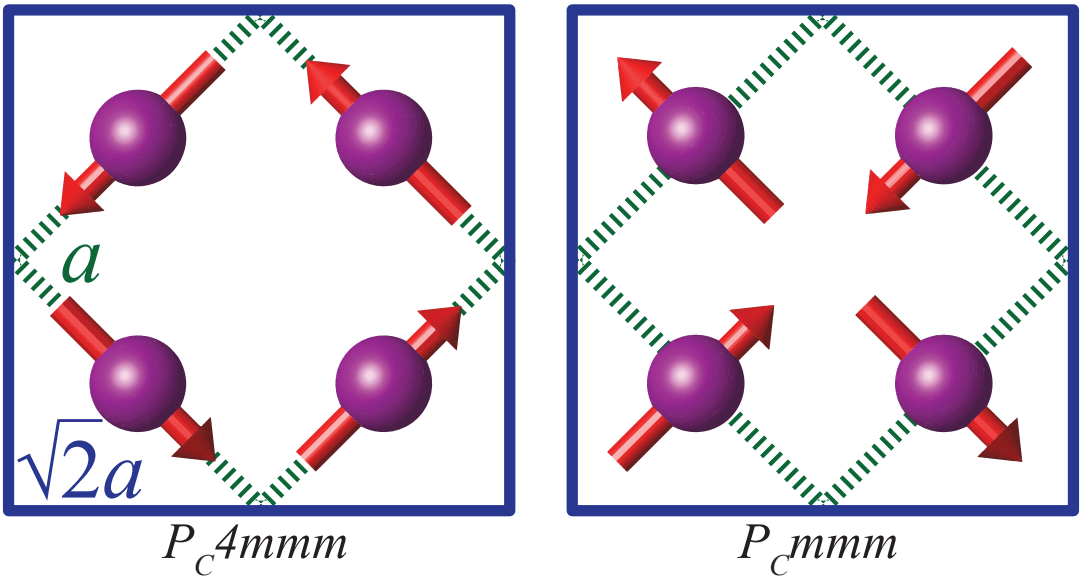

Figure 3.5: Alternate non-collinear magnetic phases for $KCuMnS_2$. The P_C4mmm (left) phase, and the P_Cmmm (right) magnetic structure of $KCuMnS_2$ with Mn atoms. Structural lattice is shown with green dashed line, magnetic cell is shown with blue solid line (rotated 45° from Figure 3.4).

for a d^5 cation. The Curie-Weiss fit for $KLiMnS_2$ also returns a calculated moment that is significantly less than anticipated for a d^5 cation. The calculated magnetic moment of 1.236 μ_B/ Mn^{2+}, seen in Figure 3.7, though larger than that measured for $KCuMnS_2$, is still around 20 % of the 5.9 μ_B predicted for the spin only moment of high-spin tetrahedral Mn^{2+}. Both of these values are actually slightly less than the 1.73 μ_B that would be seen for one unpaired electron which would be the case in low-spin Mn^{2+}. The fact that this moment is larger than that measured for $KCuMnS_2$ is a good indication that the moment being measured in $KCuMnS_2$ is coming exclusively from the Mn^{2+}. Any presence of a magnetic moment originating from copper, would have been fit alongside that of the manganese on the Cu/Mn

site, and would have led to an increased overall moment of the site. The Curie-Weiss fit for $KLiMnS_2$ does predict that it will have an antiferromagnetic transition, though one that will take place below 3 K, and thus, below the base temperature of our neutron measurements.

Upon changing the monovalent cation, the magnetic properties are dramatically altered. At low temperature patterns of the NPD data in Figure 3.2, strong magnetic peaks were observed, however, none of these actually belonged to $KLiMnS_2$. All could be successfully attributed to the magnetic peaks from the alabandite rock-salt cubic structure which is well known for both MnS and MnO. [113–117]. A broad hump that appears centered around 1.25 $Å^{-1}$ could indicate some short-range ordering with a lack of long-range ordering of the magnetic moments. However, this extra scattering could also arise from inelastic scattering and we cannot therefore definitively assign it to a spin glassy state in $KLiMnS_2$. Although powder samples of $KLiMnS_2$ (Figure 3.6b) show a cusp in the magnetic susceptibility below 11 K, this may not lead to long-range order as evidenced by the NPD data. The known Néel temperature for the alabandite found in NPD occurs at approximately 75 K, [113] which rules out this 11 K feature as arising from impurity.

3.3.3 Resistivity and Electronic Structure

Measurements for the resistance of a pressed pellet and resistivity along the *ab*-plane of a single crystal of $KCuMnS_2$ are presented in Figure 3.9. Both samples show primarily semiconducting behavior with a distinct transition near 150 K.

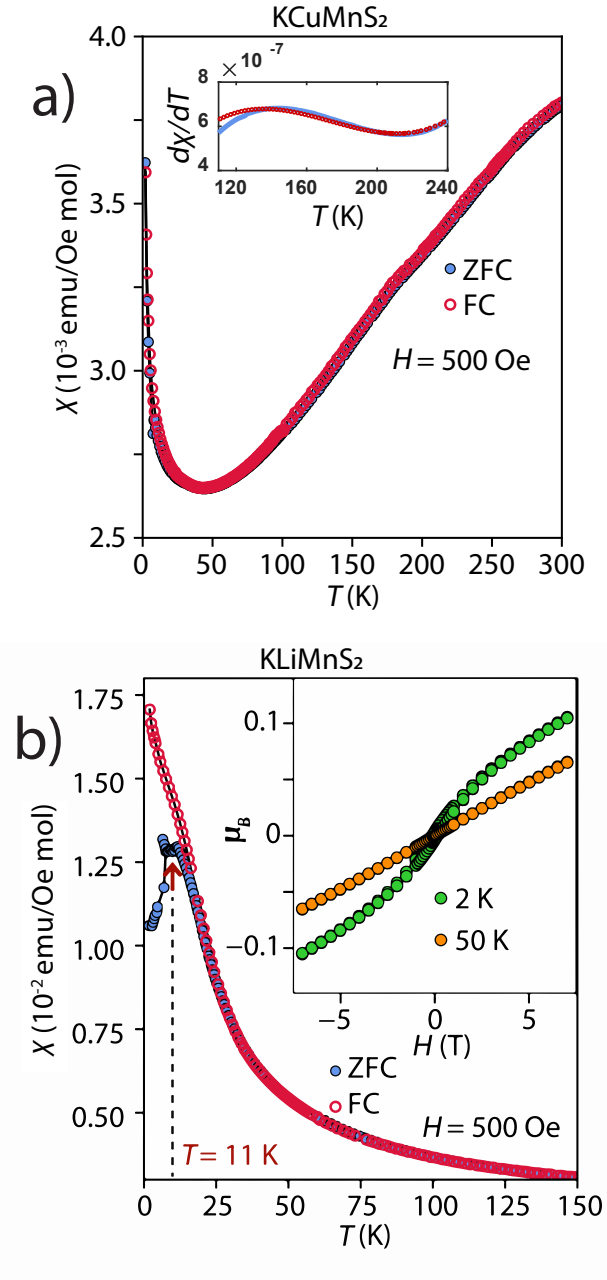

Figure 3.6: Temperature dependent magnetic susceptibility of a) $KCuMnS_2$ and b) $KLiMnS_2$. Inset of (a) is the derivative of the susceptibility and shows a subtle feature around the Néel temperature of 160 K. (Conversion to SI units: 1 Oe = $(1000/4\pi)$ A/m, 1 emu/(mol Oe) = $4\pi\ 10^{-6}$ m^3/mol)

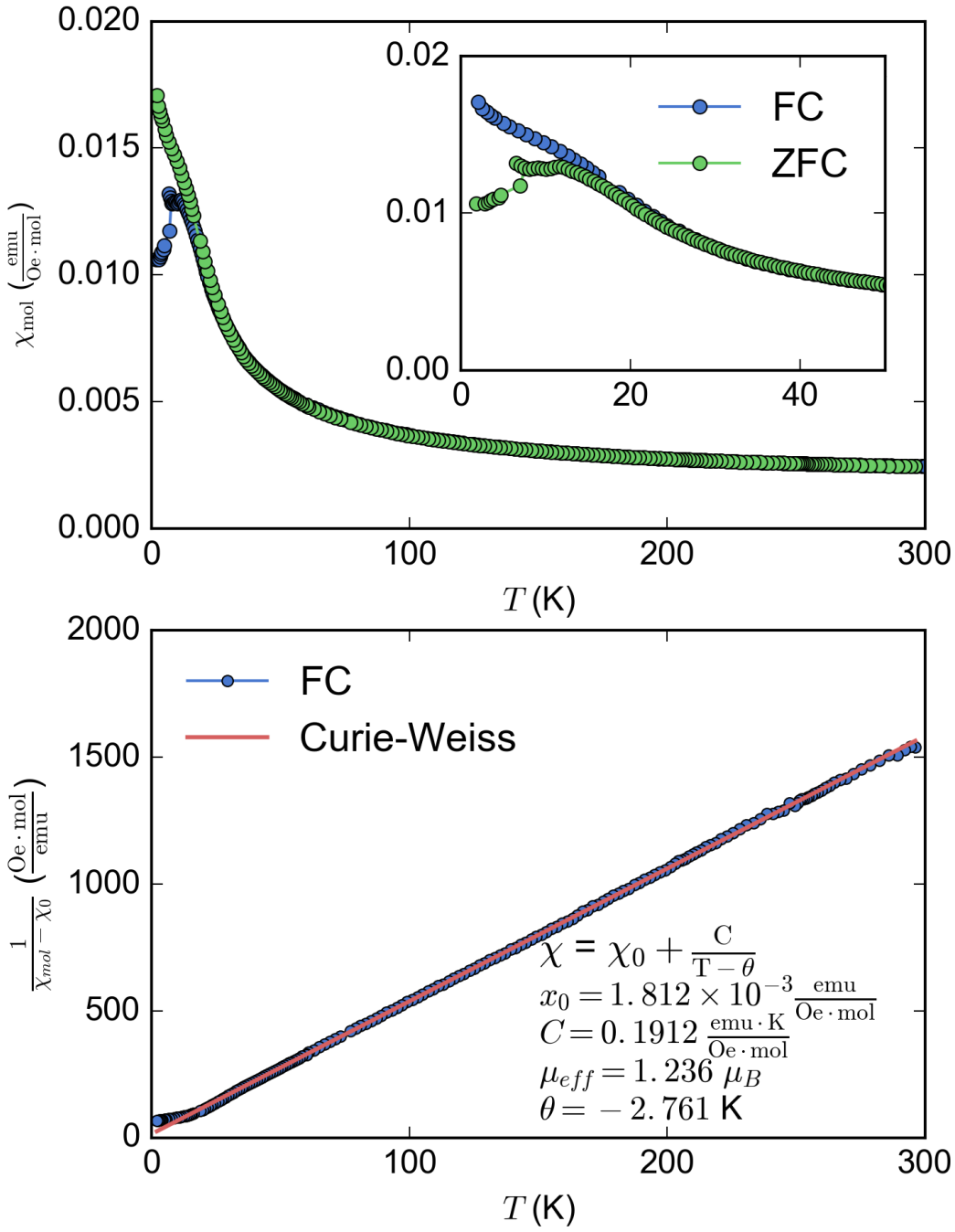

Figure 3.7: Extended magnetic susceptibility of $KLiMnS_2$ (top) and the Curie-Weiss fit of $KLiMnS_2$ (bottom) showing a calculated magnetic moment of 1.236 μ_B/ Mn^{2+} and a Weiss constant of -2.761 K.

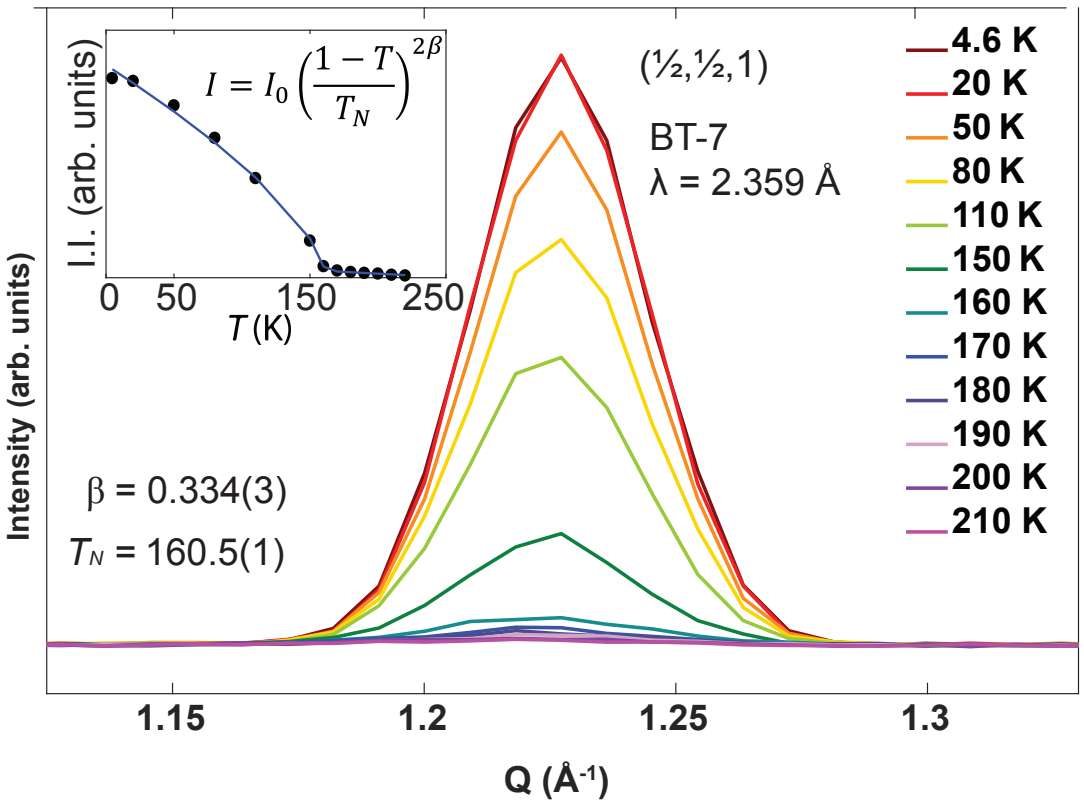

Figure 3.8: Temperature dependence of a magnetic Bragg peak in a single crystal sample of $KCuMnS_2$ from neutron diffraction. (inset) The integrated intensity of the peak is plotted versus temperature in order to fit the magnetic order parameter. From the least-squares fit we extract a Néel temperature close to 160.5(1) K and a critical exponent β of 0.334(3).

Below this transition, both samples exhibit metallic-like behavior since resistance (resistivity) both decrease with temperature until semiconductor behavior resumes at lower temperatures. For the polycrystalline sample, this occurs near 30 K, and for the single crystal near 80 K. The anomaly in the transport results is more more distinct in the single crystal sample (Figure 3.9 inset), which likely arises from powder averaging, although the transition at lower temperature is more distinct in the

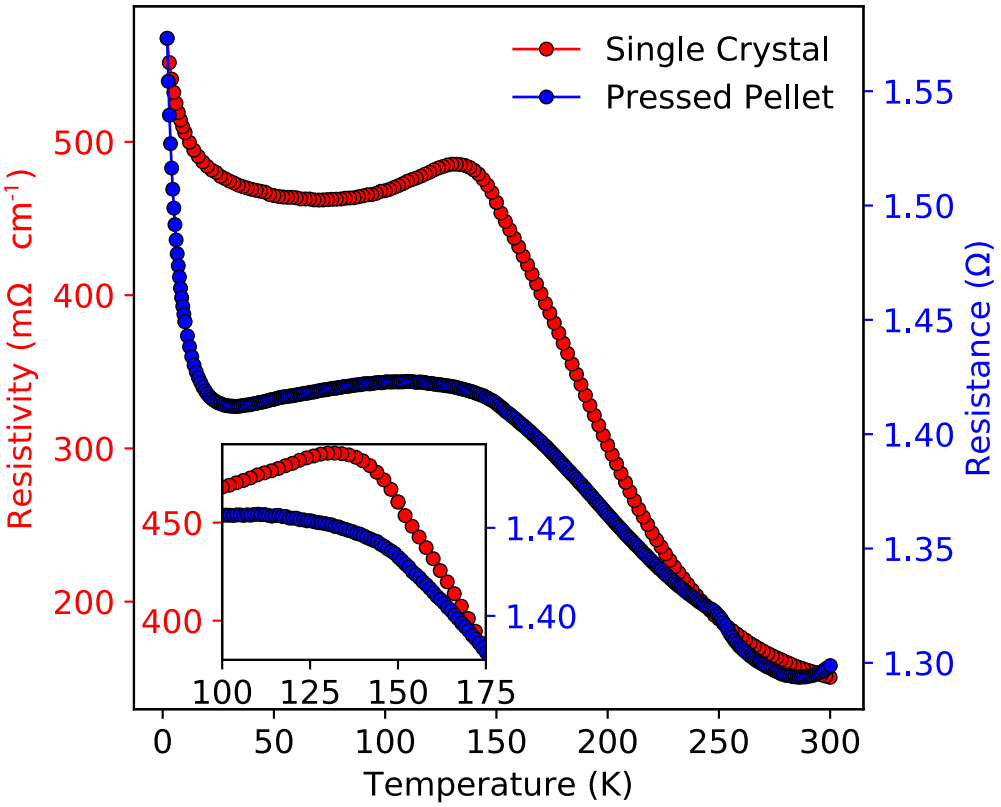

Figure 3.9: Temperature dependent resistance of $KCuMnS_2$ pressed pellet (blue, bottom), and resistivity for a single crystal of $KCuMnS_2$ along the *ab*-plane (red, top). Semiconductor to metallic behavior is observed below 150 K, which is proximate to the onset of long-range magnetic ordering (approximately 160 K), before resuming semiconductor behavior.

pressed pellet sample.

The anomaly in the resistivity of the $KCuMnS_2$ single crystal occurs near the Néel temperature of 160 K, indicating that long-range magnetic order leads to an increase in the conductivity of the sample. This is further supported by the lower temperature transition prominent in the powder sample which resumes

semiconductor behavior around 30 K at the same time as the magnetic intensity from Figure 3.8 begins to saturate. We were not able to measure the resistivity along the c-axis for the single crystal sample of $KCuMnS_2$ due to the sample morphology and were unable to obtain consistent results for $KLiMnS_2$ samples.

Density functional theory (DFT) calculations were also performed for both $KCuMnS_2$ and $KLiMnS_2$ to help gain a better understanding of the electrical transport properties. The dispersion curve of the electronic states near the Fermi level at along major symmetry directions and density of state (DOS) from DFT for the simple layered checkerboard Néel type magnetic structure in Figure 3.13 can be seen in Figure 3.10 for both compounds. Unsurprisingly, given that the all the cations have either full or half-full shells, the electronic DOS shows both to be semiconductors with band gaps near 0.5 eV for $KCuMnS_2$ and 0.8 eV for $KLiMnS_2$. Since the Fermi-level is on the edge of the valence band for both compounds, these materials would be more susceptible to hole doping to tune the electronic properties. The local density of states for both compounds, shown in Figures 3.11 and 3.12, clearly shows that the conduction band for both compounds is comprised of the manganese d orbitals, while the valence band is sparsely populated near the Fermi level by the sulfur p and manganese d orbitals, specifically the p_x and d_{yz}. This indicates that even though no resistance data was able to be retrieved for $KLiMnS_2$, it should have similar electrical properties to $KCuMnS_2$.

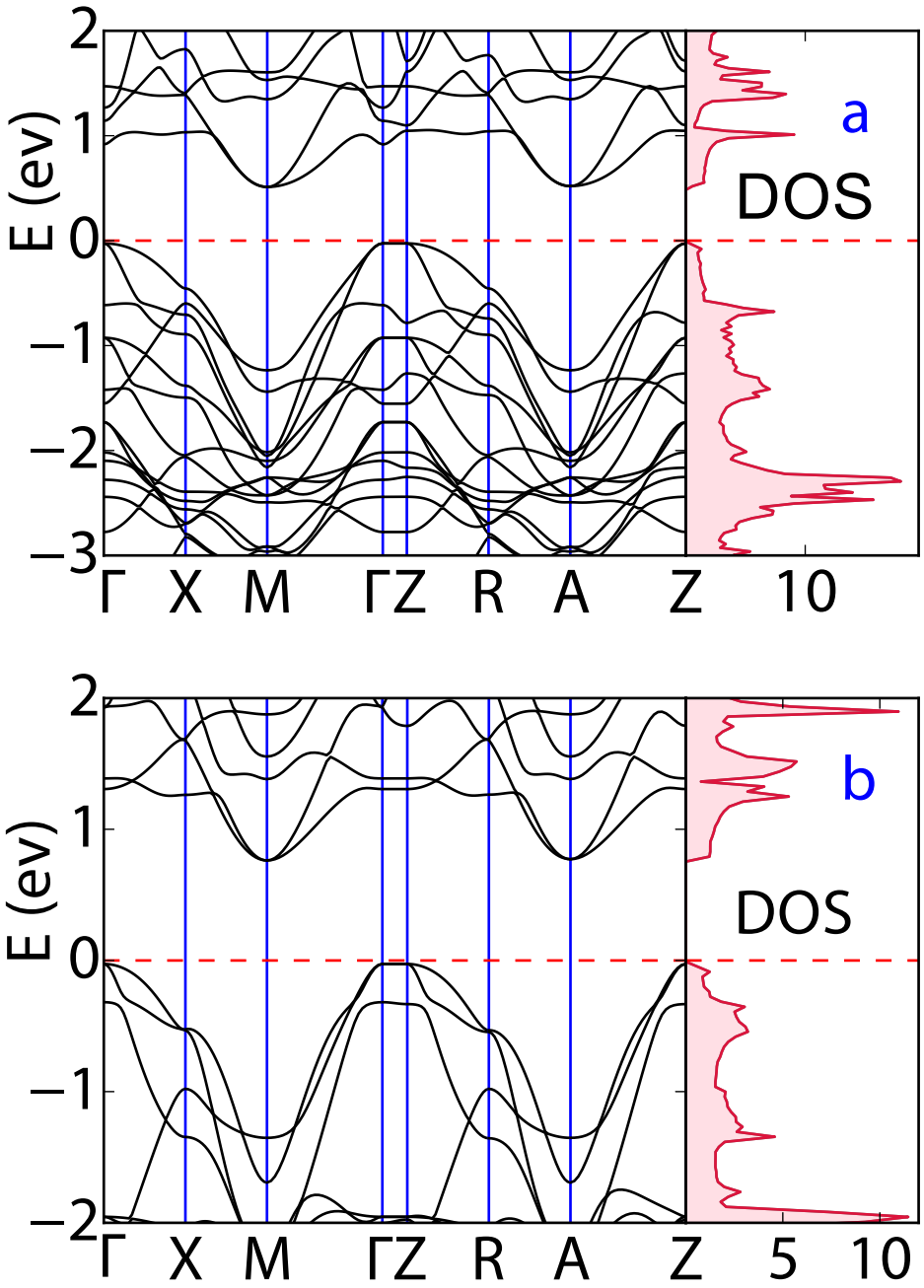

Figure 3.10: Dispersion curves and DOS of the electronic states near the Fermi-level for $KCuMnS_2$ (a) and $KLiMnS_2$ (b) showing the Fermi-level on the edge of the valence band.

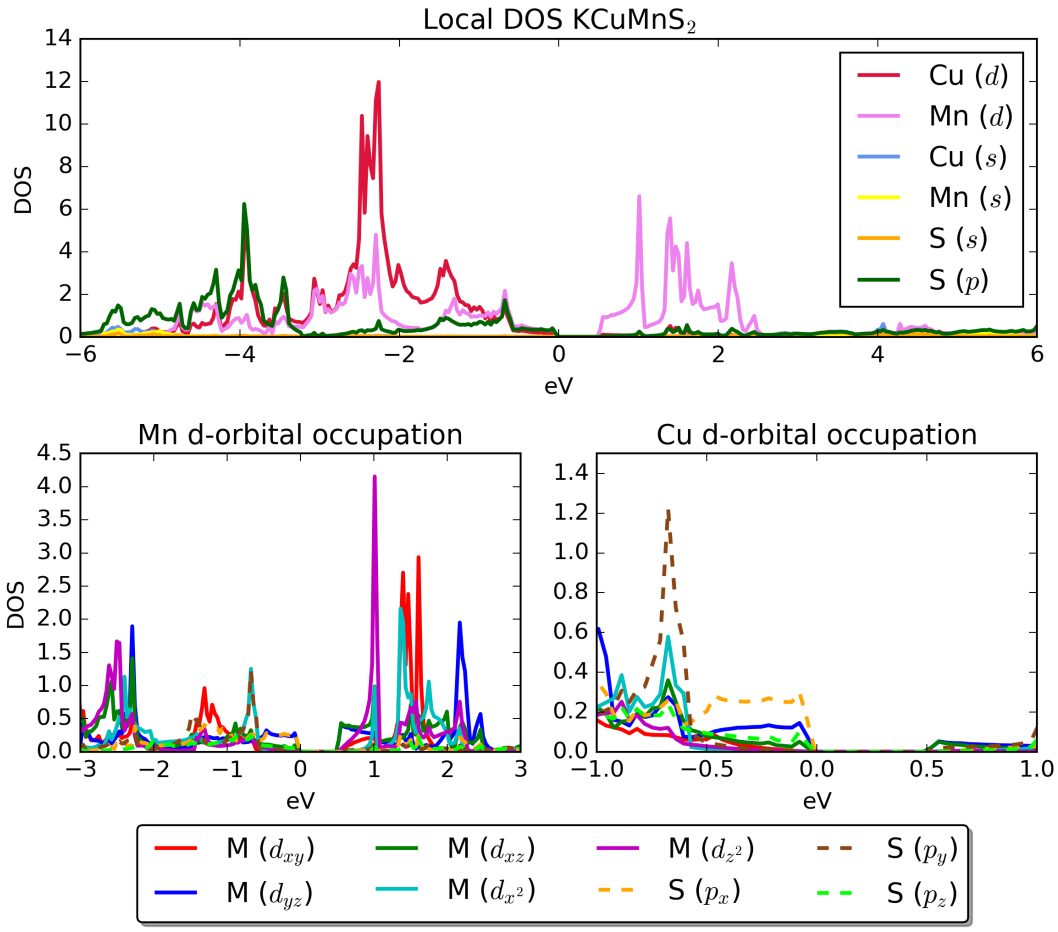

Figure 3.11: Local density of states for $KCuMnS_2$.

3.3.4 Structure and bonding

With both sulfides crystallizing in the $I4/mmm$ space group, the only refineable structural parameter is the z-position for the 4e site of the sulfide anion. The effective ionic radii of Li^+ (0.59 Å) and Cu^+ (0.60 Å) [118] are very similar, yet the nature of the monovalent cation greatly effects the z-position of the sulfide anions and cell parameters. The S–M–S tetrahedral bond angles better illustrate this drastic change. While the CuS_4 tetrahedron has nearly ideal values of 109.22(4)° and 109.60(2)° for the S–M–S bond angles (from single crystal XRD at 250 K), the LiS_4

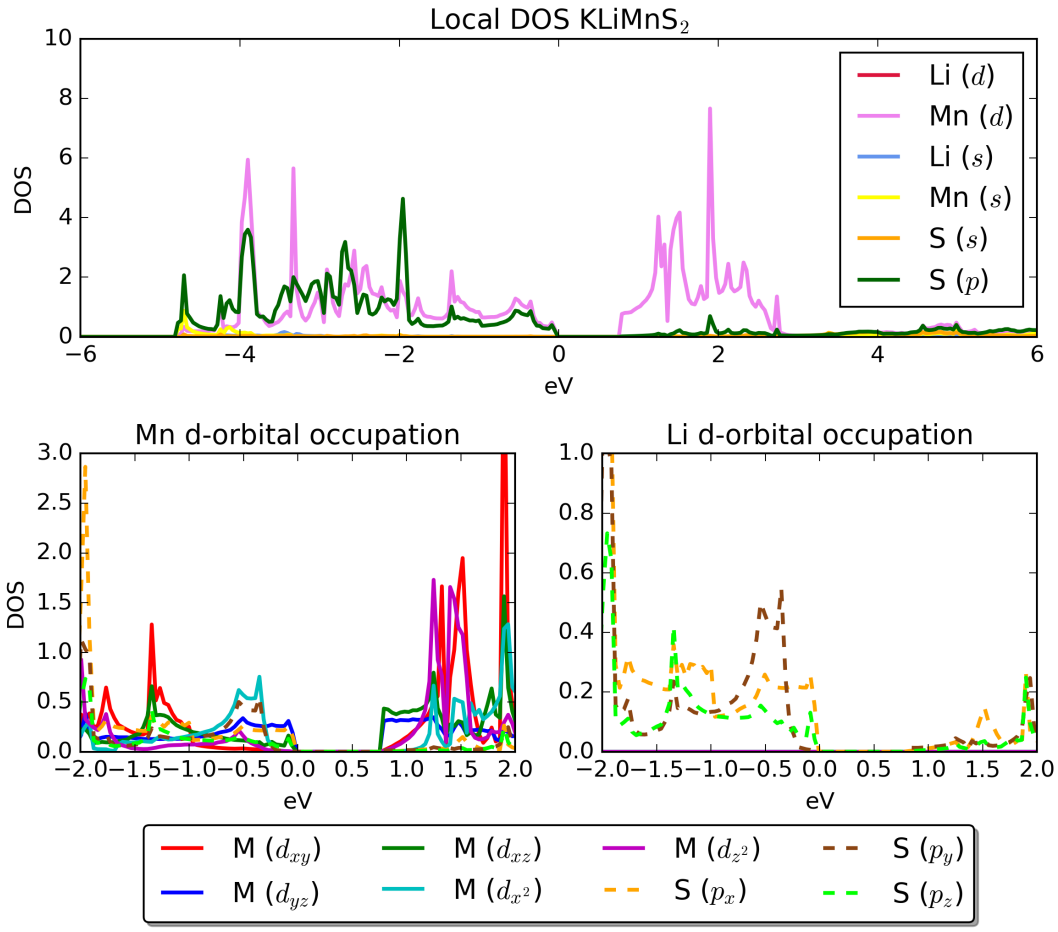

Figure 3.12: Local density of states for $KLiMnS_2$.

tetrahedron has bond angles of 112.6(2)° and 107.94(8)° (from NPD data at 200 K). Therefore, the ionic radii do not play a role in determining the key structural parameter in this system, but rather the electronics may be playing the larger role. A full $3d^{10}$ shell as opposed to a full $1s^2$ shell could more effectively hybridize with the sulfur $3p$ levels due to better matching of the orbital energy levels.

Because of the symmetry constraints of the crystal system, there is only one unique M–S bond distance in this system. Interestingly, while the S–M–S bond angles were drastically changed by the nature of M, the bond distance is unaffected.

In KMMnS$_2$, the M–S interatomic distance is given by 2.4270(7) Å and 2.431(2) Å for M = Cu and Li, respectively. These distances are close to that of 2.439(3) Å reported by Bronger et al. [107] Nevertheless, the change in S–M–S bond angle causes an increase of the a-parameter and decrease of the c-parameter for M = Li with respect to M = Cu. This is due to the fact that the tetrahedral angle within the ab-plane increases, while that out of the plane decreases.

We conclude that the relevant structural changes from diffraction patterns demonstrate that ionic radii are not the only determining factor in these quaternary sulfides. The nature of M is quite important due to the orbitals that are engaged in bonding. The nearly ideal tetrahedron created by the Cu^+ will constrain the magnetic Mn^{2+} while this is not the case for Li^+. Covalent bonding is strengthened between metal and sulfur for the case of $M = Cu^+$. Undoubtedly, this will have an effect on the crystal field splitting energies for the d^5 cations and the electronic structure, which we discuss next.

3.3.5 Electrical transport

Although transport measurements indicate that both sulfides are semiconducting, only the M = Cu sample displayed a sufficiently small band gap to measure resistivity down to base temperature. It is apparent in the temperature dependence of the single crystal sample of KCuMnS$_2$ that the anomaly in the resistivity is related to the antiferromagnetic transition. A similar anomaly has been found in the parent superconductor Fe$_{1+x}$Te for $x = 12\%$, whereby the T_N causes an anomaly in

the semiconductor-type resistivity measurement. [119–124] This has been attributed to scattering from spin fluctuations that persist below the ordering temperature, and a similar phenomenon may be occurring with $KCuMnS_2$.

The predicted band gaps in $KCuMnS_2$ and $KLiMnS_2$ are 0.5 eV and 0.8 eV, respectively. Likely, the nearly ideal tetrahedral environment in $KCuMnS_2$ causes more orbital overlap between the Cu/Mn metal and S anions, thereby increasing the band width of the conduction band. Another notable difference in the calculated band structure is that the Cu *d*-states create more electronic states between 0 and -2 eV as evidenced by the dispersion curves in Figure 3.10. Therefore, a distribution of electronic DOS near the Fermi level is created by these extra states in the Cu compound.

The similarity of our $KCuMnS_2$ structure with that reported by Oledzka is in contrast with the noticeable differences between the resistivity measurements reported here and those of Oledzka et al. [47] The previous results by Oledzka are consistent with that of a highly doped, or degenerate semiconductor, with metallic behavior above 80 K, but with resistances too high to be called metallic. While the magnitude of the resistivity for each report is relatively consistent, even with the differences between how the samples were prepared for measurement (sintered vs pressed pellet and single crystal), our results are more in line with the $ACuCoS_2$ semiconductors also prepared by Oledzka et al. [51] Apart from the reduction in resistivity during the onset of the magnetic moment, not seen in $ACuCoS_2$, our resistivity measurements show semiconducting behavior.

The difference in the resistivity measurements between the two reports for

$KCuMnS_2$ can be explained by the seemingly trivial differences between our synthesis and that of previous work. [47] washed the as-recovered powders with water, whereas we washed the excess flux with methanol. Washing with water could have removed some of the K^+ ions in the structure, as can readily happen with other known 122-type chalcogendies such as KCo_2Se_2. [125] Removal of K^+ from the lattice would oxidize the metal and therefore effectively hole doping the system. With sufficient lowering of the Fermi-level into the valence band, the compound may express metallic behavior. This semiconducting behavior is also present in the ACuFeS$_2$ compounds by Oledzka, though the values for resistivity were too great to measure below 200 K. The deviation from the predicted metallic behavior from electronic band calculations are partially explained by a non-ideal tetrahedral environment for the Cu/Fe site.

3.3.6 Comparison of AFM models

Although we could not determine the definitive antiferromagnetic structure of $KCuMnS_2$ from neutron diffraction, other evidence may point in favor one structure over the other. First, the stripe order would break 4-fold symmetry in the compound, as often happens with the 122-type iron arsenides. [126] In those parent-phases of the superconductors, the T_N is either coincident or near a tetragonal-to-orthorhombic phase transition. [4, 26, 127–129] Likewise, the $Fe_{1+x}Te$ system displays a structural phase transition near the Néel temperature. The above-mentioned compounds all display either single-stripe or double-stripe antiferromagnetic order. [120, 121] How-

ever, this phase transition is clearly not the case in the quaternary 122-sulfides studied here. The lack of a structural transition upon AFM order strengthens the case for the non-collinear structure. The critical exponent of $\beta = 0.331(5)$ for the magnetization from the neutron measurements is closest the value found for an Ising spin system in a three-dimensional lattice (3D). A similar non-collinear structure was determined for the Mott-insulator $La_2O_2Fe_2OSe_2$, which was found to be a 2D Ising system. [130]

Clearly some AFM order is needed to explain the semiconducting behavior, and the DFT results offer guidance on the true state in the $KCuMnS_2$ system. The band structure and DOS in Figure3.14 predict $KCuMnS_2$ to be metallic if AFM order is excluded. The AFM model (layered checkerboard) led to the electronic DOS of Figure 3.10, which shows $KCuMnS_2$ to be semiconducting. While simple to construct, this model is obviously wrong according to the neutron diffraction results. Therefore, we performed additional band structure calculations in order to understand how other magnetic structures may influence the electric properties. We constructed two additional AFM models. One model has the Cu and Mn cations ordered in a double striped fashion in order to construct the striped AFM order on the Mn site. The other model has Mn arranged so that it forms a tetramer that would support the non-collinear AFM models of Figure 3.5. Both models have a 2 $\times$ 2 magnetic unit cell and are illustrated in Figure 3.3.

In the case of $KCuMnS_2$, the two types of AFM order (striped and non-collinear) do not lead to qualitatively different electric properties from each other. However, their electronic DOS are quite different. As shown in the DOS of Figure

3.14, for the striped model, it appears that $KCuMnS_2$ is not quite a semiconductor but instead a metal with a very small Fermi surface. The Fermi level just crosses the top of the valence band. In the non-collinear AFM model, the same is true but there are some extra states near the valence band that would suggest a smaller band gap if it was a semiconductor. The total energies from the band structure calculations are presented in Table 3.3 which shows the striped order to be the lowest energy of all the AFM models. We must be careful in over interpreting these results, however, in that the Cu and Mn cations always remain disordered in $KCuMnS_2$ and the DFT results only reflect the case for particular types of cation ordering. From these limited calculations, however, the striped order would seem to be favored.

Determination of the correct magnetic structure could be aided by future experiments on the system. The most straightforward approach would be single crystal transport measurements such as angle-dependent magnetoresistance and/or angle dependent magnetization measurements. Furthermore, a comprehensive way to understand the structure would be polarized single crystal or powder neutron diffraction which would definitively allow for the magnetic structure to be solved.

3.3.7 Comparison with other 122-systems

Once again, it is interesting to compare the results here to those found previously on $KCuMnS_2$. Oledzka et al. observed a broad plateau just below room temperature for $KCuMnS_2$, which is attributed to short-range antiferromagnetic behavior. [47] They proposed that the suppression of magnetic ordering was due to

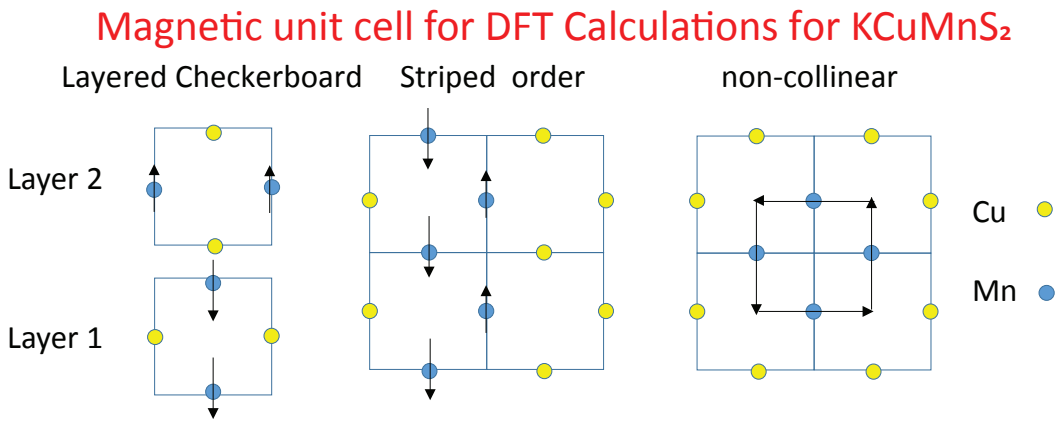

Figure 3.13: Magnetic structure used for DFT and DOS calculations for both of the proposed magnetic structures, as well as the non-magnetic case.

Table 3.3: Total energy for the various nonmagnetic and magnetic cases for $KCuMnS_2$.

Order Type	Total Energy/Atom (eV)
Nonmagnetic	-190.712528
Layered Checkerboard	-205.371127
Striped Order	-205.876911
Pinwheel (non-colinear)	-205.122159

the disruption caused by the Cu^{+} ions in the square lattice even though there may be strong antiferromagnetic exchange between the Mn^{2+} ions. However, we did not find such a divergence between the ZFC and FC curves in our magnetic susceptibility measurements. Again, this may be due to how we processed the sample after

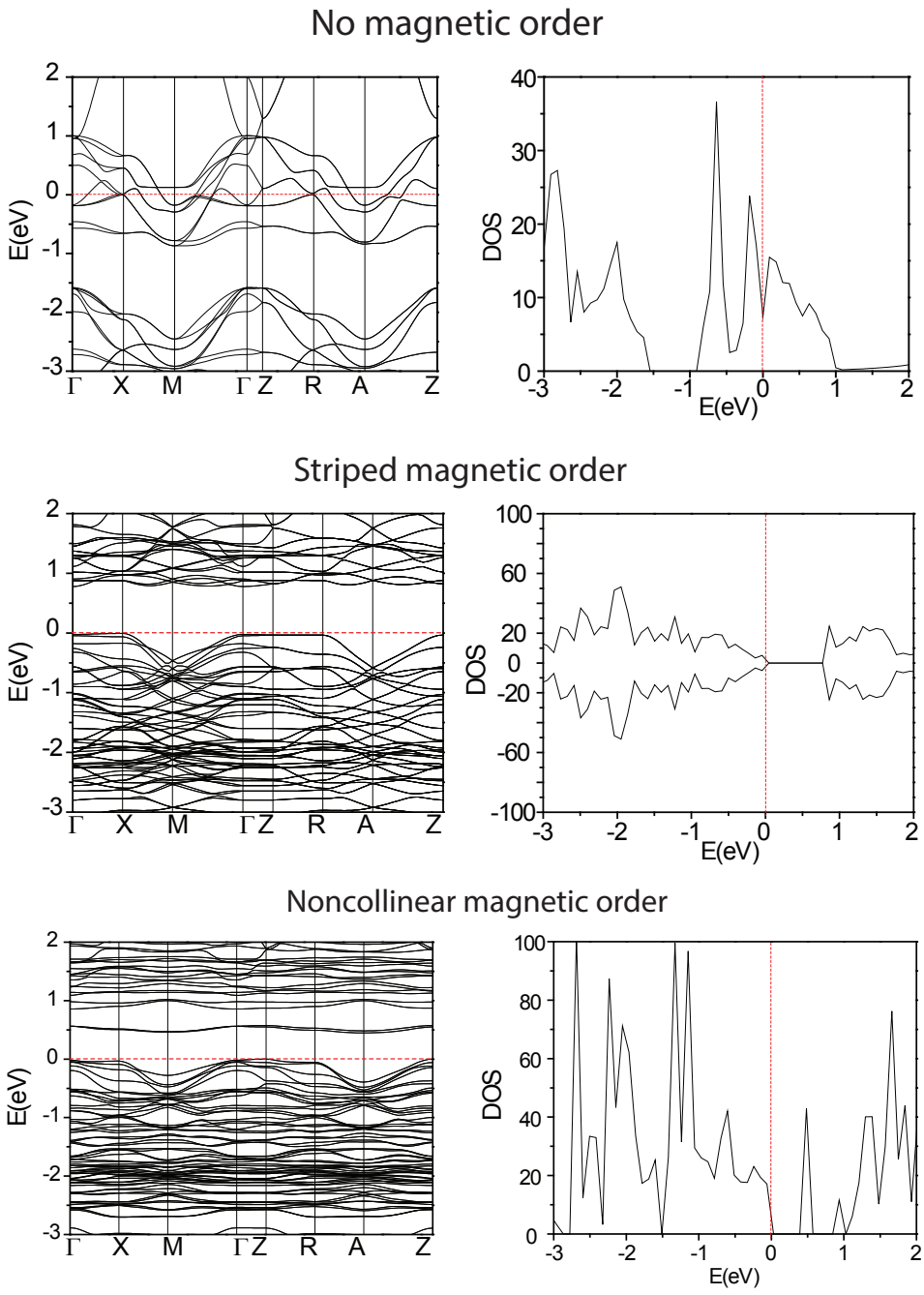

Figure 3.14: Dispersion curves and DOS of the electronic states near the Fermi-level for $KCuMnS_2$ for the non magnetic structure, and both proposed magnetic structures.

synthesis and the spin glassy behavior may arrive from vacancies rather than the random distribution of Cu^{+} cations. The random distribution of the M cations in the structure leading to clusters of Mn^{2+} is also noted as the cause for the reported divergence between ZFC and FC below 38 K, and attributed this to a spin-glassy transition. [47] However, such divergence was absent from our current measurements with the $KCuMnS_2$ system, suggesting lack of the spin-glass phase.

We also consider the closely related $KCuFeS_2$ and $KCuCoS_2$, which are isostructural. Oledzka found $KCuFeS_2$ to also be an antiferromagnet with a T_N of 40 K, although no neutron diffraction was ever carried out to investigate the possible order. [47] While a split in their ZFC and FC curves at low temperatures may suggest some spin glassiness from the random distributions of Fe and Cu cations, this explanation would not be consistent with the case of $KCuCoS_2$. In this compound the Co and Cu cations are also randomly distributed, yet the system undergoes a ferromagnetic transition near 120 K. [51]

Spin-glass behavior is not common for most of these 122-type quaternaries. $KCuCoS_2$, despite having the same random orientation of magnetic ions the d^8 Co instead undergoes a ferromagnetic transition around 120 K. In the case of $KCuCoS_2$, it is believed that c-axis interactions dominate above the T_c while ab-plane interactions make the overall order ferromagnetic below the T_c. This T_c can change due to the temperature of synthetic conditions similar to ours, dropping drastically to 50 K when the reaction temperature is increased from 720 °C to 900 °C possibly attributed to changes in the Co/Cu distribution, or sulfur vacancies.

Spin-glass behavior is also not observed in the AMn_2Pn_2 compounds that ex-

hibit antiferromagnetic behavior, possibly higher than room temperature. [109,131–133] Their G-type order indicates Mn^{2+} in the high-spin tetrahedral coordination. This is in contrast to our NPD providing a 0.92(2) μ_B/Mn^{2+}, which indicates low-spin Mn^{2+} in a tetrahedral environment. Indeed this leads our results to more similarly resemble the class of isostructural $A$$Mn_2Pn_2$ compounds. $BaMn_2Sb_2$ and $BaMn_2As_2$ have both shown themselves to be G-type collinear antiferromagnets, with no c-component to the magnetic moment. [109,131] The magnetic susceptibility can also be highly anisotropic with respect to the ab-plane for these $A$$Mn_2Pn_2$ compounds, featuring a clear feature in the susceptibility at the Néel temperature when measured parallel to the c-axis, that is much less pronounced when measured in the ab-plane. [109,112] A strong dominating ab-plane contribution to the magnetic susceptibility could contribute to the presence of only a subtle feature in our powder samples.

The notable difference here is that while $BaMn_2Sb_2$ has a T_N of 118 K, the T_N of $BaMn_2As_2$ is well above room temperature at 625 K. [132] While the magnitude of the magnetic moments for the $A$$Mn_2Pn_2$ compounds is less than the nominal 5.0 μ_B/Mn for high spin Mn^{2+}, the values of roughly 3.75μ_B/Mn are still well above that for $KCuMnS_2$. [110,134–137] While this decrease for the pnictides is attributed to the strong spin dependent hybridization of the Mn 3d and As 4p orbitals, the reduction for $KCuMnS_2$ is likely similar to that of the Fe-122 compounds due to the itinerant nature of the magnetism. It is this itinerant nature that could help $KCuMnS_2$ resemble the high T_N pnictides. Our magnetic susceptibility data hinted at a high (above our room temperature capabilities) T_N antiferromagnet, though

the lack of unindexed NPD peaks refutes the presence of any long-range ordering above 160 K.

3.4 Additional neutron diffraction experiments

The work contained within this section is currently unpublished.

3.4.1 (0.5, 0.5, 0) Reflection seen with MACS

When the single crystal of $KCuMnS_2$ was aligned on the Multi Axis Crystal Spectrometer it was determined that the single crystal used for these neutron scattering experiments was in fact two crystals grown together. The alignment of one crystal along major reflections such as the (-1, -1, 0) peak, showed additional reflections that were unaccounted for. By rotating the crystal in the (H, K, 0)-plane, the unaccounted for reflections were able to be aligned with similar reflections pre-rotation. The reflection at (-0.8, -0.6, 0) becoming the reflection at (0, 0, 0) etc. indicating the existence of two crystalline domains in the sample. These crystals were oriented in the same L direction, but were offset from one another by 50 degrees in the (H, K, 0)-plane. Figure 3.15 shows the alignment of both crystals in the twinned sample.

The orientation of the sample aside, alignment along the major reflections also showed additional reflections that were unaccounted for in previous experiments. The magnetic domain previously discussed with Néel temperature of 160 K has reflections at (0.5, 0.5, 1) and (0.5, 0.5, 3). These can be seen in the BT-7 single

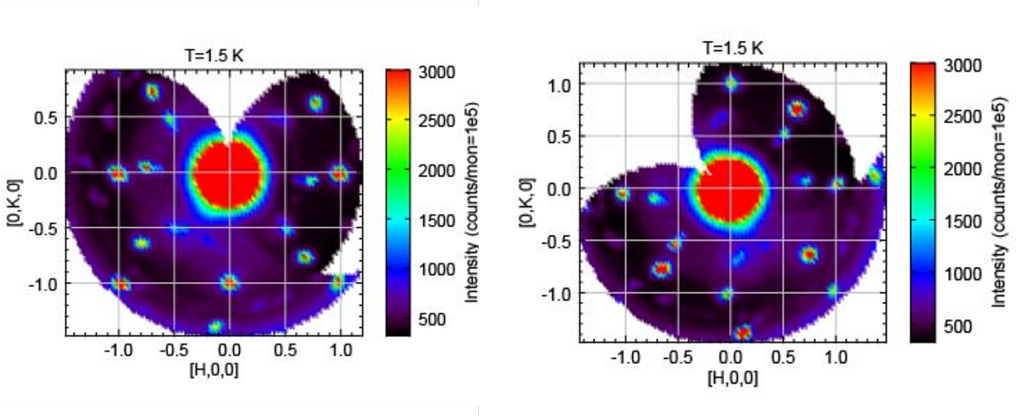

Figure 3.15: MACS scattering showing that the $KCuMnS_2$ crystal used for scattering is, in fact, two crystals grown together with an offset in the (H, K, 0)-plane by 50 degrees. One crystal is aligned in the left image, the other is aligned in the right image.

crystal diffraction scan in the (0.5, 0.5, L) direction in Figure 3.16. Both of these magnetic peaks disappear above the Néel temperature of 160 K in the scan taken at 180 K, with the remaining peaks being due to the aluminum single crystal mount. Interestingly, there is no indication of any scattering in the (0.5, 0.5, 0) direction in the BT-7 single crystal data, even though there is clearly some intensity from that reflection in the MACS frames. This could be due to a slight misalignment on the BT-7 that would still allow the viewing of the (0.5, 0.5, 1) and (0.5, 0.5, 3) reflections, while missing the (0.5, 0.5, 0) reflection. The weakening of this peak at 180 K as seen in Figure 3.17 indicates some temperature dependence which could indicate that it is due to a magnetic domain.

We also see a very strong reflection at (1, 0, 0), which, like the (0.5, 0.5, 0) reflection is forbidden for the $I4/mmm$ space group. The (0.5, 0.5, 0) could be

the result of its magnetic domain breaking symmetry and allowing the reflection, but the persistence of the (1, 0, 0) at 180 K makes this an unlikely explanation for this. One possibility is that this sample underwent a tetragonal to orthorhombic structural phase transition that is known for these types of compounds that would allow the reflection. [3–5, 22, 25, 29] The reason for not seeing this peak previously could be because the phase transition temperature is between the 6.5 K of the BT-1 measurements and the 1.5 K at which the MACS data was taken. Though this would not explain the persistence of the peak at 180 K.

3.4.2 Temperature Dependence of (0.5, 0.5, 0) Reflection [Different than the (0.5, 0.5, 1)]

The reflection seen at (0.5, 0.5, 0) for both crystalline domains indicates another magnetic reflection that was not seen in the original NPD. Not only was this reflection, which can be seen in the MACS scattering at 1.5 K, not seen in the original NPD, but it is still present, if difficult to see in the comparison in Figure 3.17, at 180 K on MACS. This is well above the onset temperature of the primary magnetic domain previously mentioned possessing a (0.5, 0.5, 1) reflection. The presence of this reflection above the Néel temperature of 160 K for the previously discussed magnetic domain, indicates that this reflection is due to an entirely different magnetic domain in this compound.

In order to help elucidate the nature of this magnetic domain, we were able to test our single crystal sample on the Spin Polarized Inelastic Neutron Spectrom-

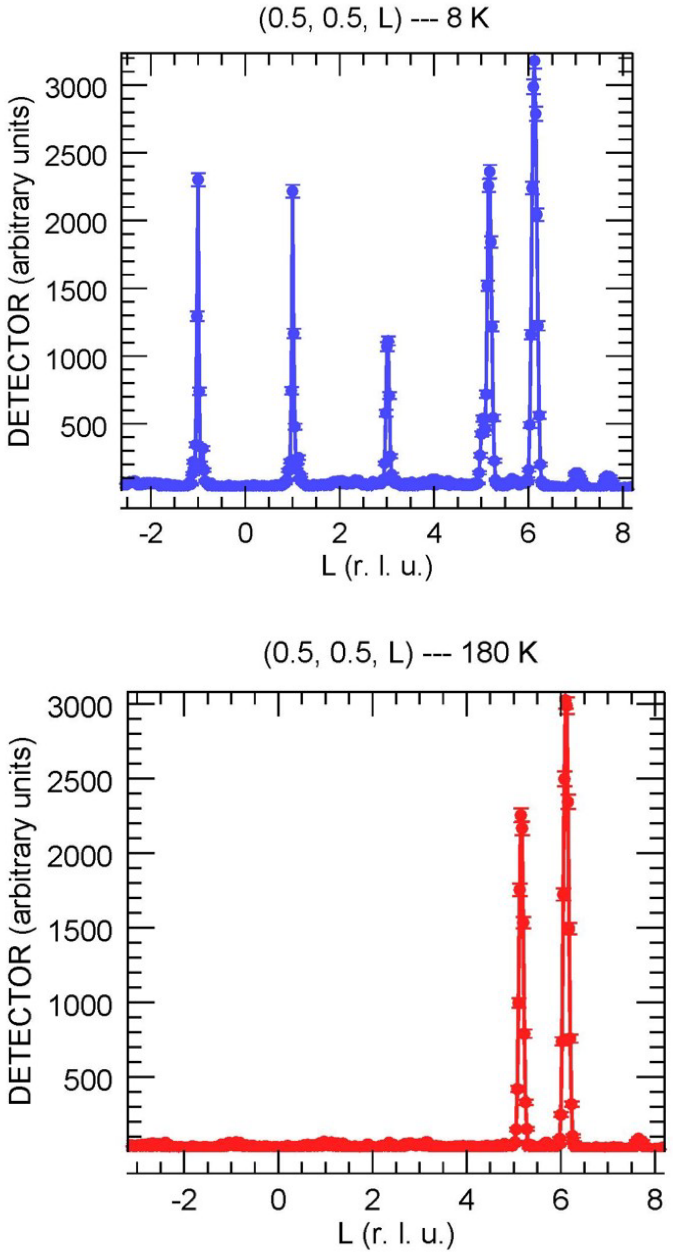

Figure 3.16: BT-7 single crystal scans for $KCuMnS_2$ along (0.5, 0.5, L) at 8 K and 180 K showing magnetic peaks at (0.5, 0.5, 1) and (0.5, 0.5, 3) that disappear at 180 K. The additional peaks still present at 180 K are due to the aluminum single crystal mount.

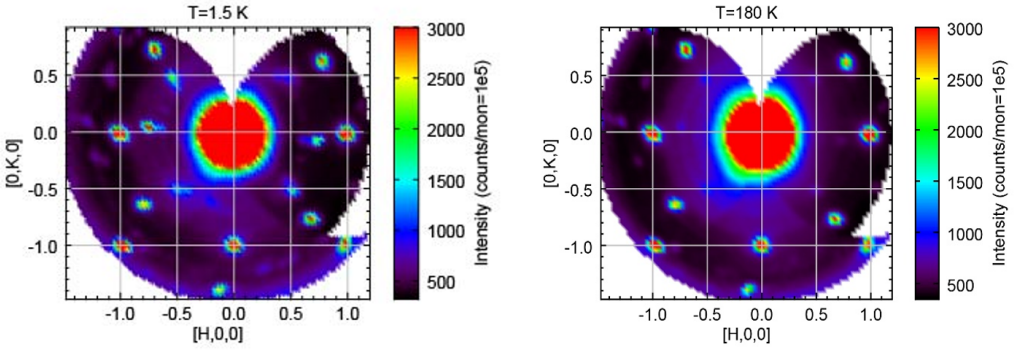

Figure 3.17: MACS scattering at 1.5 K and 180 K showing additional peaks at (0.5, 0.5, 0) not previously seen for $KCuMnS_2$, and above the transition temperature of the (0.5, 0.5, 1) peak.

eter (SPINS). Scans were taken along the (H, 0.5, 0) direction from 100 to 230 K which can be seen in Figure 3.18. These scans clearly show the reflection at (0.5, 0.5, 0), which persists with increasing temperature until roughly 210 K. The most noticeable feature of the chart is the fact that the highest intensity is not at the lowest temperature recorded, as one would expect for a magnetic domain. Instead, the intensity appears to increase with temperature before dropping off towards the onset temperature. Fitting the intensity of the reflection with respect to temperature in Figure 3.19 clearly shows the onset temperature of around 210 K and a peak in the intensity around 160 K. While the increase in intensity when lowering the temperature from 210 K can be attributed to the onset of the magnetic moment, the decrease in intensity when lowering the temperature below 160 K could be attributed to competition with the other magnetic domain. With the onset of the (0.5, 0.5, 1) magnetic domain, which has a Néel temperature of 160 K, the intensity

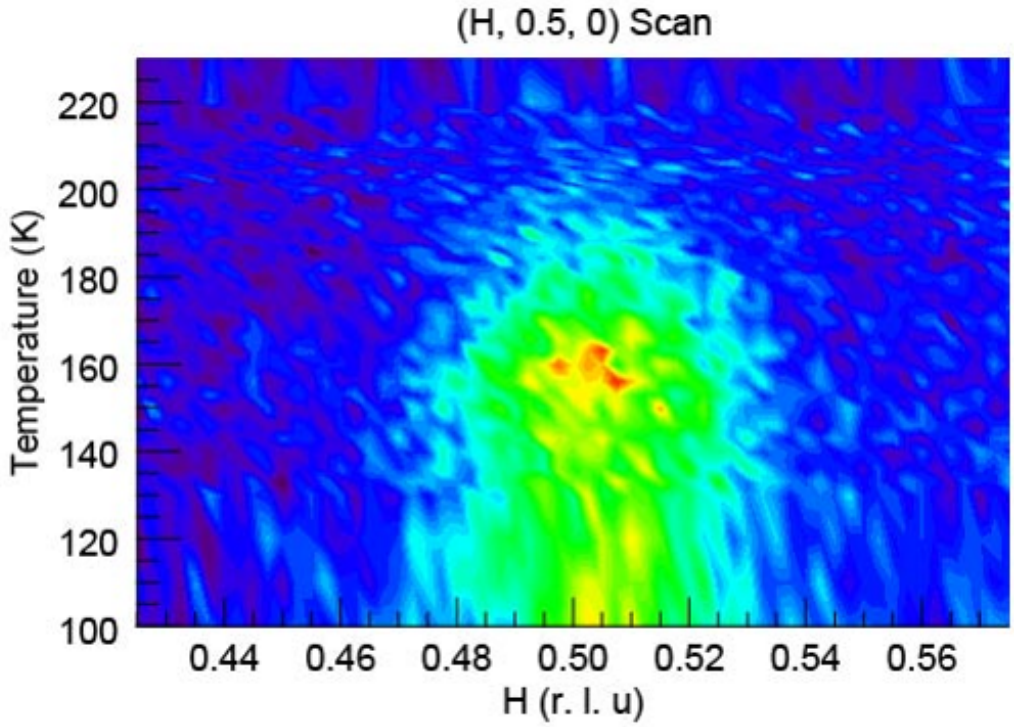

Figure 3.18: SPINS temperature dependent scans of $KCuMnS_2$ along the (H, 0.5, 0) direction, showing the (0.5, 0.5, 0) peak.

of the (0.5, 0.5, 0) reflection decreases. It seems then that these two occurrences are connected and the onset of the (0.5, 0.5, 1) magnetic domain disrupts the formation of the (0.5, 0.5, 0) magnetic domain. This indicates that the (0.5, 0.5, 0) reflection is not the result of some impurity and belongs to $KCuMnS_2$.

3.5 Conclusions

$KCuMnS_2$ and $KLiMnS_2$ were prepared trough high temperature reaction from the respective K and Li carbonates with pure metals under a CS_2 in Ar flow. Single crystals of $KCuMnS_2$ were prepared via a melt of the unwashed powder in an evac-

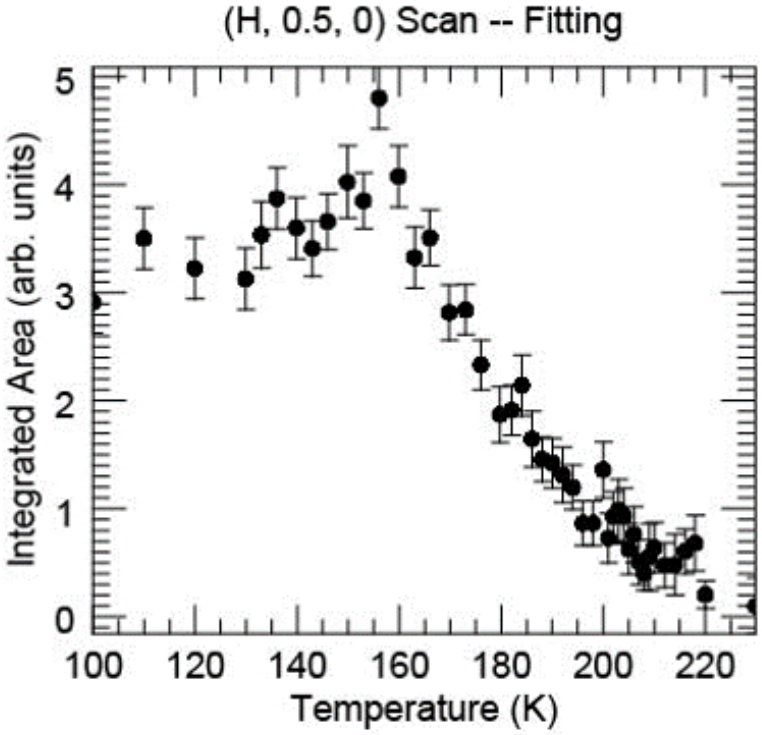

Figure 3.19: Temperature dependence of the (0.5, 0.5, 0) peak of $KCuMnS_2$, showing a peak in intensity around 160 K.

uated ampule. From neutron diffraction data, we have proposed a striped pattern magnetic structure, as well as a non-colinear magnetic structure for $KCuMnS_2$, with alternating layers oriented antiferromagnetically with a T_N of 160.5 K. Both structures have their magnetic moment oriented along only the *ab*-plane and a moment that was refined to 0.92(2) μ_B/ Mn^{2+}. We have also shown that by substituting Li^+ for Cu^+, long range ordering of the magnetic moment is destroyed. A feature of the $KLiMnS_2$ NPD pattern could indicate some short range ordering, though it is not definitive as it could also be the result of inelastic scattering.

The magnetic susceptibility of $KCuMnS_2$ decreases with temperature, showing

only a small feature near 160 K, until developing a curie tail near 40 K. Single crystal and pressed pellet powder samples of $KCuMnS_2$ show primarily semiconducting behavior for resistivity/resistance measurements respectively, except around the T_N of 160.5 K. Immediately below 160 K, $KCuMnS_2$ shows metallic behavior until resuming semiconducting behavior when the moment saturates, indicating that long-range magnetic order aids in the conductivity of the sample. Band structure calculations show the Fermi-level at the edge of the valence band for both compounds would make them susceptible to hole-doping.

Chapter 4: The Magnetic an Electronic Properties of $KCuMnSe_2$ and $KLiMnSe_2$

The work presented in this chapter has not yet been published. Dr. Peter Zavalij performed the single crystal analysis for this work, Brandon Wilfong performed properties measurements and accompanying Curie-Weiss fits, density functional theory and band structure calculations, Austin Virtue carried out sample preparation and powder diffraction measurements.

4.1 Introduction

It is clear that the M component of the MX_4 tetrahedra plays a major role in determining the properties of the AM_2X_2 system. Even changing half of the composition of this site, such as substituting lithium in place of copper, can drastically change the electrical and magnetic properties the $KMMnS_2$ compounds. Studies have shown that changing the A component of these compounds between different alkali metals produces trends in the Curie and Néel temperature, based off of the difference in interlayer spacing of those given series. [39,47,48,50,138] This then leaves the X component of the MX_4 tetrahedra as a method of modifying the properties of these compounds. Though not as pronounced as altering the metal site between

copper and lithium, changing the X component between different chalcogenides has shown to alter the properties of these compounds.

The utilization of larger chalcogenides will result in the lengthening of the unit cell and weaken $M-M$ bonding in the M_2X_2 layer, while enhancing the $M-X$ bonding. For example, in the AMFeCh_2 system, compounds such as $KAgFeS_2$, and $KCuFeS_2$ exhibit spin glass behavior while $KAgFeSe_2$, $KAgFeTe_2$ and $KCuFeTe_2$ have long range antiferromagnetic ordering. [50,92,139–143] The transition temperature at which this takes place also decreases along with the unit cell going from telluride to selenide to sulfide. The suppression of long range ordering with compression of the ab plane is attributed to the broadening of the Fe-3d band near the Fermi surface determined by the Fe-Ch overlap. To help understand if this overlap affect extends to the manganese containing compounds, the selenide versions of the sulfides prepared previously from chapter 3 can be prepared to compare the effect of the Mn-Ch overlap for the two systems.

From Greenblatt, $KCuMnSe_2$ was determined to be semiconducting and exhibit short-range antiferromagnetism. [48] The difference in the properties of the sulfides compared to their previously reported results may indicate that a different washing procedure for the selenides will also lead to a change in properties. The change in Ch to selenium is also expected to increase the size of the ab plane which could promote antiferromagnetism over spin glassiness in the AMMnCh_2 system as it does in the AMFeCh_2 system. In this chapter we show that while $KCuMnS_2$ already displays antiferromagnetic order, the Néel temperature is increased by the change in X atom to around 170 K. $KLiMnS_2$ displays no long range ordering,

and the increase in the *ab* plane for $KLiMnSe_2$ does not promote any long rang ordering antiferromagnetism. Calculations also predict that the valence band of these compounds has a strong *Ch* presence, so changing this from sulfur to the less electronegative, larger selenium, should have a noticeable difference on the conduction of these materials. Indeed, while we find that $KLiMnSe_2$ is an insulator, while $KCuMnSe_2$ is a semiconductor below 150 K and does not show the peak in resistance associated with the magnetic onset seen with $KCuMnS_2$.

4.2 Synthesis and experimental details

4.2.1 Sample preparation

The quaternary selenides were prepared through a modified procedure from Oledzka *et al.*. [48] By heating a mixture of pure metals with alkali metal carbonates under a flow of the reducing gas of 5 % hydrogen in nitrogen. Depending on the desired product, stoichiometric amounts of Mn metal (99.95% -325 mesh, Alfa Aesar) were mixed with either Cu metal (99.5% -200 +325 mesh, CERAC inc.) or a 5% excess of lithium carbonate (98%, Honeywell) to account for some Li evaporation, along with a 10% excess of potassium carbonate (99% anhydrous, Alfa Aesar), and a 10% excess of selenium pure metal (9.59% Aldrich). Powders were ground together in an agate mortar and pestle as an acetone slurry to a homogeneous mixture and allowed to dry. A typical synthesis of 12.5 mmol would consist of 0.9502 g K_2CO_3, 0.4849 g Li_2CO_3, 0.7943 g Cu, 0.6867 g Mn, and approximately 2.1717 g of selenium metal.

The mixture was loaded as a powder into an alumina crucible which was then placed into a tube furnace under a flow of 5 % hydrogen in nitrogen. The mixed gas flow pathway was set up to flow through a tube furnace, exiting the tube furnace through a bleach solution. The furnace was then heated at a rate of 180 °C per hour up to 900 °C. Once the temperature was reached, it was held at this temperature for 24 h, before the sample was cooled to room temperature at 180 °C per hour.

CAUTION: to impede the evolution of toxic H_2Se, the end of the gas stream was bubbled through a bleach solution (concentrated Clorox germicidal bleach, active ingredient: 8.25% sodium hypochlorite). The entire apparatus was contained in a fume hood.

The powders recovered contained impurities of potassium polyselenide. This polyselenide impurity could either be washed away with small amounts of water followed by methanol, or used as the flux for single crystal growth of the compounds, described below.

Single crystal growth was achieved by placing roughly 0.25 g of the unwashed powder into an evacuated quartz ampule, which was then placed in a second evacuated quartz ampule, heated at a rate of 50 °C per hour to 1000 °C. This temperature was held for 10 hours before cooling at a rate of 6 °C per hour to 500 °C. The ampule was then cooled at a rate of 30 °C per hour to room temperature. Single crystals were then recovered manually.

4.2.2 Diffraction, Magnetization, Resistivity, and DFT

Neutron powder measurements for $KCuMnSe_2$ and $KLiMnSe_2$ were performed on the HB-2A diffractometer at the Oak Ridge National Laboratory, High Flux Isotope Reactor (HFIR), with wavelength $\lambda = 2.4103$ Å (Ge 113 monochromator). Temperature dependent powder diffraction patterns were taken starting from a base temperature of 3.5 K. Rietveld refinements of the neutron diffraction data was carried out using the TOPAS 5.0 software. [75]

X-ray data was collected on a $KCuMnSe_2$ single crystal of approximate dimensions 0.35 mm × 0.30 mm × 0.05 mm in size with Mo Kα radiation of $\lambda = 0.71073$ Å. The crystal was measured every 20 degrees from 110 K to 250 K using the Bruker Smart Apex-II CCD system to uncover any possible crystallographic phase transitions coinciding with the onset of long-range magnetic order. The structure was solved and refined with the SHELX Software Package. [73]

Electrical transport measurements were preformed using a 9 T Quantum Design Physical Property Measurement System (PPMS-9) with polycrystalline samples of $KCuMnSe_2$ and $KLiMnSe_2$. Polycrystalline samples were ground into a powder and pressed into pellets utilizing < 2 ton uniaxial load without sintering. Electrical resistivity was measured using the four-probe method with gold wire and contacts made with silver paste. The temperature and field dependence of longitudinal electrical resistivity was measured in a range from 300 K to 1.8 K with applied current of 0.1 mA and frequencies near 17 Hz.

Temperature dependent DC (direct current) magnetic susceptibility measure-

ments were carried out using a Quantum Design Magnetic Property Measurement System (MPMS) on powder samples of $KCuMnSe_2$ and $KLiMnS_2$. Field-cooled (FC) and zero field-cooled (ZFC) measurements were taken from 1.8 K to 300 K with an applied magnetic field of 500 Oe. Magnetization versus field loops were carried out using the MPMS from -7 T to 7 T on the powder samples at 2 K and 50 K.

4.3 Results and discussion

4.3.1 Crystal Structure

The result of single crystal XRD measurements of $KCuMnSe_2$ are shown in Table 4.1 which shows that the sample crystallizes in a body-centered tetragonal crystal system. The lattice constants are $a = 4.0752(9)$ Å and $c = 13.821(3)$ Å at 110 K in space group $I4/mmm$ (No. 139). This is an increase of a of 0.131 Å and an increase of c of 0.582 Å with respect to $KCuMnS_2$, which is expected as the result of the larger chalcogenide.

The structural parameters for this single crystal are presented in Table 4.2, with all occupancies refined to unity. The Cu and Mn atoms share half of the $4d$ Wyckoff position, which has a site symmetry of $-4m2$. No superlattice reflections that would imply any ordering of the Mn and Cu atoms on the $4d$ site were observed. The crystal was found to retain tetragonal symmetry at all temperatures measured.

The structure obtained from the single crystal X-ray results (Tables 4.1 and 4.2) was used to model and fit the neutron powder diffraction (NPD) data. The NPD taken at 200 K is shown in Figure 4.1. Refinement of the model showed primarily

$KCuMnSe_2$, with small amounts of impurities of manganosite (MnO, 0.38 weight %) and copper (0.82 weight %). Even modeling these impurities the refinement of the model only provides an R_{wp} = 13.760 %. The main reasons for this are the poor fittings of the (011) peak at a Q of 1.6 $Å^{-1}$, the (013) peak at 2.05 $Å^{-1}$, the (213) peak at 3.7 $Å^{-1}$, and the (211) peak at 3.46 $Å^{-1}$. While the poor fitting of the peaks with additional measured intensity could be due from an additional

Table 4.1: Single-crystal X-ray diffraction data for $KCuMnSe_2$.

Space Group	$I4/mmm$ (no.139)
a (Å)	4.0752(9)
c (Å)	13.821(3)
Crystal system	Tetragonal
Volume ($Å^3$)	229.53(11)
Z	2
Calculated density (g cm^{-3})	4.565
λ, Mo Kα Å	0.71073
No. of reflections collected	1681
No. of independent reflections	141
$F(000)$	282.0
R_1, wR_2 (%)	1.59, 3.54
Temperature	110 K

Table 4.2: Structural, lattice, and anisotropic displacement parameters for $I4/mmm$ $KCuMnSe_2$ from single crystal data at 110 K. All off-diagonal terms are equal to zero.

Atom	Wyckoff Site	x	y	z	$U_{11}(Å^2) = U_{22}(Å^2)$	$U_{33}(Å^2)$
K	2a	0	0	0.5	0.0110(5)	0.0181(8)
Cu/Mn	4d	0.5	0	0.25	0.0078(2)	0.0164(4)
Se	4e	0.5	0.5	0.35942(4)	0.0074(2)	0.0136(3)

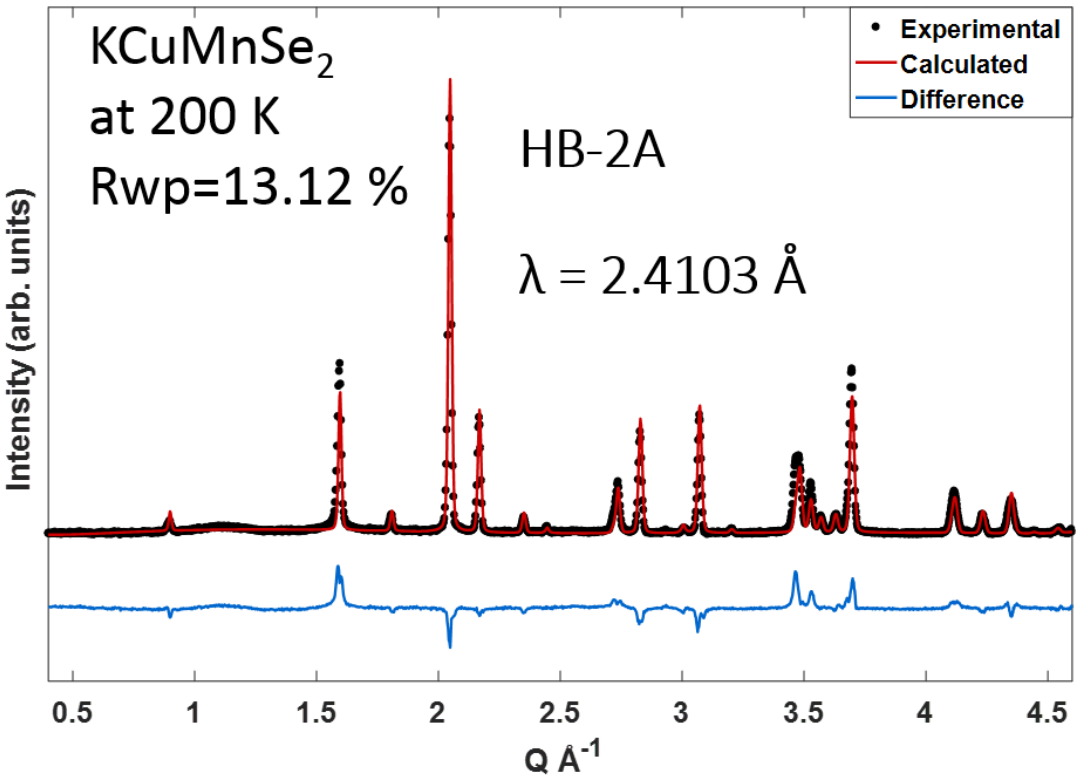

Figure 4.1: Neutron powder diffraction of $KCuMnSe_2$ with less than 1% manganosite and copper impurities.

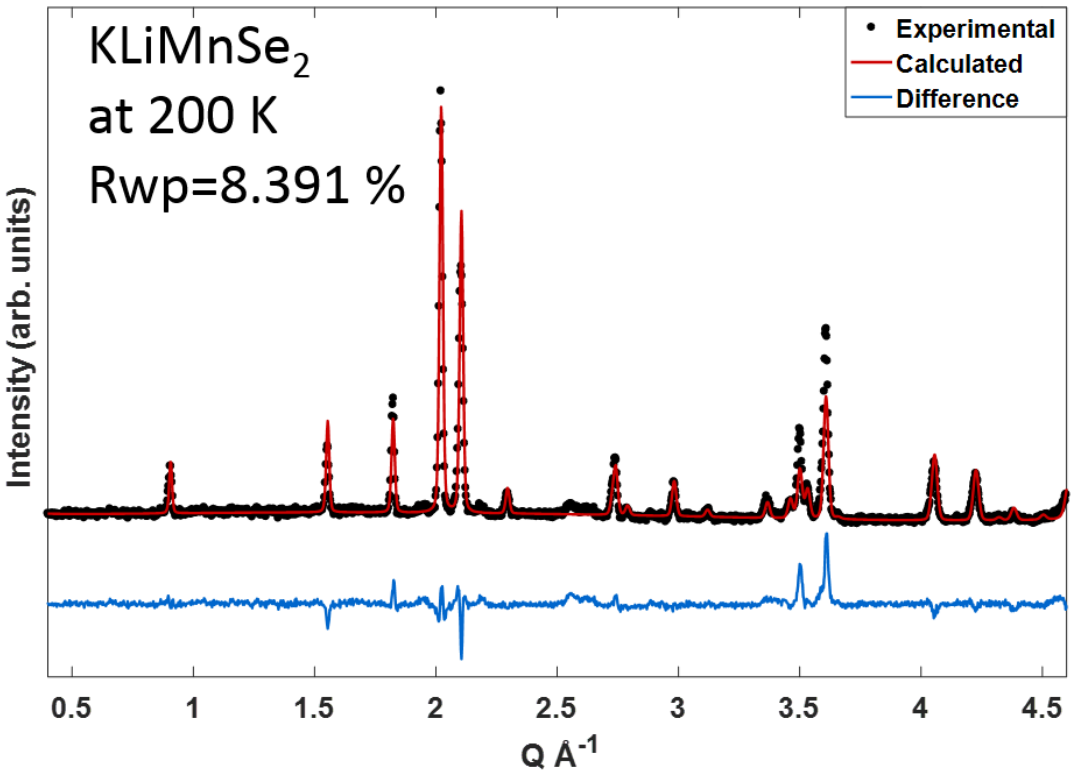

Figure 4.2: Neutron powder diffraction of $KLiMnSe_2$

impurity, all of these peaks share a k value of 1, possessing some K occupancy. There is also a broad hump around 1.25 $Å^{-1}$, which could be due to remaining potassium polyselenide impurity. While this indicates that further refinement is necessary to refine a models to adequately fit the NPD, this model can still be used as a comparison to the NPD at lower temperatures, discussed later with regard to magnetic structure.

While no single crystal XRD was performed on $KLiMnSe_2$, PXRD refinement provided an adequate model to refine using the NPD obtained. NPD for $KLiMnSe_2$, again using isotopically pure ^{7}Li, At 200 K, the structure model refines to an R_{wp} = 9.502 % without any impurity phases. $KLiMnSe_2$ retains the tetragonal 122-

structure but the a parameter lengthens to 4.2041(3) Å from 4.0822(2) Å, while the c parameter contracts to 13.715(1) Å from 13.827(1) Å compared to the NPD data for $KCuMnSe_2$ at the same temperature. Refinement of the occupancy of the Mn and Li sites indicated a not insignificant loss at that site, with occupancies of Mn = 45.92 % and Li = 43.14 %. Likely, the loss of lithium to evaporation had some effect on this, though how much of an effect that had on the refinement of the Mn still needs to be seen. As with $KCuMnSe_2$, while further refinement is always possible for a Rietveld refinement, this model can still be used for comparison with the low temperature NPD.

4.3.2 Temperature dependence

First we discuss the temperature dependence of the NPD pattern for $KCuMnSe_2$ between 3.5 K and 200 K. Cooling the sample down to base temperature causes the emergence of additional peaks that can be attributed to a magnetic structure. The NPD pattern at 3.5 K can be seen in Figure 4.3 and clearly shows additional peaks specifically focusing around 1.15 $Å^{-1}$. While the refinement for this pattern is shown, no R_{wp} is presented as at the time of this work, we do not yet have a model to fit the magnetic structure associated with these peaks. Not only does this prevent us from obtaining any meaningful R_{wp} value, it hinders accurate refinement of all other parameters due to the fact that the refinement is still trying to model the magnetic peaks using only the structural parameters. This does not prevent us from directly comparing the patterns to determine the temperature dependence.

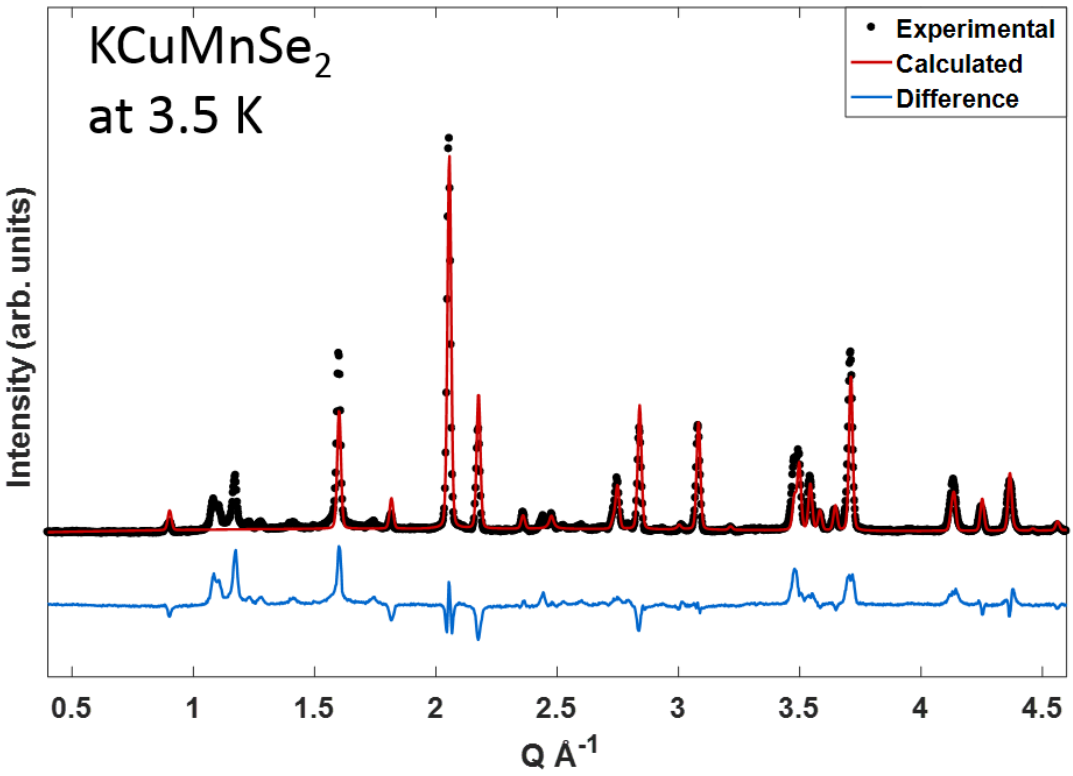

Figure 4.3: Neutron powder diffraction of $KCuMnSe_2$

Full powder patterns were taken at a base of 3.5 K, as well as 10, 30, 50, 100, 160, and 200 K. Comparing these scans around 1.15 $Å^{-1}$, shown in Figure 4.4, shows a clear temperature dependence for no fewer than five different peaks.

After the full powder pattern scans were completed, the sample, at 3.5 K, was then slowly heated while one of the detectors was held a position of 26.05 degrees 2θ, or 1.175 $Å^{-1}$. Intensity measurements were taken every two minutes with an initial temperature interval of five degrees, though this temperature interval shortened above 160 K. The inset for Figure 4.4 shows the temperature dependence of the peak at 1.175 $Å^{-1}$. While there is some interference with the broad hump that may be due to potassium polyselenide, this peak appears to have an onset slightly above

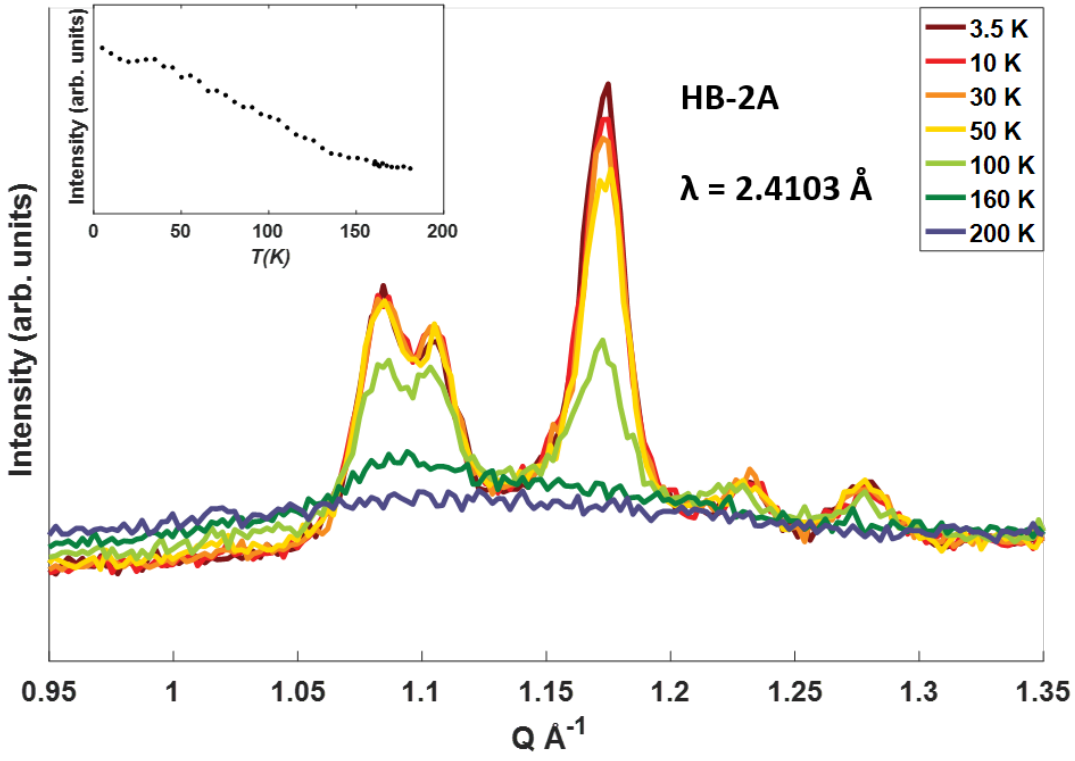

Figure 4.4: Enhanced view of the magnetic peaks of $KCuMnSe_2$ around 1.15 $Å^{-1}$ with the temperature dependence of the peak at 1.175 $Å^{-1}$.

160 K. This also would fit with the temperature dependent peaks at 1.1 $Å^{-1}$ shown in Figure 4.4, where both peaks are clear at 100 K, become difficult to see at 160 K, and are gone at 200 K. Both peaks at higher Q appear to be gone by 160 K, but this could be due to their originally weak intensity.

The NPD powder pattern for $KLiMnSe_2$ at the base temperature of 3.5 K can be seen in Figure 4.5. Using the same occupancy parameters for the refinement at 200 K, the refinement at 3.5 K possesses an R_{wp} of 8.319. This improved R_{wp} while still only modeling $KLiMnSe_2$ indicates that there is very little temperature dependence for $KLiMnSe_2$. Similar to $KLiMnS_2$, there is a broad hump that appears

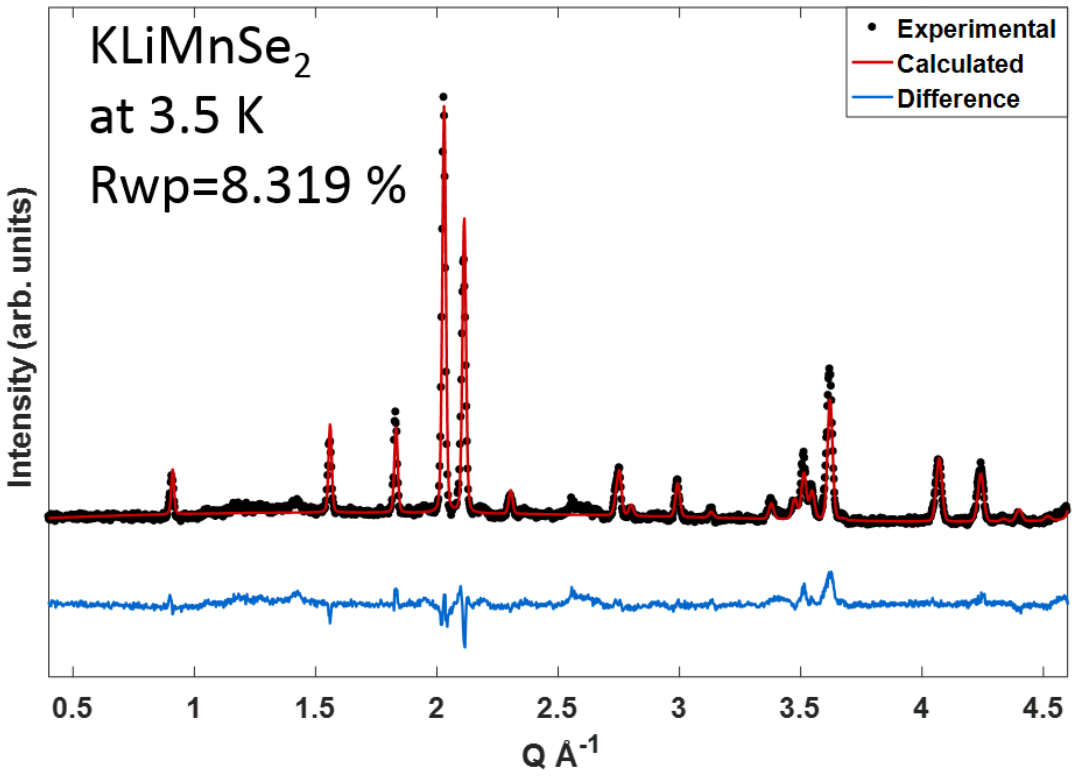

Figure 4.5: Neutron powder diffraction of $KLiMnSe_2$

centered around 1.25 $Å^{-1}$ that could indicate some short-range ordering with a lack of long-range ordering of the magnetic moments, or it could arise from inelastic scattering. Even with the improved R_{wp}, there is still one additional temperature dependent peak at around 1.4 $Å^{-1}$ in Figure 4.6, though the onset temperature for this is significantly lower than those for $KCuMnSe_2$. Full powder patterns were taken at 3.5, 20, 50, 75, 100, and 200 K, and a comparison between the 3.5 K and 20 K patterns in Figure 4.6 shows that the weak temperature dependent peak had vanished by 20 K.

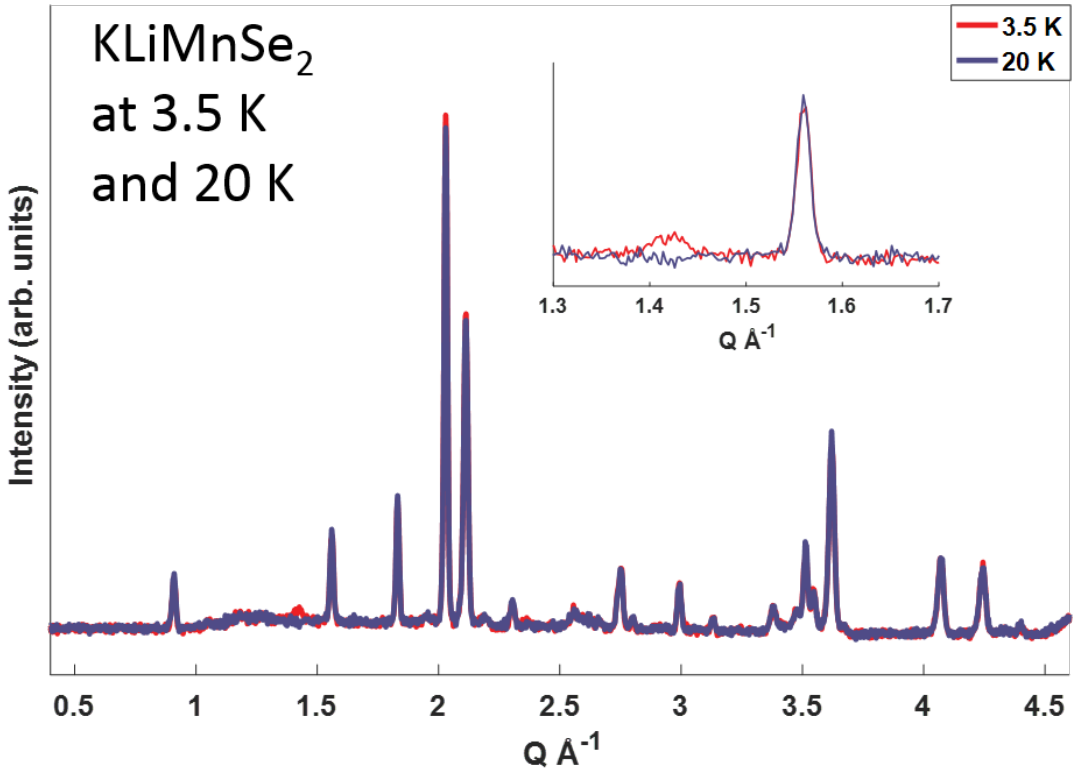

Figure 4.6: Neutron powder diffraction of $KLiMnSe_2$

4.3.3 Magnetism and Magnetic Structure

Magnetic susceptibility measurements were taken for $KCuMnSe_2$ and $KLiMnSe_2$, and can seen in Figure 4.7. Interestingly, there were no significant features above 60 K for $KCuMnSe_2$. Susceptibility steadily rises with decreasing temperature until the ZFC and FC curves for both compounds diverge (roughly 50 K for $KCuMnSe_2$ and 40 K for $KLiMnSe_2$). At this temperature, there is a sharp increase in susceptibility in both curves, however the ZFC curves then have a similar cusp to what was seen for $KLiMnS_2$ (At 38 K for $KCuMnSe_2$ and 33 K for $KLiMnSe_2$). This could be the result of spin-glass behavior that is enhanced through the extended $M - M$ bond distances when using the larger Ch. As with the sulfides, we are

expecting the magnetic properties of these compounds to be solely from the Mn^{2+} ($3d^5$) ions as copper is in the diamagnetic $3d^{10}$ configuration and lithium would have a happy helium configuration. Given the Mn^{2+} occupancy of the site to be only 50 %, this increased $M - M$ distance would work against any long range ordering of any manganese clusters brought about from the general site disorder. The Curie-Weiss fits for these compounds both predict antiferromagnetic order, at 163 K for $KCuMnSe_2$ and 45 K for $KLiMnSe_2$. Interestingly, the calculated magnetic moment for $KCuMnSe_2$ as seen in Figure 4.8, while larger than that of $KCuMnS_2$ at 2.365 μ_B/ Mn^{2+} is significantly less than that calculated for $KLiMnSe_2$ in Figure 4.9 at 4.529 μ_B/ Mn^{2+}. Neither of these yet reach the 5.9 μ_B predicted for the spin only moment of high-spin Mn^{2+}. These calculated moments are much closer to two (2.83 μ_B), and four (4.9 μ_B) unpaired electrons for $KCuMnSe_2$ and $KLiMnSe_2$ respectively. While this could be achieved for low-spin and high-spin Mn^{3+} respectively, the charge balancing needed would also add unpaired electrons to the system. While no impurities were seen for either sample with NPD or XPD, they can never be truly dismissed. Again, this increased moment for the lithium compound is a good indication that the magnetic characteristic of these compounds relies solely on the manganese.

4.3.4 Resistivity and Electronic Structure

The electrical resistance of both compounds was taken showing that $KLiMnSe_2$ is an insulator(Figure 4.10b), whereas $KCuMnSe_2$ has some semiconducting prop-

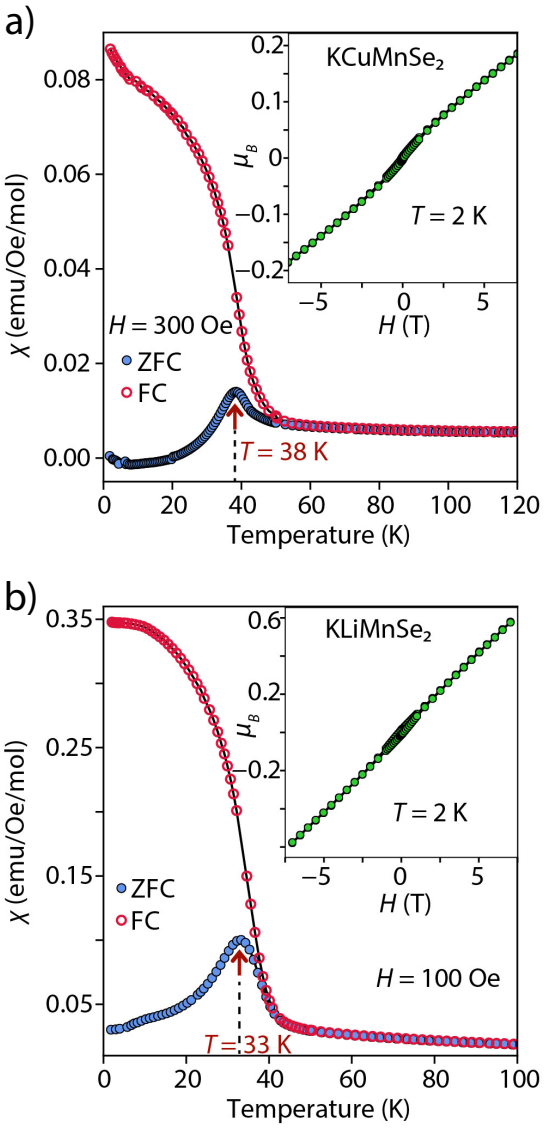

Figure 4.7: Temperature dependent magnetic susceptibility of a) $KCuMnSe_2$ and b) $KLiMnSe_2$.

erties (Figure 4.10a). $KCuMnSe_2$ behaves as a degenerate semiconductor between 150 and 290 K, with an increasing resistance with temperature similar to a metal. Below 150 K, $KCuMnSe_2$ behaves as a classic semiconductor. This is in contrast to what was seen by Oledzka, whose measurements show only thermally activated semiconductor type behavior. [48] The difference in resistivities is not surprising

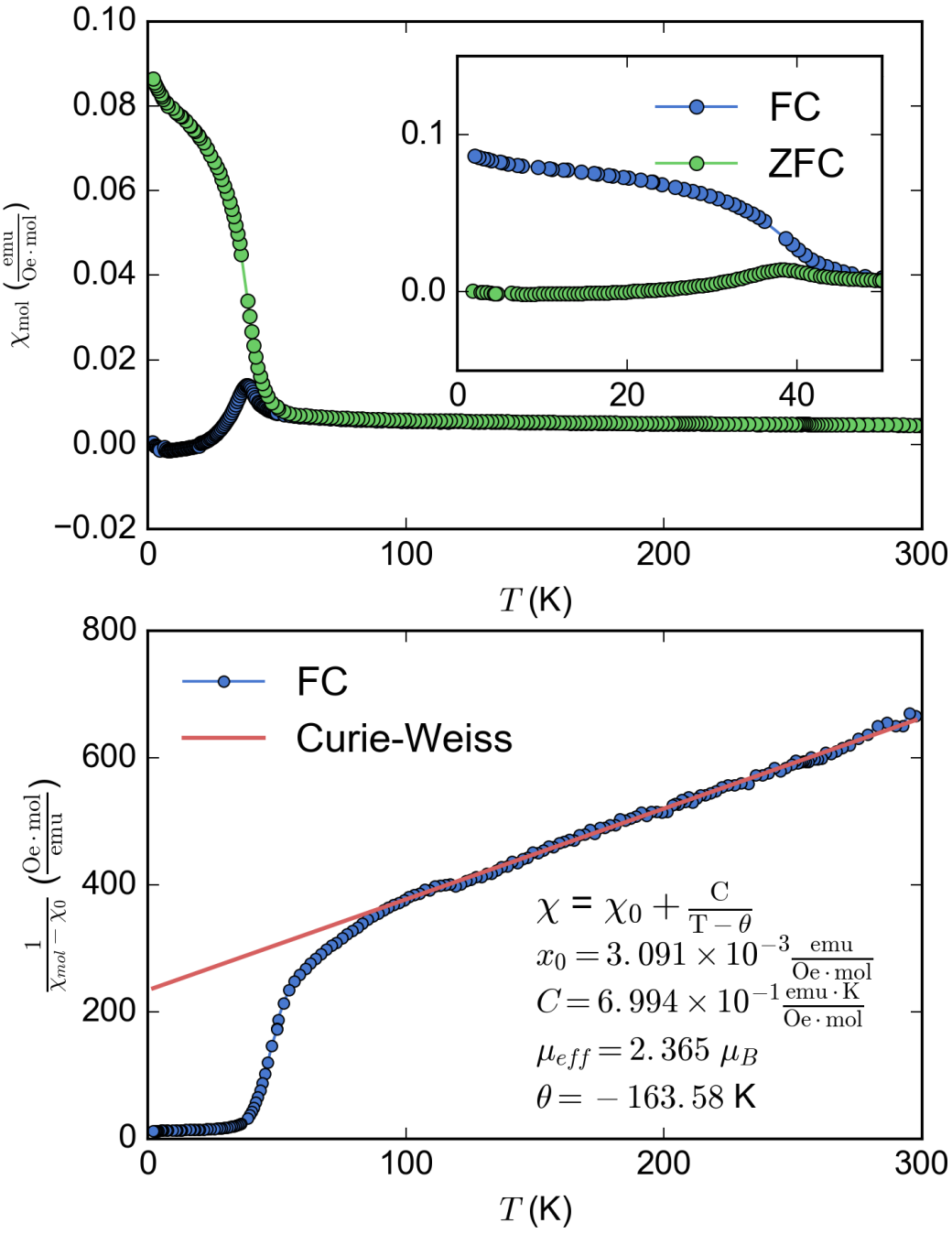

Figure 4.8: Extended magnetic susceptibility of $KCuMnSe_2$ (top) and the Curie-Weiss fit of $KCuMnSe_2$ (bottom) showing a calculated magnetic moment of 2.365 μ_B/ Mn^{2+} and a Weiss constant of -163.58 K.

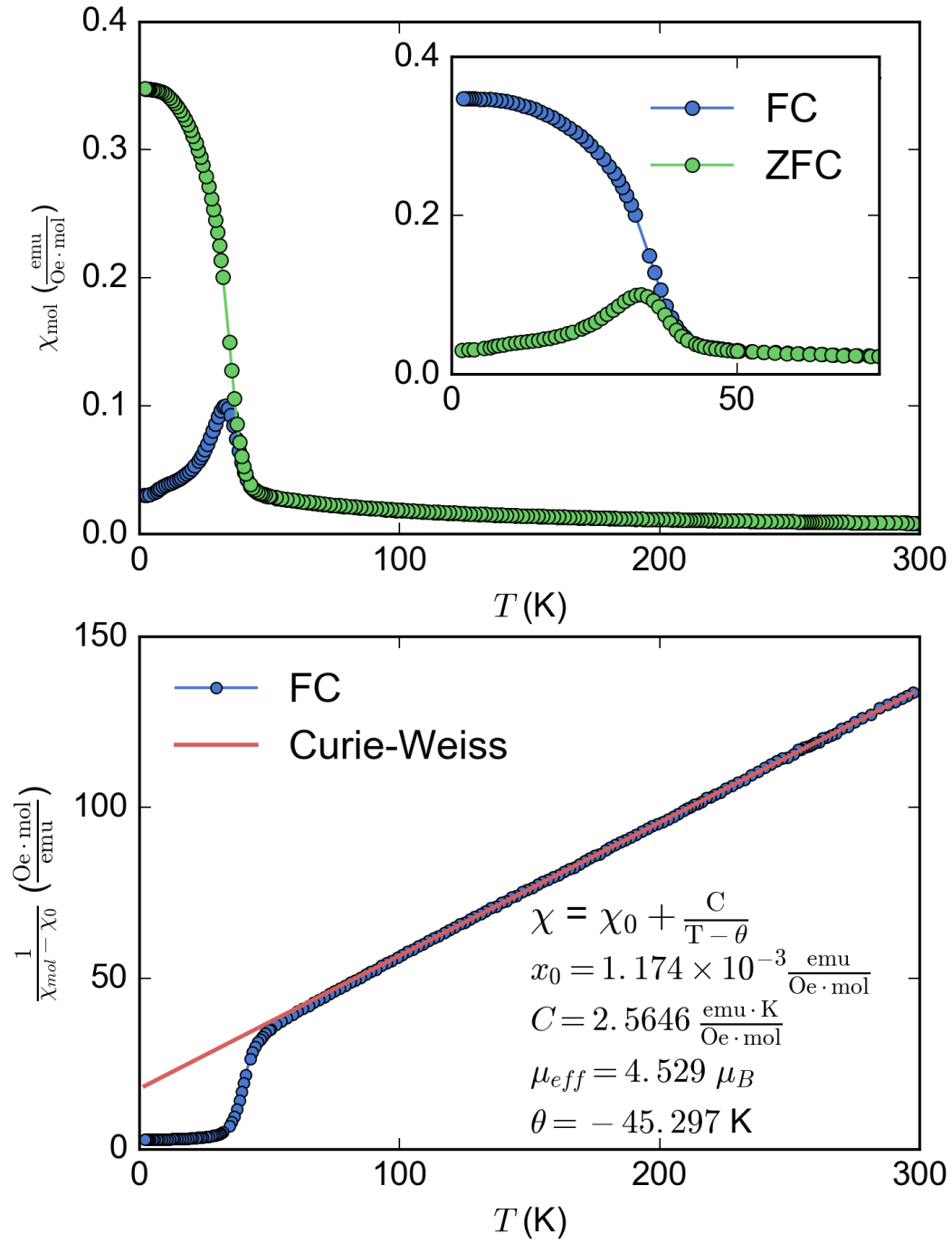

Figure 4.9: Extended magnetic susceptibility of $KLiMnSe_2$ (top) and the Curie-Weiss fit of $KLiMnSe_2$ (bottom) showing a calculated magnetic moment of 4.529 μ_B/ Mn^{2+} and a Weiss constant of -45.297 K.

when one takes into account the the dispersion curves for each compound. While the full curves and densities of states for both compounds in Figure 4.11 looks like both compounds are semiconductors, a more detailed look into the band structure in 4.13 shows predictably no lithium states near the Fermi level. While $KCuMnSe_2$ is predicted to be a hole carrier [48], such a mechanism would be very difficult for $KLiMnSe_2$ as it does not have the copper *d*-orbitals in the valence band that $KCuMnSe_2$ has as shown in Figure 4.12.

4.4 Conclusions

Samples of $KCuMnSe_2$ and $KLiMnSe_2$ have been prepared for neutron diffraction studies as well as magnetic and electrical properties measurements. Single crystals of $KCuMnSe_2$ were prepared for a more detailed characterization. $KCuMnSe_2$ also showed some long range ordering of its magnetic moments with an onset of around 170 K, though its magnetic structure is as yet unknown. In contrast to this $KLiMnSe_2$ shows no strong indication of long range ordering, other than a small peak in the NPD taken at 3.5 K that is gone by 20 K. Their electrical properties are also markedly different, as $KLiMnSe_2$ is an insulator, while $KCuMnSe_2$ behaves as a degenerate semiconductor above 150 K and behaves as a classical semiconductor below 150 K.

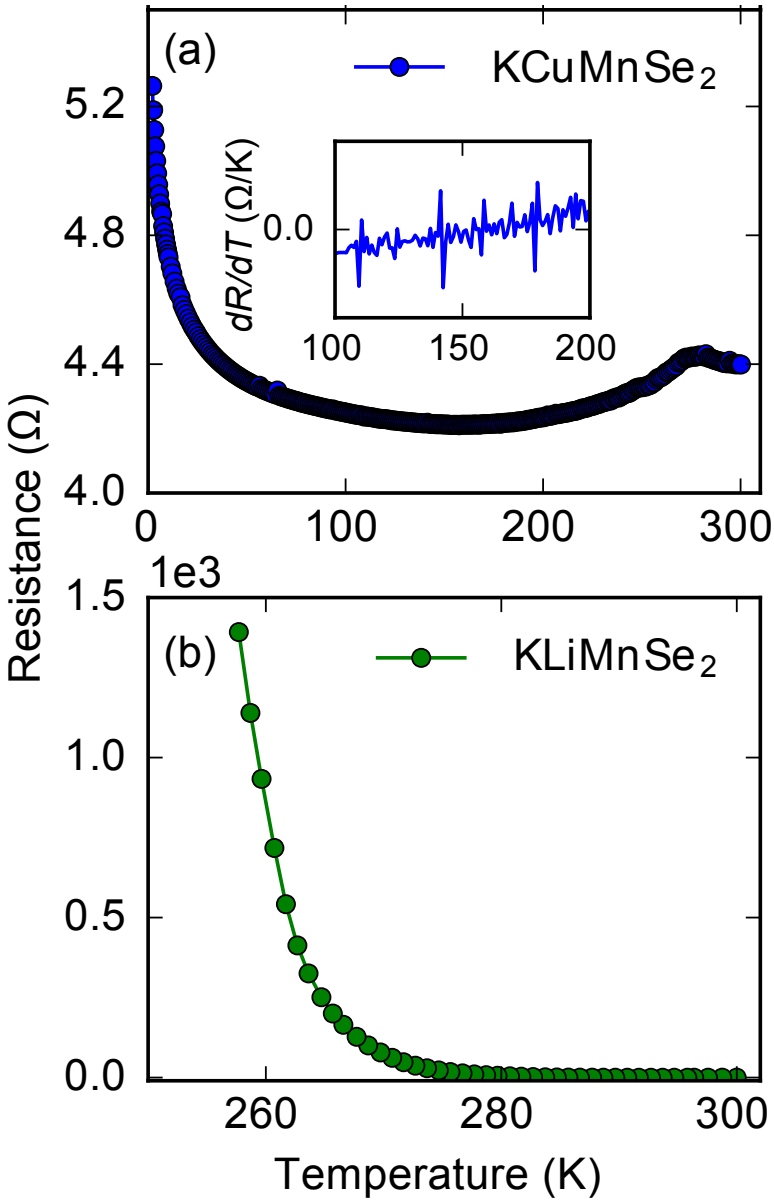

Figure 4.10: Resistance of $KCuMnSe_2$ (a), and $KLiMnSe_2$ (b).

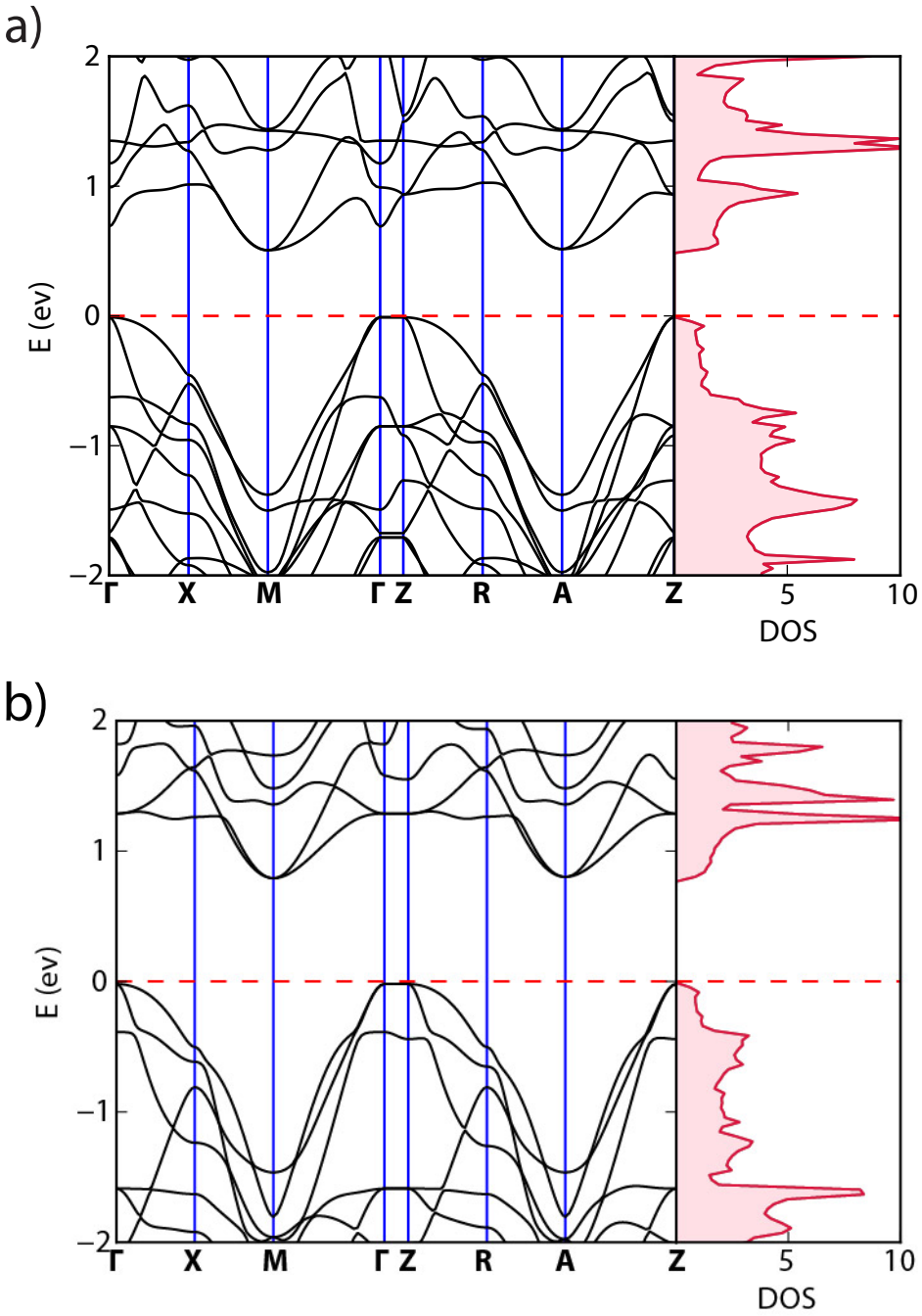

Figure 4.11: Dispersion curves and DOS of the electronic states near the Fermi-level for $KCuMnSe_2$ (a) and $KLiMnSe_2$ (b) showing the Fermi-level on the edge of the valence band.

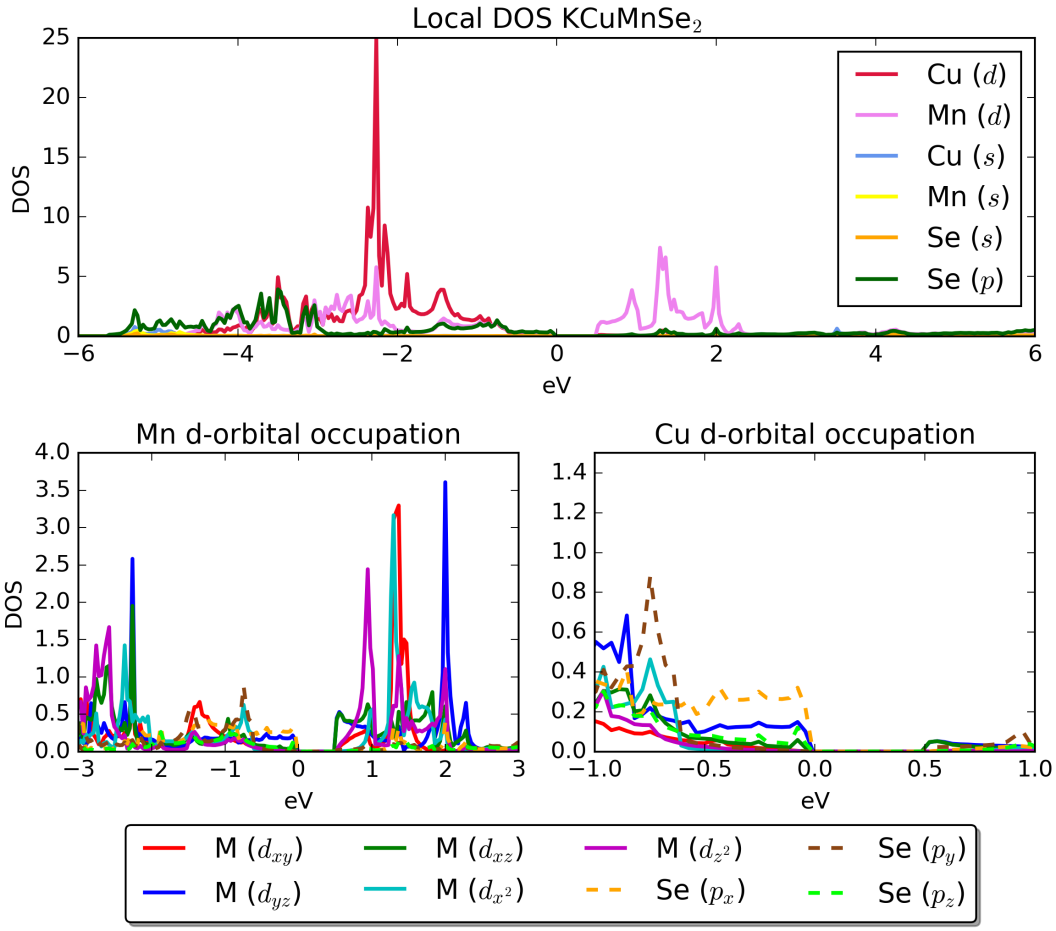

Figure 4.12: Local density of states for $KCuMnSe_2$.

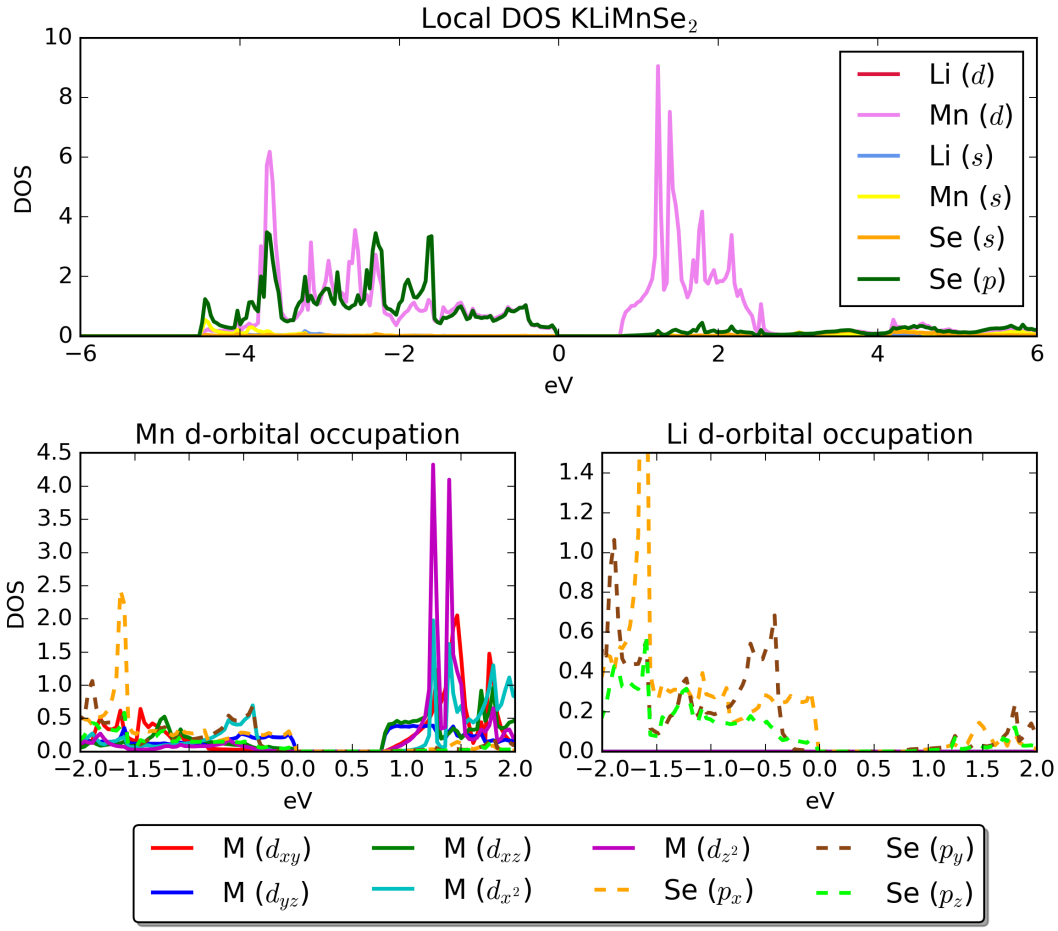

Figure 4.13: Local density of states for $KLiMnSe_2$.

Chapter 5: Additional 122 Type Compounds with the $ThCr_2Si_2$ structure

The work presented in this chapter has not yet been published. Brandon Wilfong performed properties measurements and accompanying Curie-Weiss fits, density functional theory and band structure calculations, Austin Virtue carried out sample preparation and powder diffraction measurements.

5.1 Introduction

It could be said that the spark that lit the fire for this work was the discovery of superconductivity in the iron containing 122-type compounds. [20,26–30] Striving to understand the properties of related manganese compounds to the degree that they could be modified to the point of mimicking their superconducting iron kin was one of the dreams of this work. The variety of structures with tetrahedral FeX_4 forming layers of Fe_2X_2, naturally leads to the investigation of all modifications to this structure type. This is particularly true of the electron or hole doping through site substitution that has been shown to promote superconductivity. [1,6–19,21,24,25,27,28,30] This site substitution is primarily achieved through either the A or M site, with the A site incorporating both an alkali metal, and alkaline earth metal,

or where the M site incorporates different transition metals, as in chapters 3 and 4.

The lack of a synthetic method capable of preparing KMn_2Ch_2 leads, not only to the required incorporation of copper, but also a difficulty in comparing the mixed metal compounds to the non-mixed metal iron based superconductors. As $KCuFeCh_2$ has been reported, a more direct comparison can be made between these mixed metal compounds to determine the characteristics of the manganese containing compounds versus their iron variants. As with the manganese versions of these compounds, there is no discernible ordering between the copper and iron. Unlike the manganese compounds however, these iron compounds display magnetic behavior similar to that of the lithium manganese compounds, with no long range ordering, and a distinct spin glass like behavior.

As for other modifications to the 122-type system in regards to the M compositions that we have previously discussed, solid solutions of these series and small amounts of doping would be the next step towards tuneability. Particularly, the $KCuMnCh_2$ and $KCuFeCh_2$ systems. As manganese and iron are both 2+ in these systems, a solid solution of $KCu[Mn_xFe_{1-x}Ch$ should be feasible. This chapter shows the work done on attempting to produce this solid solution, the difficulties in doing so, as well as the work done to determine the limits of the $KCuMCh_2$ systems acceptance of a metal site ration away from 1:1.

5.2 $KCuFeCh_2$ where Ch = S, Se

5.2.1 Sample preparation

The quaternary sulfide was prepared in a method similar to that in chapter 3 in a modified from another procedure from Oledzka *et al.*. [50] This is a single step process as an alternative to the methods that had been used to prepare these compounds prior to the work done by Oledzka. [139, 144] The quaternary selenide was prepared in a method similar to that in chapter 4. The key difference is that in place of manganese, iron metal powder (99.5% APS 6-10 micron, Alfa Aesar) was used. A typical synthesis of 12.5 mmol would consist of 0.9502 g K_2CO_3, 0.7943 g Cu, and 0.6981 g Fe was used. For the selenide, approximately 2.1717 g of selenium metal was added to this original mixture. For the sulfides, approximately 15 mL of CS_2 was used during the synthesis. As in the previous chapters to impede the evolution of either toxic H_2S or H_2Se, the end of the CS_2 stream was bubbled through a bleach solution. The entire apparatus was contained in a fume hood. Single crystal growth was also achieved through the previously described method of sealing in a double quartz ampule, and slow cooling from temperature.

5.2.2 Diffraction

Neutron powder measurements for $KCuFeS_2$ and $KCuFeSe_2$ were performed on the BT-1 diffractometer at the NIST Center for Neutron Research (NCNR) with wavelength $\lambda = 2.079$ Å (Ge 311 monochromator) at a base temperature of 6 K and

an elevated temperature of 70 K.

5.2.3 Crystal Structure

The lattice constants for $KCuFeS_2$ refined from neutron diffraction in Figure 5.1 at 70 K are $a = 3.8455(1)$ Å and $c = 13.0976(6)$ Å in space group $I4/mmm$ (No. 139). The lattice constants for $KCuFeSe_2$ refined from neutron diffraction in Figure 5.2 at 70 K show the expected increase due to the larger chalcogenide, and are $a = 3.9690(1)$ Å and $c = 13.711(1)$ Å in space group $I4/mmm$ (No. 139) . The fit obtained from the $KCuFeSe_2$ pattern also needed to be fit with small amounts of iron (3.72 %) and berzelianite (Cu_2Se, 3.54 %).

5.2.4 Temperature dependence

Unlike the previous manganese containing compounds, neither $KCuFeS_2$ or $KCuFeSe_2$ showed any drastic difference to their neutron powder patterns at base temperature. Figure 5.3 shows the fit for the neutron powder data of $KCuFeS_2$ at 6.5 K. Using only the structural model, a similar fit is able to be obtained compared to the elevated temperature model ($R_{WP} = 9.713$ at 6.5 K vs $R_{WP} = 9.430$ at 70 K). To emphasize this, the difference between the two patterns is shown in Figure 5.4, with its difference curve showing only typical lattice contraction at lower temperature which refines the model parameters to $a = 3.8411(1)$ Å and $c = 13.0800(6)$ Å.

For the most part, $KCuFeSe_2$ follows the same trend, with similar fits at both temperatures ($R_{WP} = 10.605$ at 6.5 K vs $R_{WP} = 10.501$ at 70 K) also fitting small

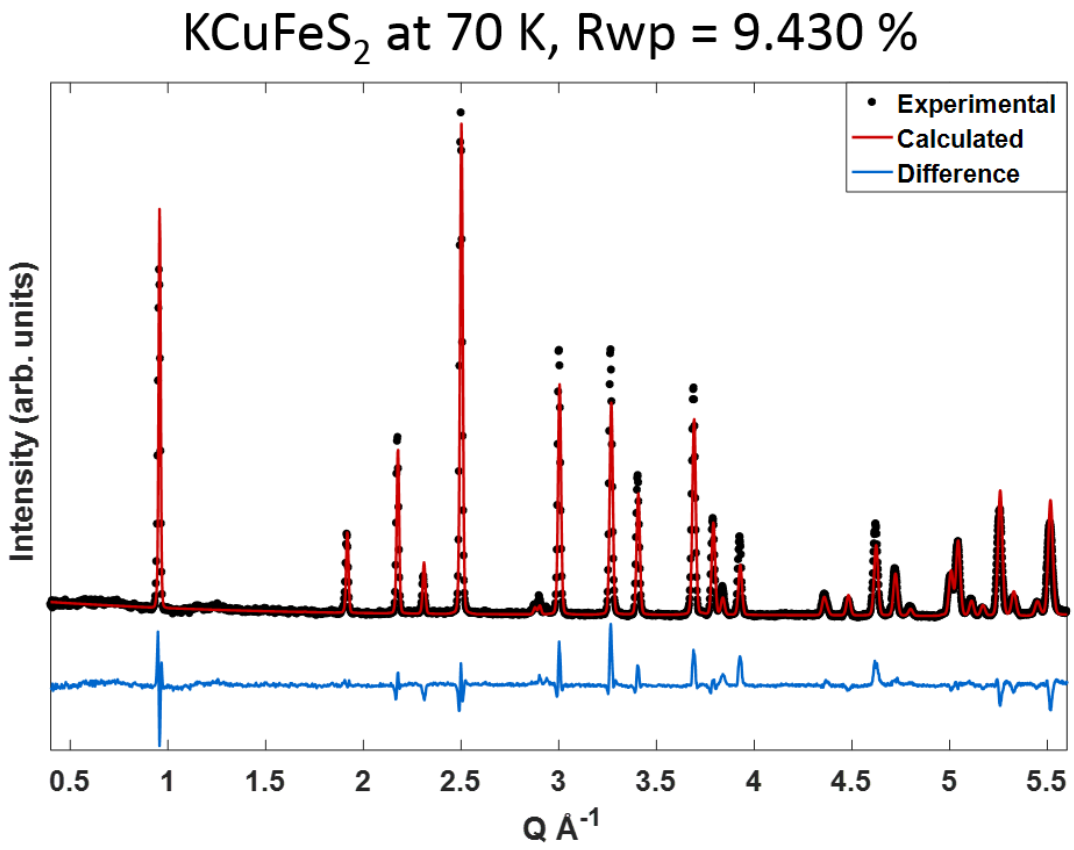

Figure 5.1: Neutron powder diffraction of $KCuFeS_2$ at 70 K

amounts of iron and berzelianite. The only differences of note are the slight increase in intensities most notable on the (002) peak at 0.96 $Å^{-1}$ and the (020) peak at 3.16 $Å^{-1}$.

5.2.5 Magnetization, and Electronic Structure

The temperature dependent magnetic susceptibility curve for $KCuFeSe_2$ under fields of 30 Oe, 300 Oe, and 1 T is shown in Figure 5.7. While there appears to be a transition at around 40 K, this temperature decreases and the divergence of the ZFC and FC curves becomes less pronounced at higher field. This is an indication

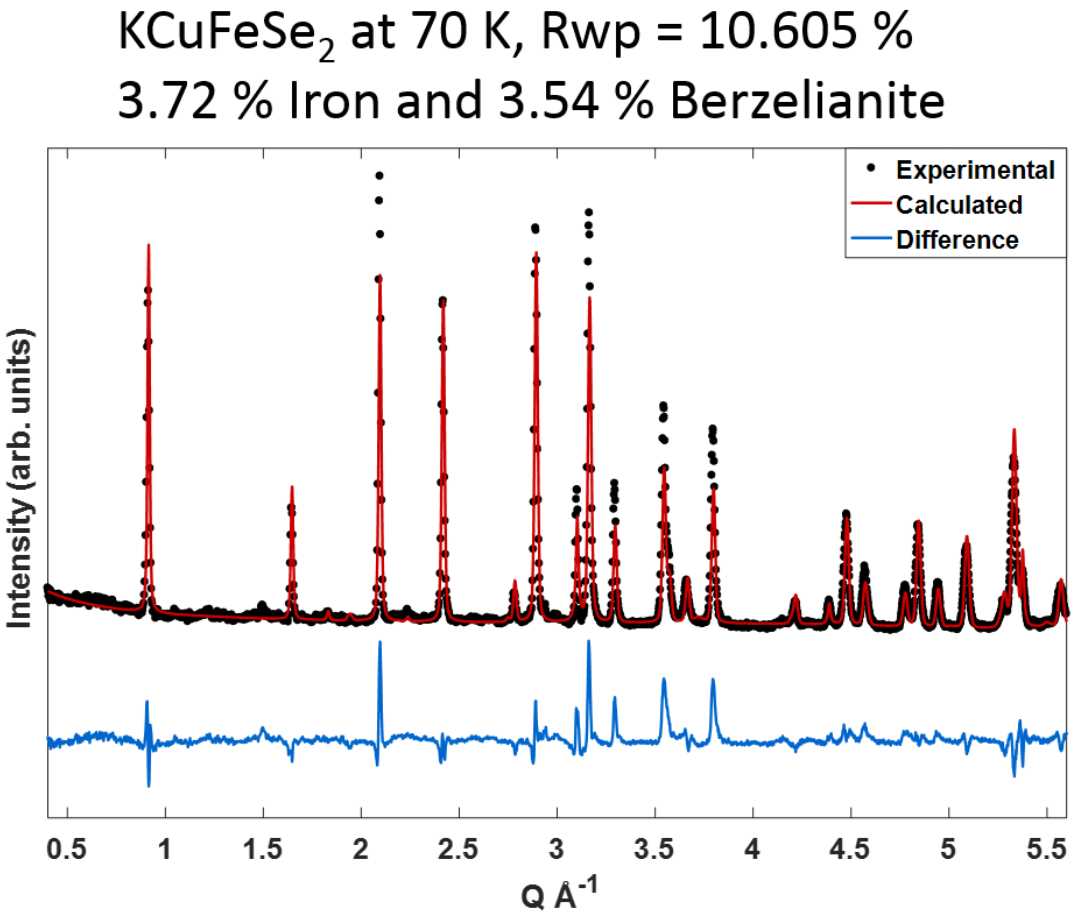

Figure 5.2: Neutron powder diffraction of $KCuFeSe_2$ at 70 K

that the transition is associated with a spin-glass transition. The Curie-Weiss fit for $KCuFeSe_2$ can be seen in Figure 5.8, and shows the largest of the predicted moments for the compounds discussed in this work at 5.484 μ_B/ Fe^{2+}. Though this is larger than the 4.9 μ_B predicted from the spin only magnetic moment of Fe^{2+}, it is less than the theoretical maximum with positive orbital contributions. It should be noted that the NPD data for this sample also revealed a small amount of iron impurity that could cause an additional moment to this fit. Though the Curie-Weiss fit also indicates an antiferromagnetic transition at 19 K, there is no indication of

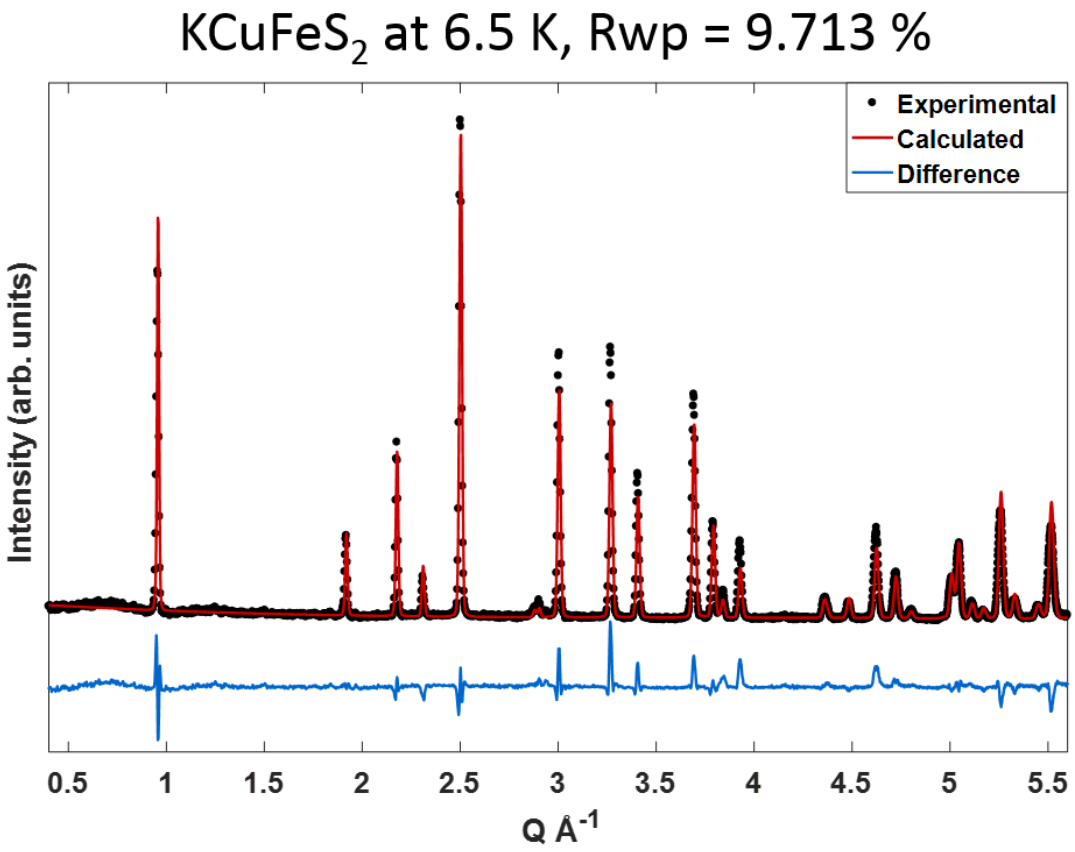

Figure 5.3: Neutron powder diffraction of $KCuFeS_2$ at 6.5 K

long range ordering of this large magnetic moment from neutron diffraction.

The density of states calculations for both of these compounds predicts them to be metallic (Figure 5.9. This is a marked difference between the other compounds from chapters 3 and 4. Not unsurprisingly, when looking into the reason as to the cause of this change, it comes in the form of the only change made to the compounds from those in chapters 3 and 4. The local density of states for both compounds (Figures 5.10 and 5.11) shows primarily Fe orbital density at the Fermi level.

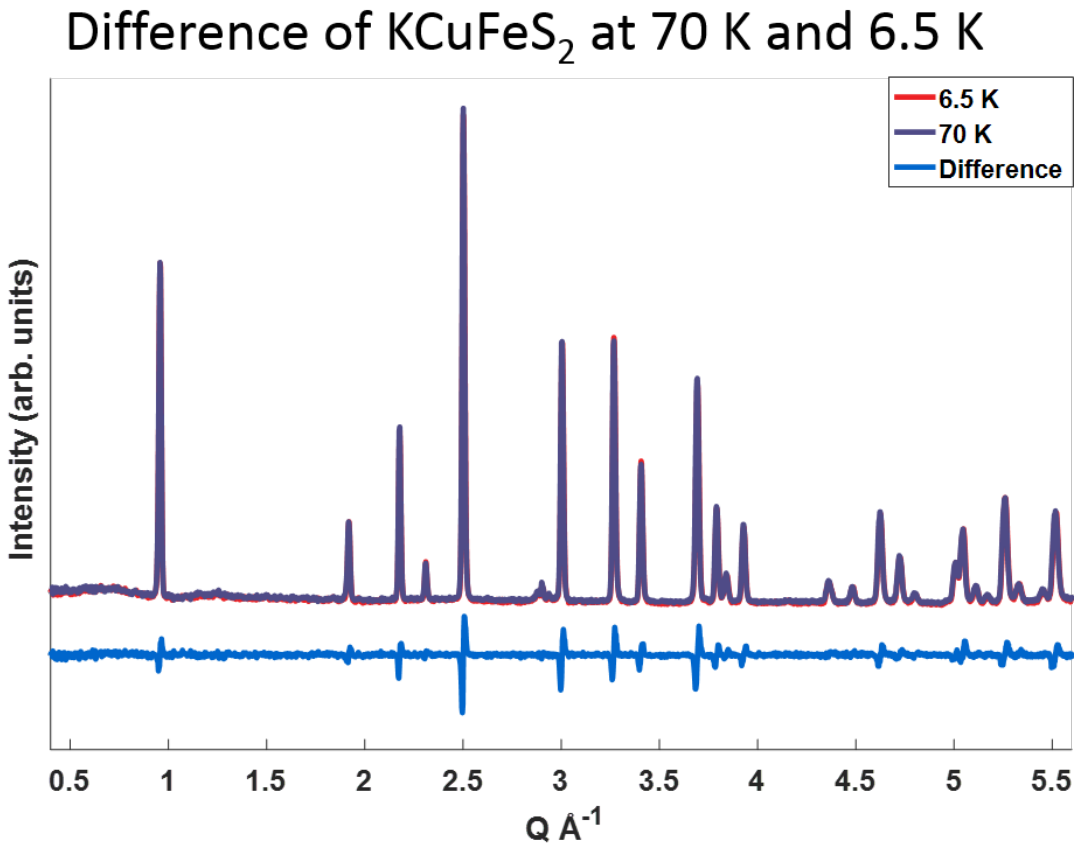

Figure 5.4: The difference in neutron powder diffraction of $KCuFeS_2$ at 70 and 6.5 K

5.3 $KCu_{1-x}M_xS_2$ (Where M = 2+ Cation, some combination of Mn^{2+}, and Fe^{2+})

5.3.1 Synthesis and experimental details

These quaternary sulfides were prepared in a method similar to that in chapter 3, with the composition of metals used in the synthesis matched to the desired content in the sample.

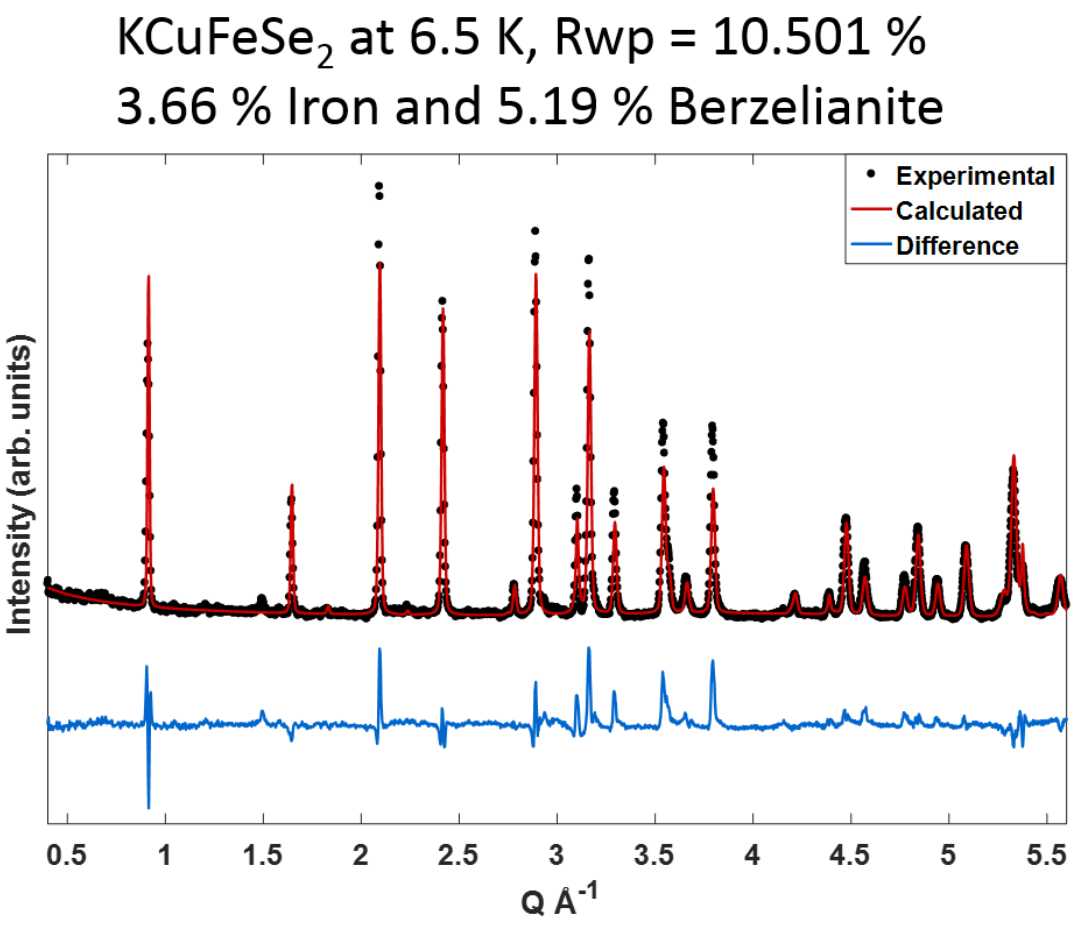

Figure 5.5: Neutron powder diffraction of $KCuFeSe_2$ at 6.5 K

5.3.2 Results

While previous chapters may have made it seem like the synthesis of these materials is trivial, and to be fair, the procedure itself is pretty straight forward, the proposed tuneability of these materials is not as simple as one would hope. While in theory, the site occupancy of these materials should be dictated by their constituents, making them work together is another matter. When keeping the A cation the same, in this work it has been potassium all along which only occupies the A site, and keeping the X anion main group element as a chalcogenide that only

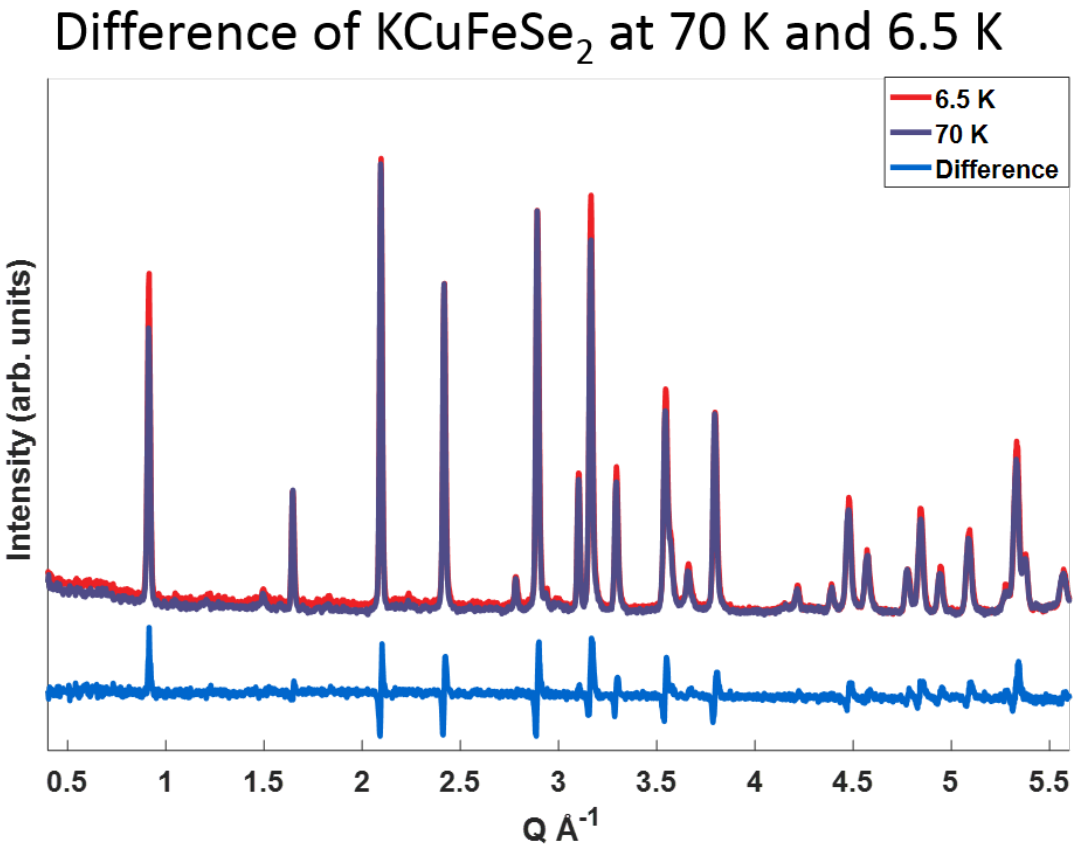

Figure 5.6: The difference in neutron powder diffraction of $KCuFeSe_2$ at 70 and 6.5 K

occupies the X site, that therefor leaves only the M site for the added transition metals to occupy. In theory, as long as they average out to a 1.5+ oxidation state, the MX_4 tetrahedral layers should be able to nicely ionically bond to the A cation layers.

As this section demonstrates however, this is not easily the case. This work has already presented $KCuMnS_2$, and $KCuFeS_2$. Both compounds have Cu^{1+} with the other metal being 2+. It is therefor reasonable to assume that in a $KCuMS_2$ compound, it is possible to have both Mn^{2+} and Fe^{2+} sharing the M^{2+} site, in

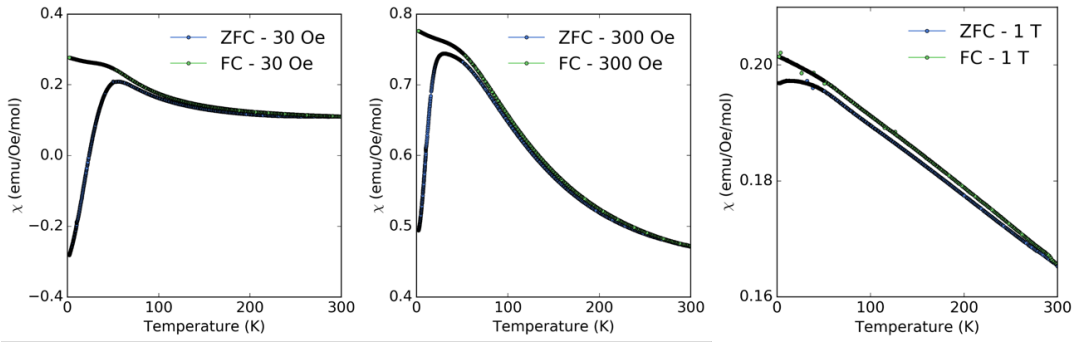

Figure 5.7: Magnetic susceptibility of $KCuFeSe_2$ with respect to temperature under a magnetic field of 30 Oe (left), 300 Oe (middle) and 1 T (right) showing the divergence between ZFC and FC becomes less pronounced at higher fields.

the same way that Cu and Mn or Fe share the overall M position in the 122-type structure. Since both $KCuMnS_2$, and $KCuFeS_2$ were synthesized using the same synthetic procedure, why then could you not create a solid solution series by adding both metals in the desired amount. Figure 5.12 shows the PXRD of a sample prepared using the described synthetic procedure for a desired concentration of $KCuMn_{0.8}Fe_{0.2}S_2$, or an M site concentration of 50 % Cu, 40 % Mn and 10 % Fe. As seen in the Figure, while a crystalline 122-type structure product was produced, there was also a not insignificant amount of alabandite (MnS) impurity.

As iron has been known to completely occupy the M site for $K_xFe_2S_2$ where x is anywhere from 0 to 1, [66] iron should be able to obtain an oxidation state in these compounds to not only replace the Mn^{2+}, but also the Cu^{1+}. Again, by adding metals together in the desired ratio of the final product, this time attempting to synthesis $KCu_{0.8}MnFe_{0.2}S_2$ for an overall M site concentration of 40 % Cu, 50 % Mn and 10 % Fe. As can be seen in Figure 5.13, again, while there was some 122-type

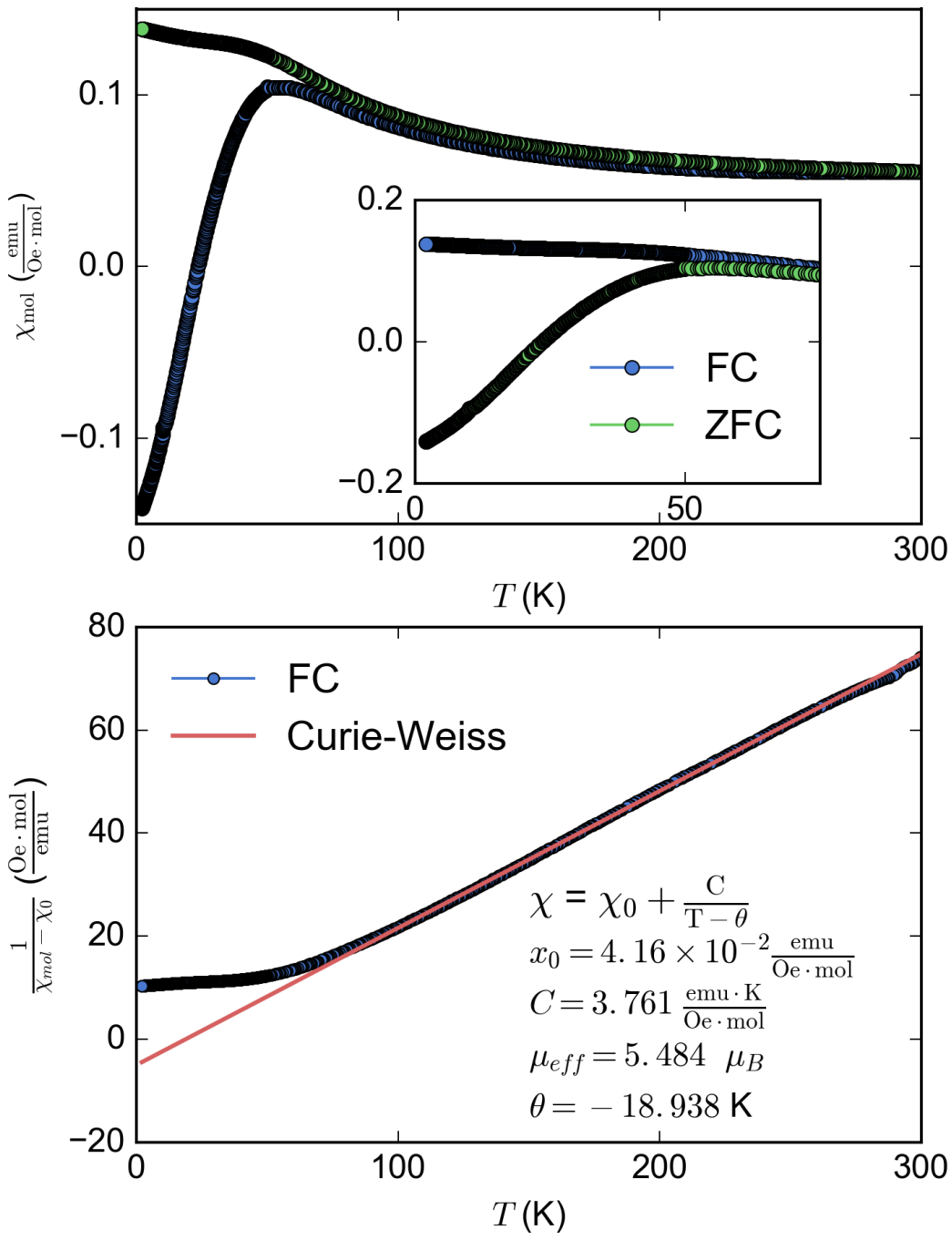

Figure 5.8: Extended magnetic susceptibility of $KCuFeSe_2$ (top) and the Curie-Weiss fit of $KCuFeSe_2$ (bottom) showing a calculated magnetic moment of 5.484 μ_B/ Fe^{2+} and a Weiss constant of -18.938 K.

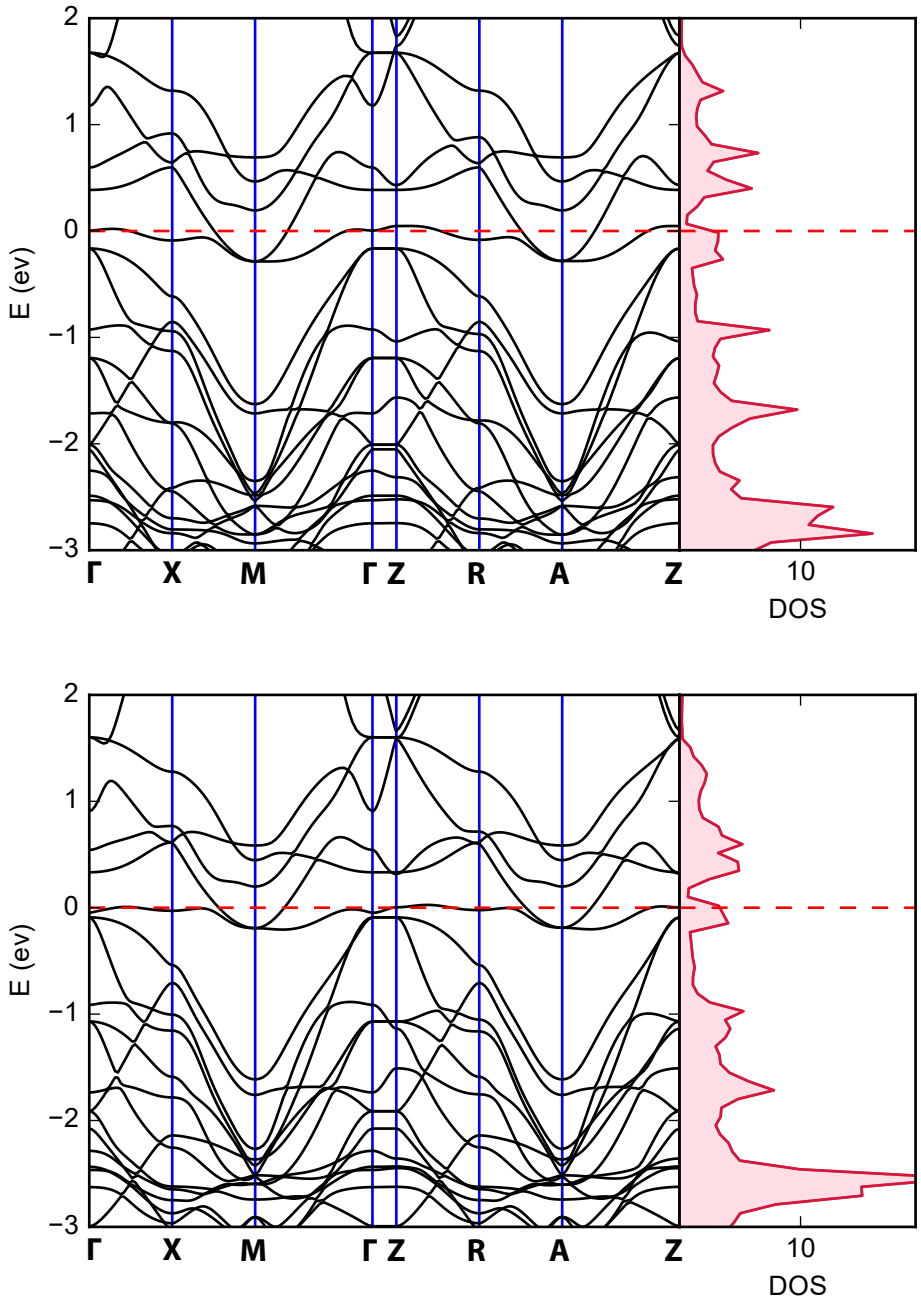

Figure 5.9: Dispersion curves and DOS of the electronic states near the Fermi-level for $KCuFeS_2$ (a) and $KCuFeSe_2$ (b) showing that both compounds are expected to be metallic.

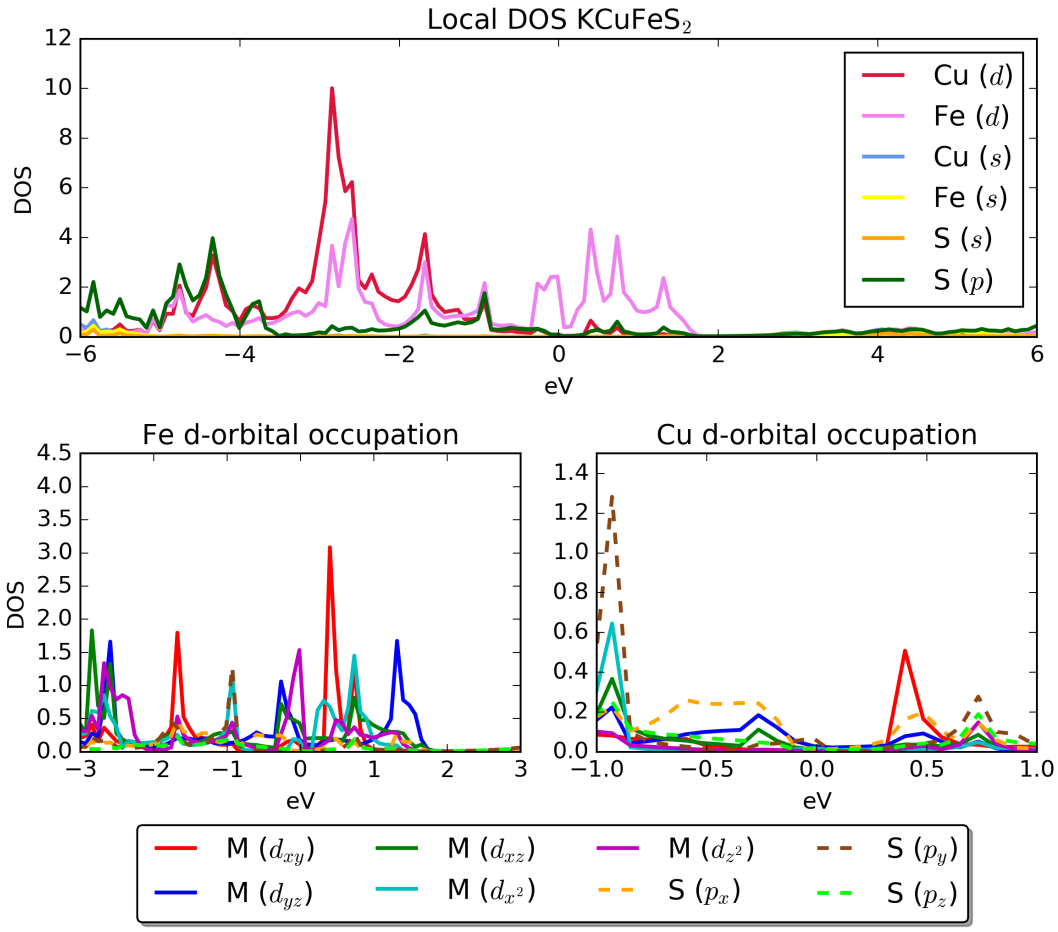

Figure 5.10: Local density of states for $KCuFeS_2$.

compound created, this time the alabandite impurity was even larger than for the $KCuMn_{0.8}Fe_{0.2}S_2$ attempt.

It appears that for each of these attempts, iron may have preferentially form the 122-type structure with copper, restricting reaction sites in the solid state procedure. It could also be that iron and manganese don't mix in the 122-type structure, as $KFeMnS_2$ is yet unknown.

While it is still theoretically possible to synthesis these compounds, it is clear that significantly more detail needs to be paid to the oxidation states of the compo-

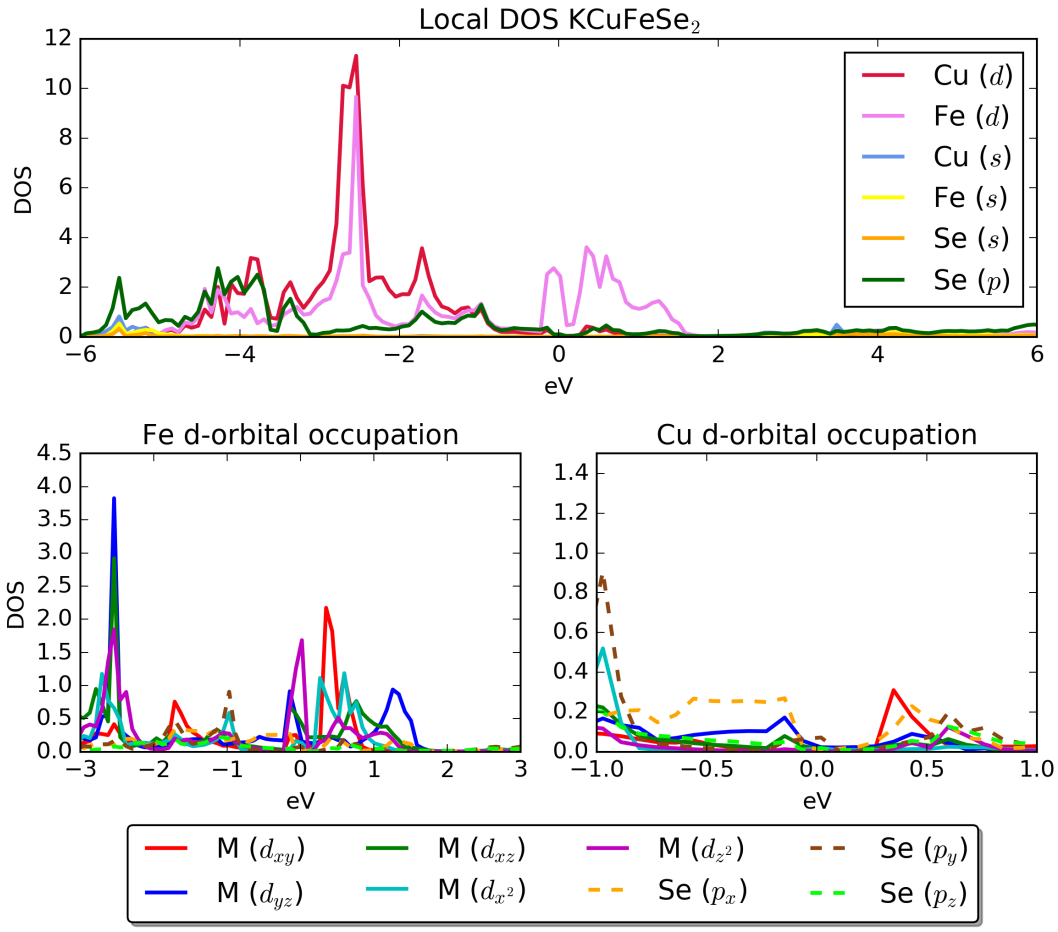

Figure 5.11: Local density of states for $KCuFeSe_2$.

nents of the desired product. More specifically, it is clear that the synthetic procedure is significantly less robust when multiple elements that can share an oxidation state site are used. Much more care would need to be taken in order to achieve the desired oxidation state for the individual components. As this procedure has already proven to be able to oxidize the pure metals into their desired oxidation states for $KCuMnS_2$, and $KCuFeS_2$, modified procedures would either need to use this to their advantage when starting with reduced metals, or find a way to prevent this if starting with reagents in the desired state.

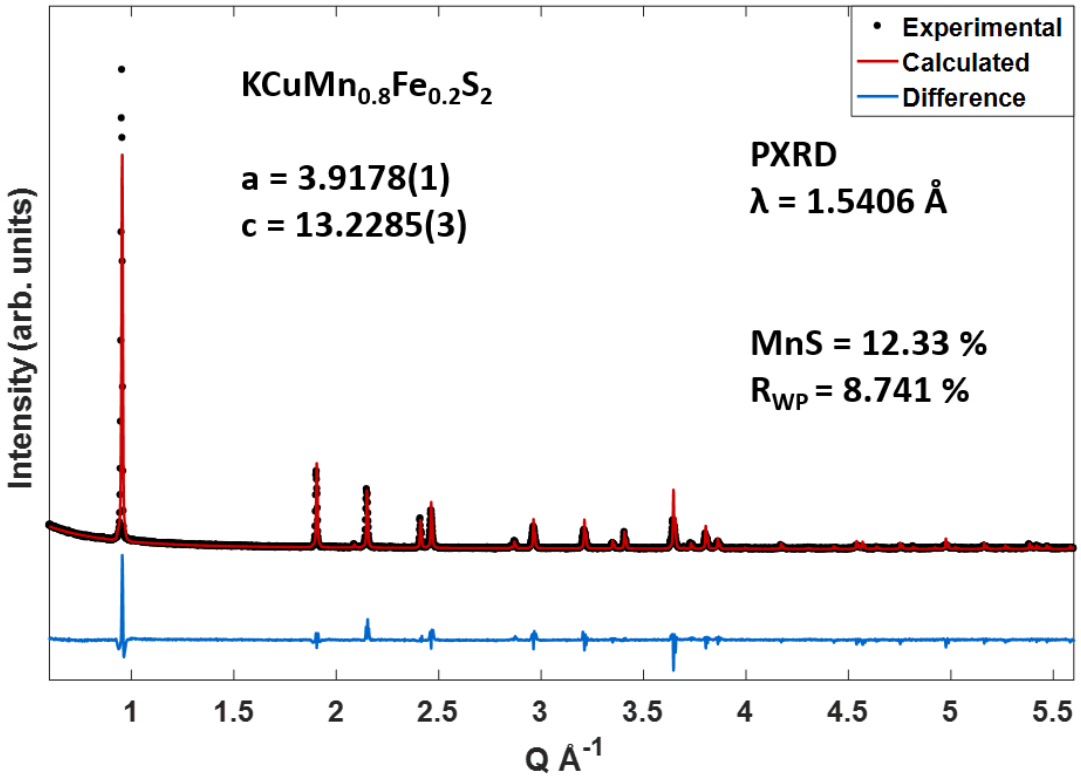

Figure 5.12: PXRD of $KCuMn_{0.8}Fe_{0.2}S_2$

It is unlikely that copper and manganese are in any states other than Cu^{1+} and Mn^{2+} when trying to add iron to their synthesis. Trying to change the nominal amount of these metals away from 1 : 1 even without any iron in the system causes equally disastrous results. Figure 5.14 is the PXRD from the attempted synthesis of $KCu_{0.9}Mn_{1.1}S_2$. This is only a 5 % excess of Mn and a 5 % deficiency of Cu. Likewise to the iron containing compounds, while there was primarily the 122-type structure characterized in the pattern, there was also a calculated 12.73 % alabandite impurity. Switching the excess and deficiency to a 5 % excess of Cu and a 5 % deficiency of Mn for $KCu_{1.1}Mn_{0.9}S_2$, as seen in Figure 5.15 also has a noticeable alabandite impurity. While not a large amount of alabandite, considering the original deficiency of Mn

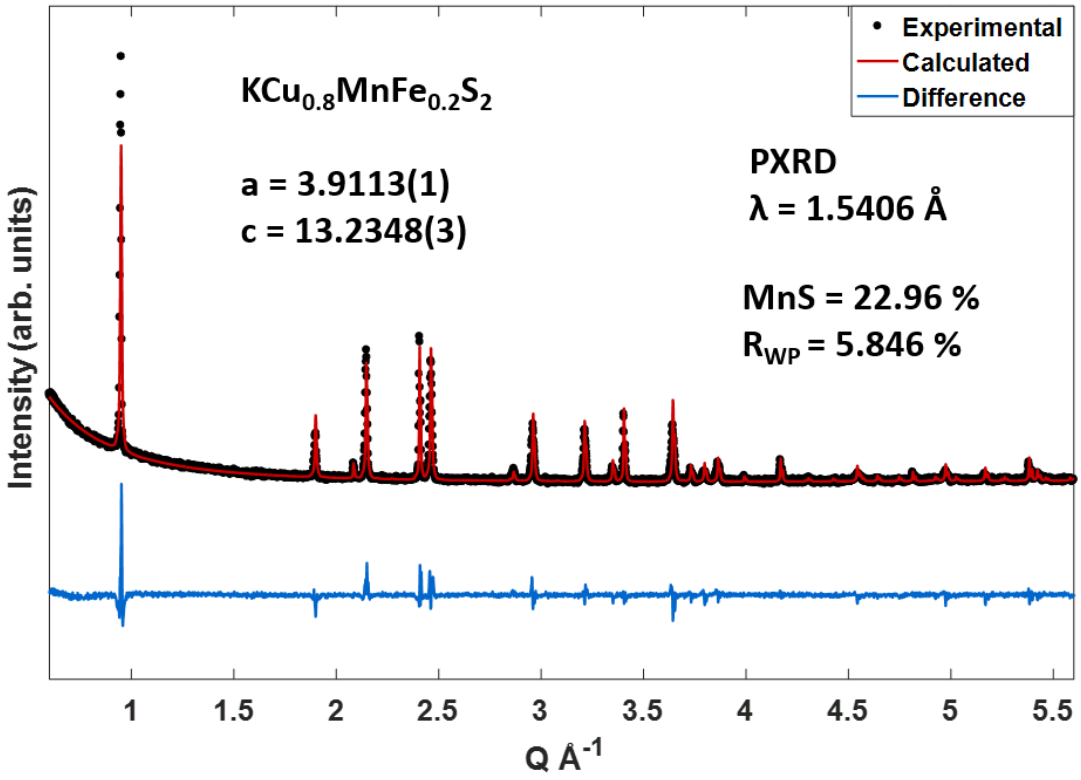

Figure 5.13: PXRD of $KCu_{0.8}MnFe_{0.2}S_2$

to begin with, even a 5.4 % impurity is significant.

Interestingly, for all of these PXRD patterns, each one was modeled using the 122-type structure and alabandite. There were no noticeable additional reflections from any copper or iron impurities, and attempts to fit unnoticeable ones (always inadvisable) proved fruitless. This would mean that any excess copper caused through this manganese deficiency would either, contrary to my previous assertion, occupy the M^{2+} site in order to facilitate the 122-type structure, or be lost elsewhere in amorphous impurities. While there is other indication that iron occupies both oxidation states other than the known absence of manganese in the compounds, there is that possibility, along with being lost as amorphous impurities. As these prod-

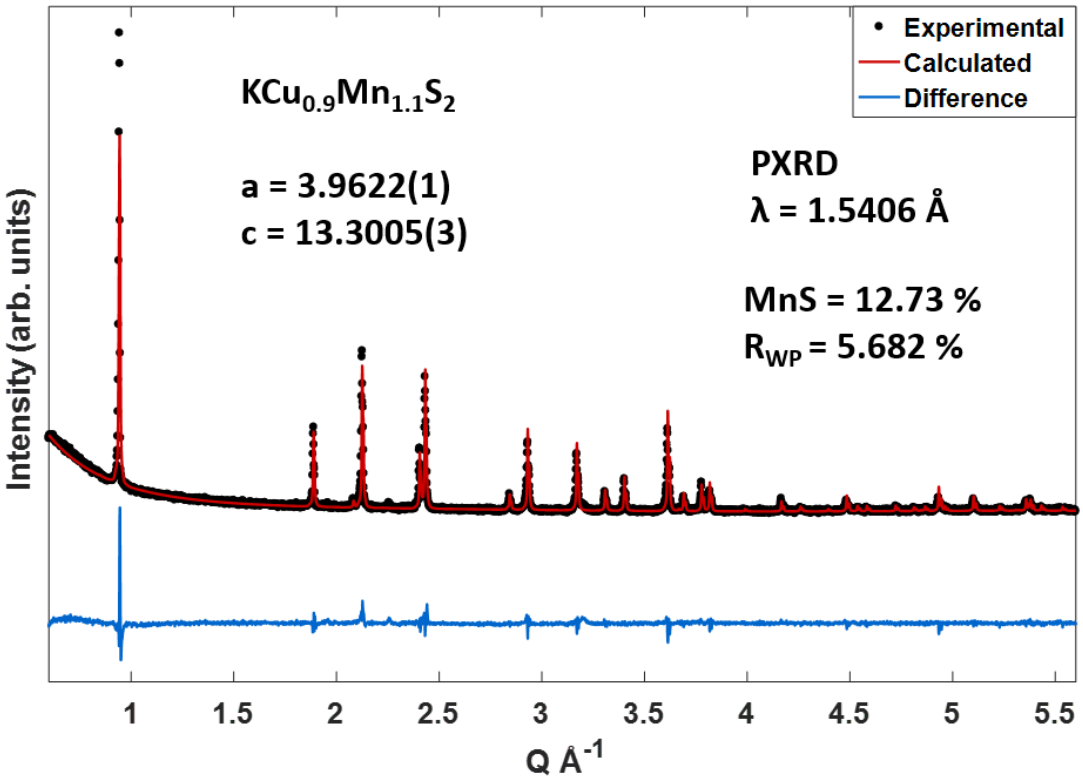

Figure 5.14: PXRD of $KCu_{0.9}Mn_{1.1}S_2$

ucts already have amorphous potassium polysulfide impurities, the amorphous metal impurities may be a part of one another.

All of these fits were refined from an initial $KCuMnS_2$ structure. The occupancies of the copper and manganese were held constant at 50 % of the site, even for the samples with added iron. Refining the occupancy of this position between these atoms would be extremely difficult given their similar X-ray scattering power. The fairly good R_{WP} values shows that even for compounds that we assume contain iron, treating it as manganese does not overly hinder the fitting. While there are characterization techniques that could help us determine the occupancies of this site, the alabandite impurity alone is enough to call for an improved synthetic method

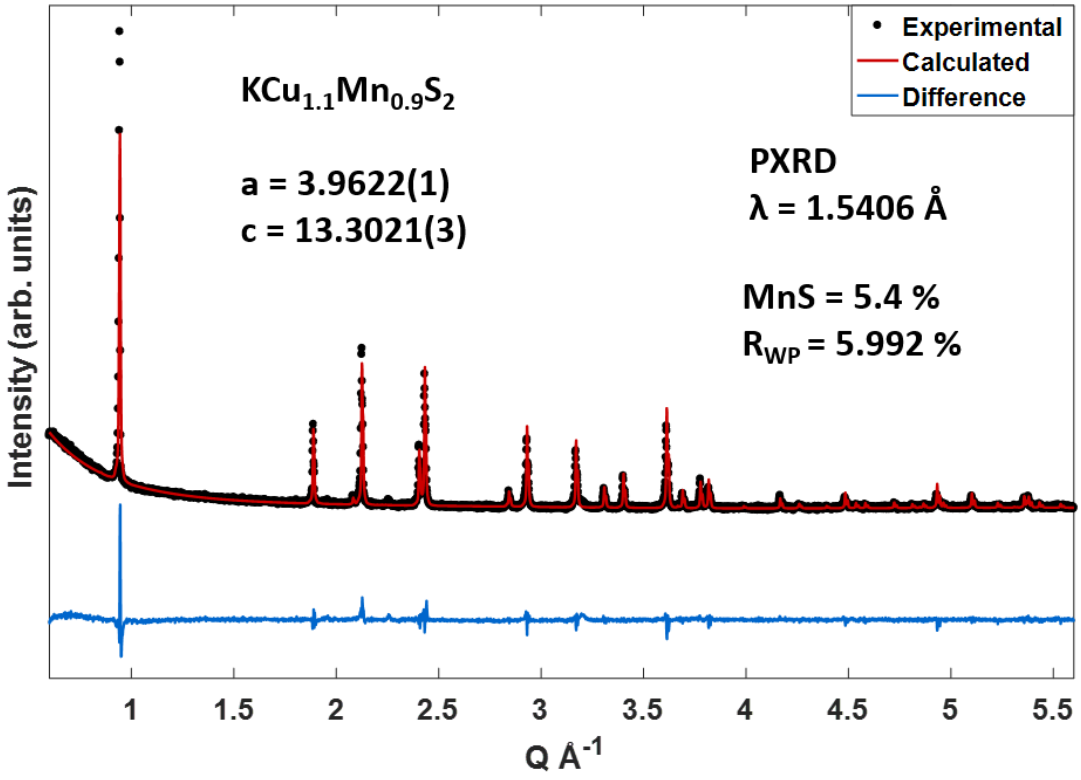

Figure 5.15: PXRD of $KCu_{1.1}Mn_{0.9}S_2$

before moving forward.

5.4 Conclusions

In conclusion, samples of $KCuFeS_2$ and $KCuFeSe_2$ were prepared for neutron diffraction studies and the magnetic susceptibility of $KCuFeSe_2$ is presented in relation to its calculated band structure. Neither compound shows the emergence of additional peaks between 3 and 70 K, though for $KCuFeSe_2$ there is a small amount of additional scattering for certain peaks. Both compounds are predicted to be metallic.

Attempts through now to modify these 122-type materials away from their

1112 stoichiometry have so far proven unsuccessful. Efforts to replace either manganese or copper in $KCuMnS_2$ with iron produce a large amount of alabandite (MnS) impurity. Efforts to change the ratio of copper to manganese in this compound away from a 1:1 ratio also produce alabandite impurity.

Chapter 6: Overall Conclusions and future work

6.1 Conclusions

In this work the properties of a range of 122-type compounds have been investigated. Particularly in regards to the affect that having a mixed metal site has on these compounds and the different types of MX_4 tetrahedra that they are comprised of.

Powder samples of these compounds have been prepared for neutron diffraction and properties measurements, and single crystals of $KCuMnS_2$ and $KCuMnSe_2$ have been prepared for further X-ray and neutron characterization. $KCuMnS_2$ becomes an antiferromagnet below a T_N near 160 K, and the first magnetic structures are proposed for $KCuMnS_2$. The substitution of Li^+ for Cu^+ in the compound completely destroys any long range ordering of the magnetic moments of Mn^{2+} down to 3.5 K. No crystallographic phase transition is observed for either single crystal X-ray data, or through neutron powder diffraction. The appearance of a forbidden peak in the MACS data for $KCuMnS_2$, could be due to the structural phase transition taking place below NPD data. A separate magnetic domain with seen with an onset temperature around 210 K, whose intensity dropped around the T_N of 160 K of the primary magnetic domain, indicating some interaction in the form of suppression.

The selenides of these samples were also created and showed similarities to their sulfides. As with its sulfide counterpart, $KCuMnSe_2$ also has long range ordering of its magnetic moment, though the structure of this magnetic domain is, as yet, unknown. Also like its sulfide counterpart, $KLiMnSe_2$ has no long range ordering of its magnetic moment, though there is one small feature that can be seen at 3.5 K that is gone by 20 K. The electrical properties of these materials is also discussed in relation to their calculated band structures, with $KCuMnSe_2$ being a semiconductor and $KLiMnSe_2$ being an insulator.

Finally, additional 122-type compounds are presented. The neutron powder diffraction patterns of $KCuFeS_2$ and $KCuFeSe_2$ are shown, and attempts at varying the metal concentration away from the 1112 structural formula are presented. Both $KCuFeS_2$ and $KCuFeSe_2$ are expected to be metallic based off of their density of states calculations. While the 122-type structure has shown to be accommodating for accepting a mixed metal site when one metal is in the +1 oxidation state and the other is in the +2 oxidation state, attempts at introducing a third metal into the site to share either of the oxidation states have failed. Attempts at slightly modifying the ratio of the +1 and +2 metals away from 1:1 has also proven difficult. Even so, doping for these types of materials is well known and the avenue is still an exciting one.

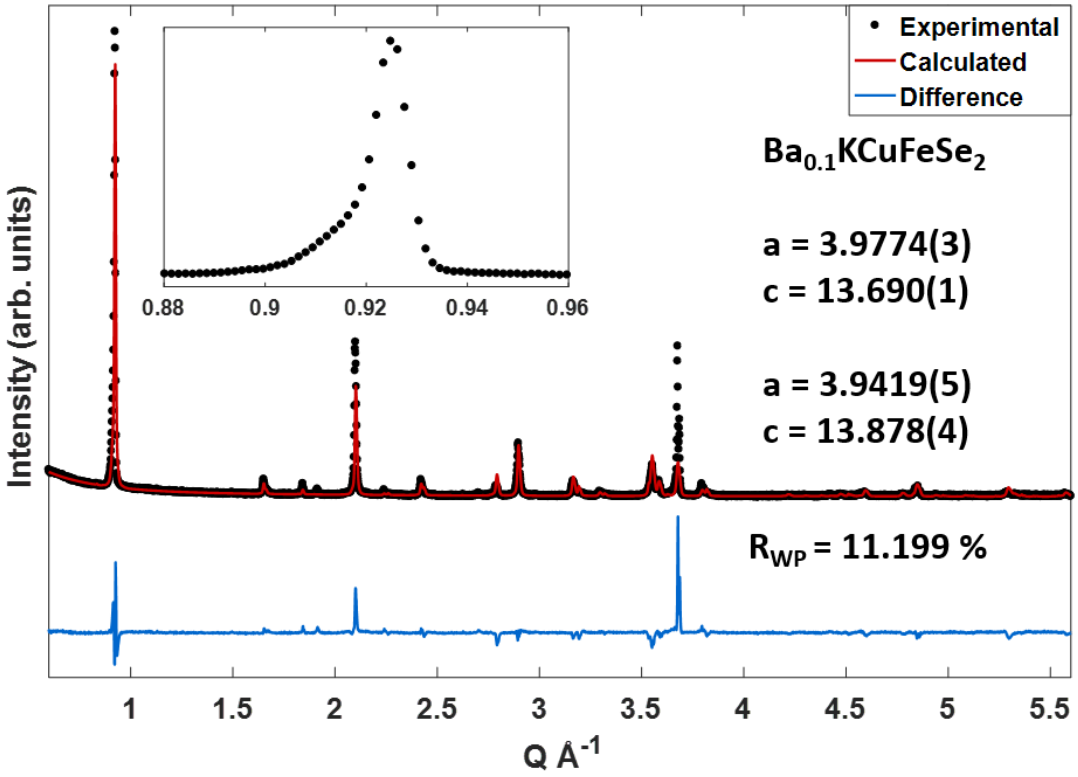

Figure 6.1: PXRD of $Ba_xK_yCuFeSe_2$

6.2 Future Work

Just because it has proven difficult to tune the metal sites between different metals with the same oxidation state as discussed in chapter 5, does not mean we have exhausted all way to modify this system. Indeed the first 122-type superconductor was achieved by varying, not the metal component, but the cation A. The $BaFe_2As_2$ system itself, is not superconducting, but $Ba_{1-x}K_xFe_2As_2$ is when x is about 0.4. [27]

Initial attempts to recreate the mixture of barium and potassium in the A cite for our own compounds has produced some interesting results. Trying to incorporate a 10 % excess of Ba into $KCuFeSe_2$, there were no noticeable impurity phases.

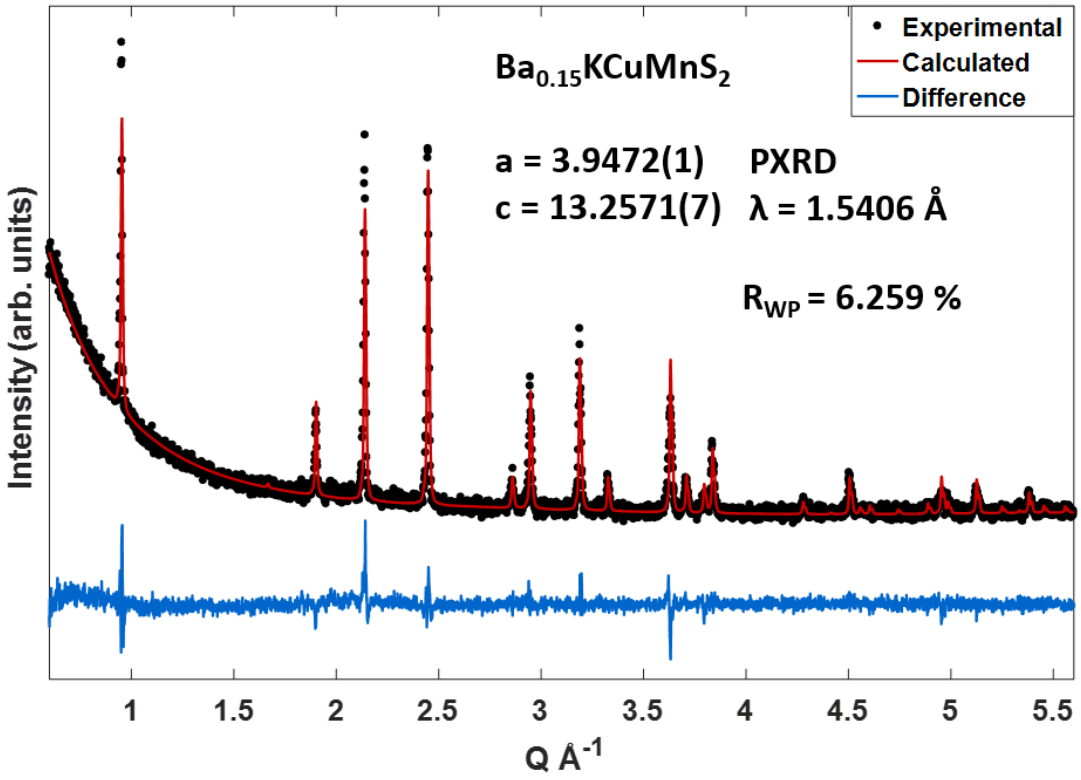

Figure 6.2: PXRD of $Ba_xK_yCuMnS_2$

However, there was a distinct saw-tooth profile to all of the Bragg reflections as seen in the inset in Figure 6.1. This saw-tooth pattern was fit using two different 122-type profiles, thus the two different lattice parameter profiles in Figure 6.1. One profile is slightly compressed along the c-axis while having an extended a-axis, if only slightly. This is a hallmark when comparing compounds with A^{1+} cations, and A^{2+} cations. It is difficult to differentiate a site based solely off of PXRD, even though the difference in their electron densities is large, subtle variation would still pose a problem. This makes it difficult to tell if we are actually electron doping the system or maintaining the charge balance by losing twice as many A^{1+} cations as we are gaining A^{2+} cations.

Attempts to incorporate barium into $KCuMnS_2$ also showed some promise, as an attempt to synthesis $Ba_xK_yCuMnS_2$ by simply adding a 15 % concentration of barium carbonate to the synthetic procedure for $KCuMnS_2$, produced a seemingly crystallographically phase pure compound. Refining only the potassium site occupied by potassium, gives an occupancy of 1.23(1) indicating some heavier atom in the site. Though given the inherent potassium excess in the original procedure to begin with, further testing would be required to definitively determine any barium occupancy in the site. Of course, any attempts at creating subtle variations with specific occupancies would require accurate elemental analysis. Inductively coupled plasma atomic emission spectroscopy (ICP-AES) has proven difficult as these compounds have proven to be very stable in the nitric acid necessary for the measurements. Other options would have to be sought, such as X-ray photoelectron spectroscopy, which could also provide insight not only to the elemental composition, but also the oxidation state of the transition metals involved.

Appendix A: Additional DFT, and Refinement Parameters

Table A.1: optimized lattice parameters, starting magnetic structure, optimized magnetic structure and corresponding moment, and ground state energies of each calculated phase

Compound	a ($\AA$)	c ($\AA$)	Starting magnetic structure	Optimized magnetic structure	Optimized magnetic moment	Ground state electronic energy (eV)
$KCuMnS_2$	3.9625	13.459	Layered Checkerboard AFM (-5, 5 μ_B Mn)	Layered Checkerboard AFM	($\pm 4.089 \mu_B$) Mn Net moment = 0.000 μ_B	-51.342
$KCuMnSe_2$	4.1018	14.050	Layered Checkerboard AFM (-5, 5 μ_B Mn)	Layered Checkerboard AFM	($\pm 4.123 \mu_B$) Mn Net moment = 0.000 μ_B	-48.131
$KCuFeS_2$	3.8775	13.3304	Layered Checkerboard AFM (-5, 5 μ_B Fe)	Layered Checkerboard AFM	($\pm 3.118 \mu_B$) Fe Net moment = 0.000 μ_B	-48.911
$KCuFeSe_2$	4.0136	13.955	Layered Checkerboard AFM (-5, 5 μ_B Fe)	Layered Checkerboard AFM	($\pm 3.137 \mu_B$) Fe Net moment = 0.000 μ_B	-45.525
$KLiMnS_2$	4.071	13.331	None	Layered ferromagnetism	($4.199 \mu_B$) Mn Net moment = 8.400 μ_B	-50.822
$KLiMnSe_2$	4.235	13.953	Layered Checkerboard AFM (-5, 5 μ_B Mn)	Layered Checkerboard AFM	($4.261 \mu_B$) Mn Net moment = 0.000 μ_B	-47.607

Table A.2: Structural parameters for $KLiMnS_2$ at 3.5 K from NPD.

$I4/mmm$ $a = 4.0312(2)$ (Å) $c = 13.1453(8)$ (Å) $R_{wp} = 7.019$ %

Atom	Wyckoff Site	x	y	z	Occ
K	2a	0	0	0.5	1
Li	4d	0.5	0	0.25	0.489(6)
Mn	4d	0.5	0	0.25	0.48(1)
S	4e	0.5	0.5	0.3536(3)	1

Table A.3: Structural parameters for $KLiMnSe_2$ at 200 K from NPD.

$I4/mmm$ $a = 4.2041(3)$ (Å) $c = 13.715(1)$ (Å) $R_{wp} = 9.502$ %

Atom	Wyckoff Site	x	y	z	Occ
K	2a	0	0	0.5	1
Li	4d	0.5	0	0.25	0.43(3)
Mn	4d	0.5	0	0.25	0.46(1)
Se	4e	0.5	0.5	0.3542(3)	1

Table A.4: Structural parameters for $KLiMnSe_2$ at 3.5 K from NPD. * Occupancy held constant from those refined at 200 K.

$I4/mmm$ $a = 4.1903(3)$ (Å) $c = 13.659(1)$ (Å) $R_{wp} = 8.319$ %

Atom	Wyckoff Site	x	y	z	Occ
K	2a	0	0	0.5	1
Li	4d	0.5	0	0.25	0.43*
Mn	4d	0.5	0	0.25	0.46*
Se	4e	0.5	0.5	0.3555(3)	1

Table A.5: Structural parameters for $KCuFeS_2$ at 70 K from NPD.

$I4/mmm$ $a = 3.8455(1)$ (Å) $c = 13.0976(6)$ (Å) $R_{wp} = 9.430$ %

Atom	Wyckoff Site	x	y	z	Occ
K	2a	0	0	0.5	1
Cu	4d	0.5	0	0.25	0.5
Fe	4d	0.5	0	0.25	0.5
S	4e	0.5	0.5	0.3500(3)	1

Table A.6: Structural parameters for $KCuFeSe_2$ at 70 K from NPD.

$I4/mmm$ $a = 3.9690(1)$ (Å) $c = 13.711(1)$ (Å) $R_{wp} = 10.501$ %

Atom	Wyckoff Site	x	y	z	Occ
K	2a	0	0	0.5	1
Cu	4d	0.5	0	0.25	0.5
Fe	4d	0.5	0	0.25	0.5
Se	4e	0.5	0.5	0.3610(2)	1

Bibliography

[1] Yoichi Kamihara, Takumi Watanabe, Masahiro Hirano, and Hideo Hosono. Iron-Based Layered Superconductor La[$O_1 - xF_x$]FeAs (x = 0.05 0.12) with T_c = 26 K. *Journal of the American Chemical Society*, 130(11):3296–3297, mar 2008.

[2] P Quebe, L.J Terbüchte, and W Jeitschko. Quaternary rare earth transition metal arsenide oxides RTAsO (T=Fe, Ru, Co) with ZrCuSiAs type structure. *Journal of Alloys and Compounds*, 302(1-2):70–74, apr 2000.

[3] Clarina de la Cruz, Q. Huang, J. W. Lynn, Jiying Li, W. Ratcliff II, J. L. Zarestky, H. A. Mook, G. F. Chen, J. L. Luo, N. L. Wang, and Pengcheng Dai. Magnetic order close to superconductivity in the iron-based layered $LaO_{1-x}F_x$ FeAs systems. *Nature*, 453(7197):899–902, jun 2008.

[4] Jun Zhao, Q. Huang, Clarina de la Cruz, Shiliang Li, J. W. Lynn, Y. Chen, M. A. Green, G. F. Chen, G. Li, Z. Li, J. L. Luo, N. L. Wang, and Pengcheng Dai. Structural and magnetic phase diagram of CeFeAsO1 xF x and its relation to high-temperature superconductivity. *Nature Materials*, 7(12):953–959, dec 2008.

[5] Jun Zhao, Q. Huang, Clarina de la Cruz, J. W. Lynn, M. D. Lumsden, Z. A. Ren, Jie Yang, Xiaolin Shen, Xiaoli Dong, Zhongxian Zhao, and Pengcheng Dai. Lattice and magnetic structures of PrFeAsO, $PrFeAsO_{0.85}F_{0.15}$, and $PrFeAsO_{0.85}$. *Physical Review B*, 78(13):132504, oct 2008.

[6] G. F. Chen, Z. Li, D. Wu, G. Li, W. Z. Hu, J. Dong, P. Zheng, J. L. Luo, and N. L. Wang. Superconductivity at 41 K and Its Competition with Spin-Density-Wave Instability in Layered $CeO_{1-x}F_x$FeAs. *Physical Review Letters*, 100(24):247002, jun 2008.

[7] Z. A. Ren, J. Yang, W. Lu, W. Yi, G. C. Che, X. L. Dong, L. L. Sun, and Z. X. Zhao. Superconductivity at 52 K in iron based F doped layered quaternary compound Pr[O_1xF_x]FeAs. *Materials Research Innovations*, 12(3):105–106, sep 2008.

[8] J. Prakash, S. J. Singh, S. L. Samal, S. Patnaik, and A. K. Ganguli. Potassium fluoride doped LaOFeAs multi-band superconductor: Evidence of extremely high upper critical field. *EPL (Europhysics Letters)*, 84(5):57003, dec 2008.

[9] X. H. Chen, T. Wu, G. Wu, R. H. Liu, H. Chen, and D. F. Fang. Superconductivity at 43 K in $SmFeAsO_{1-x}F_x$. *Nature*, 453(7196):761–762, jun 2008.

[10] Zhi-An Ren, Jie Yang, Wei Lu, Wei Yi, Xiao-Li Shen, Zheng-Cai Li, Guang-Can Che, Xiao-Li Dong, Li-Ling Sun, Fang Zhou, and Zhong-Xian Zhao. Superconductivity in the iron-based F-doped layered quaternary compound $Nd[O_1xF_x]FeAs$. *EPL (Europhysics Letters)*, 82(5):57002, jun 2008.

[11] Ren Zhi-An, Lu Wei, Yang Jie, Yi Wei, Shen Xiao-Li, Zheng-Cai, Che Guang-Can, Dong Xiao-Li, Sun Li-Ling, Zhou Fang, and Zhao Zhong-Xian. Superconductivity at 55 K in Iron-Based F-Doped Layered Quaternary Compound $Sm[O_1xF_x]$ FeAs. *Chinese Physics Letters*, 25(6):2215–2216, jun 2008.

[12] Jie Yang, Zheng-Cai Li, Wei Lu, Wei Yi, Xiao-Li Shen, Zhi-An Ren, Guang-Can Che, Xiao-Li Dong, Li-Ling Sun, Fang Zhou, and Zhong-Xian Zhao. Superconductivity at 53.5 K in GdFeAsO 1δ. *Superconductor Science and Technology*, 21(8):082001, aug 2008.

[13] Jan-Willem G. Bos, George B. S. Penny, Jennifer A. Rodgers, Dmitry A. Sokolov, Andrew D. Huxley, and J. Paul Attfield. High pressure synthesis of late rare earth RFeAs(O,F) superconductors; R = Tb and Dy. *Chemical Communications*, (31):3634, 2008.

[14] N. Qureshi, Y. Drees, J. Werner, S. Wurmehl, C. Hess, R. Klingeler, B. Büchner, M. T. Fernández-Díaz, and M. Braden. Crystal and magnetic structure of the oxypnictide superconductor $LaFeAsO_{1-x}F_x$: A neutron-diffraction study. *Physical Review B*, 82(18):184521, nov 2010.

[15] J. Prakash, S. J. Singh, A. Banerjee, S. Patnaik, and A. K. Ganguli. Enhancement in transition temperature and upper critical field of $CeO_{0.8}F_{0.2}FeAs$ by yttrium doping. *Applied Physics Letters*, 95(26):262507, dec 2009.

[16] J Prakash, S J Singh, S Patnaik, and A K Ganguli. Upper critical field, superconducting energy gaps and the Seebeck coefficient in $La_{0.8}Th_{0.2}FeAsO$. *Journal of Physics: Condensed Matter*, 21(17):175705, apr 2009.

[17] J. Prakash, S.J. Singh, D. Das, S. Patnaik, and A.K. Ganguli. New oxypnictide superconductors: $PrOFe_{1x}Co_xAs$. *Journal of Solid State Chemistry*, 183(2):338–343, feb 2010.

[18] Athena S. Sefat, Ashfia Huq, Michael A. McGuire, Rongying Jin, Brian C. Sales, David Mandrus, Lachlan M. D. Cranswick, Peter W. Stephens, and Kevin H. Stone. Superconductivity in $LaFe_{1x}Co_xAsO$. *Physical Review B*, 78(10):104505, sep 2008.

[19] Yanpeng Qi, Zhaoshun Gao, Lei Wang, Dongliang Wang, Xianping Zhang, and Yanwei Ma. Superconductivity in Co-doped SmFeAsO. *Superconductor Science and Technology*, 21(11):115016, nov 2008.

[20] Chul-Ho Lee, Akira Iyo, Hiroshi Eisaki, Hijiri Kito, Maria Teresa Fernandez-Diaz, Toshimitsu Ito, Kunihiro Kihou, Hirofumi Matsuhata, Markus Braden, and Kazuyoshi Yamada. Effect of Structural Parameters on Superconductivity in Fluorine-Free $LnFeAsO_{1-y}$(Ln = La, Nd). *Journal of the Physical Society of Japan*, 77(8):083704, aug 2008.

[21] Dinah R. Parker, Michael J. Pitcher, Peter J. Baker, Isabel Franke, Tom Lancaster, Stephen J. Blundell, and Simon J. Clarke. Structure, antiferromagnetism and superconductivity of the layered iron arsenide NaFeAs. *Chemical Communications*, (16):2189, 2009.

[22] Shiliang Li, Clarina de la Cruz, Q. Huang, G. F. Chen, T.-L. Xia, J. L. Luo, N. L. Wang, and Pengcheng Dai. Structural and magnetic phase transitions in $Na_{1-\delta}FeAs$. *Physical Review B*, 80(2):020504, jul 2009.

[23] G. F. Chen, W. Z. Hu, J. L. Luo, and N. L. Wang. Multiple Phase Transitions in Single-Crystalline $Na_{1-\delta}FeAs$. *Physical Review Letters*, 102(22):227004, jun 2009.

[24] F.-C. Hsu, J.-Y. Luo, K.-W. Yeh, T.-K. Chen, T.-W. Huang, P. M. Wu, Y.-C. Lee, Y.-L. Huang, Y.-Y. Chu, D.-C. Yan, and M.-K. Wu. Superconductivity in the PbO-type structure -FeSe. *Proceedings of the National Academy of Sciences*, 105(38):14262–14264, sep 2008.

[25] T. M. McQueen, Q. Huang, V. Ksenofontov, C. Felser, Q. Xu, H. Zandbergen, Y. S. Hor, J. Allred, A. J. Williams, D. Qu, J. Checkelsky, N. P. Ong, and R. J. Cava. Extreme sensitivity of superconductivity to stoichiometry in $Fe_{1+\delta}Se$. *Physical Review B*, 79(1):014522, jan 2009.

[26] Marianne Rotter, Michael Pangerl, Marcus Tegel, and Dirk Johrendt. Superconductivity and Crystal Structures of $(Ba_{1x}K_x)Fe_2As_2$(x =0-1). *Angewandte Chemie International Edition*, 47(41):7949–7952, sep 2008.

[27] Marianne Rotter, Marcus Tegel, and Dirk Johrendt. Superconductivity at 38 K in the Iron Arsenide $(Ba_{1x}K_x)Fe_2As_2$. *Physical Review Letters*, 101(10):107006, sep 2008.

[28] Athena S. Sefat, Rongying Jin, Michael A. McGuire, Brian C. Sales, David J. Singh, and David Mandrus. Superconductivity at 22 K in Co-Doped $BaFe_2As_2$ Crystals. *Physical Review Letters*, 101(11):117004, sep 2008.

[29] Q. Huang, Y. Qiu, Wei Bao, M. A. Green, J. W. Lynn, Y. C. Gasparovic, T. Wu, G. Wu, and X. H. Chen. Neutron-Diffraction Measurements of Magnetic Order and a Structural Transition in the Parent $BaFe_2As_2$ Compound

of FeAs-Based High-Temperature Superconductors. *Physical Review Letters*, 101(25):257003, dec 2008.

[30] S. R. Saha, N. P. Butch, T. Drye, J. Magill, S. Ziemak, K. Kirshenbaum, P. Y. Zavalij, J. W. Lynn, and J. Paglione. Structural collapse and superconductivity in rare-earth-doped $CaFe_2As_2$. *Physical Review B*, 85(2):024525, jan 2012.

[31] Z. Ban and M. Sikirica. The crystal structure of ternary silicides ThM_2Si_2 (M = Cr, Mn, Fe, Co, Ni and Cu). *Acta Crystallographica*, 18(4):594–599, apr 1965.

[32] E. Parthé, B. Chabot, H. F. Braun, and N. Engel. Ternary $BaAl_4$-type derivative structures. *Acta Crystallographica Section B Structural Science*, 39(5):588–595, oct 1983.

[33] W.B. Pearson. The most populous of all crystal structure typesthe tetragonal $BaAl_4$ structure. *Journal of Solid State Chemistry*, 56(3):278–287, mar 1985.

[34] Roald Hoffmann and Chong Zheng. Making and breaking bonds in the solid state: the thorium chromium silicide ($ThCr_2Si_2$) structure. *The Journal of Physical Chemistry*, 89(20):4175–4181, sep 1985.

[35] Dirk Johrendt, Claudia Felser, Ove Jepsen, Ole Krogh Andersen, Albrecht Mewis, and Jean Rouxel. LMTO Band Structure Calculations of $ThCr_2Si_2$-Type Transition Metal Compounds. *Journal of Solid State Chemistry*, 130(2):254–265, may 1997.

[36] Ulrich Häussermann, Shahrad Amerioun, Lars Eriksson, Chi-Shen Lee, and Gordon J. Miller. The s p Bonded Representatives of the Prominent $BaAl_4$ Structure Type: A Case Study on Structural Stability of Polar Intermetallic Network Structures. *Journal of the American Chemical Society*, 124(16):4371–4383, apr 2002.

[37] Wanyue Peng, Sevan Chanakian, and Alexandra Zevalkink. Crystal chemistry and thermoelectric transport of layered AM_2X_2 compounds. *Inorganic Chemistry Frontiers*, 5(8):1744–1759, 2018.

[38] Andrzej Szytuła and Janusz Leciejewicz. Chapter 83 Magnetic properties of ternary intermetallic compounds of the RT_2X_2 type. pages 133–211. 1989.

[39] G. Huan, M. Greenblatt, and M. Croft. New ternary transition metal chalcogenides AM_2X_2 (A = K, Rb, Cs, M = Co, A = K, M = Ni, X = S, Se) - magnetically ordered metals with $ThCr_2Si_2$-Type structure. *Eur. J. Solid State Inorg. Chem.*, 26(2):193–220, 1989.

[40] Xiaoyan Tan, Zachary P. Tener, and Michael Shatruk. Correlating Itinerant Magnetism in RCo_2Pn_2 Pnictides (R = La, Ce, Pr, Nd, Eu, Ca; Pn = P, As)

to Their Crystal and Electronic Structures. *Accounts of Chemical Research*, 51(2):230–239, feb 2018.

[41] Paul C. Canfield and Sergey L. Bud'ko. FeAs-Based Superconductivity: A Case Study of the Effects of Transition Metal Doping on $BaFe_2As_2$. *Annual Review of Condensed Matter Physics*, 1(1):27–50, aug 2010.

[42] K-H Müller and V N Narozhnyi. Interaction of superconductivity and magnetism in borocarbide superconductors. *Reports on Progress in Physics*, 64(8):943–1008, aug 2001.

[43] Ashok K. Ganguli and Jai Prakash. Iron-Based Superconductors with Extended FeX_4 (X = As and Se) Tetrahedra. *European Journal of Inorganic Chemistry*, 2011(26):3868–3876, sep 2011.

[44] A.L. Ivanovskii. New ternary $ThCr_2Si_2$-type ironselenide superconducting materials: Synthesis, properties and simulations. *Physica C: Superconductivity*, 471(13-14):409–427, jul 2011.

[45] Michael Shatruk. $ThCr_2Si_2$ structure type: The perovskite of intermetallics. *Journal of Solid State Chemistry*, 272:198–209, apr 2019.

[46] K.R. Andress and Alberti E. X-Ray Investigation of Aluminum-Barium Alloys. *Z. Metallkd*, 27:126–128, 1935.

[47] M Oledzka, CL Lee, KV Ramanujachary, and M Greenblatt. PREPARATION AND PROPERTIES OF LOW-DIMENSIONAL QUATERNARY SULFIDES: $ACuMnS_2$ (A= K, Rb, Cs). *Materials Research Bulletin*, 32(7):889–898, 1997.

[48] M Oledzka, K.V Ramanujachary, and M Greenblatt. Synthesis and characterization of new quaternary selenides with $ThCr_2Si_2$-type structure: $ACuMnSe_2$ (A = K, Rb, Cs). *Mater. Res. Bull.*, 33(6):855 – 866, 1998.

[49] A.R. Newmark, G. Huan, M. Greenblatt, and M. Croft. Magnetic ordering in $TlCo_{2-x}Ni_xSe_2$ with the $ThCr_2Si_2$ structure. *Solid State Communications*, 71(11):1025–1032, sep 1989.

[50] M. Oledzka, K. V. Ramanujachary, and M. Greenblatt. Physical properties of quaternary mixed transition metal sulfides: $ACuFeS_2$(A = K, Rb, Cs). *Materials Research Bulletin*, 31(12):1491–1499, dec 1996.

[51] M. Oledzka, J.-G. Lee, K.V. Ramanujachary, and M. Greenblatt. Synthesis and Characterization of Quaternary Sulfides with $ThCr_2Si_2$-Type Structure: $KCo_{2x}Cu_xS_2(0.5 \leq x \leq 1.5)$ and $ACoCuS_2$(A= K, Rb, Cs). *Journal of Solid State Chemistry*, 127(2):151–160, dec 1996.

[52] Chong. Zheng and Roald. Hoffmann. Donor-acceptor layer formation and lattice site preference in the solid: the $CaBe_2Ge_2$ structure. *Journal of the American Chemical Society*, 108(11):3078–3088, may 1986.

[53] Chong Zheng and Roald Hoffmann. An Unusual Electron Count and Electron-Deficient Multi-Center Bonding in One Class of Intermetallics: The $BaAl_4$, $CaAl_2Zn_2$, $CeMg_2Si_2$ and FCC Al Structures. *Zeitschrift für Naturforschung B*, 41(3):292–320, mar 1986.

[54] Gerhard Cordier, Erwin Czech, and Herbert Schäfer. CaZn2Al2, der erste Vertreter einer inversen ThCr2Si2-Struktur / CaZn2Al2, the First Example of an Inverse ThCr2Si2-Structure. *Zeitschrift für Naturforschung B*, 39(12):1629–1632, dec 1984.

[55] Gerhard Cordier, Gregor Dörsam, and Caroline Röhr. Neue ternäre vertreter des $ThCr_2Si_2$- und des $CaZn_2Al_2$-Struktur-typs in den systemen A-T-X und RE-T-X (A Ca, Sr, Ba; RE La, Ce, Pr; T Cu, Ag, Au und X Al, Ga). *Journal of the Less Common Metals*, 166(1):115–124, oct 1990.

[56] C. Huhnt, G. Michels, M. Roepke, W. Schlabitz, A. Wurth, D. Johrendt, and A. Mewis. First-order phase transitions in the $ThCr_2Si_2$-type phosphides ARh_2P_2 (A = Sr, Eu). *Physica B: Condensed Matter*, 240(1-2):26–37, sep 1997.

[57] N. Ni, S. Nandi, A. Kreyssig, A. I. Goldman, E. D. Mun, S. L. Bud'ko, and P. C. Canfield. First-order structural phase transition in $CaFe_2As_2$. *Physical Review B*, 78(1):014523, jul 2008.

[58] Marcus Tegel, Marianne Rotter, Veronika Weiß, Falko M Schappacher, Rainer Pöttgen, and Dirk Johrendt. Structural and magnetic phase transitions in the ternary iron arsenides $SrFe_2As_2$and $EuFe_2As_2$. *Journal of Physics: Condensed Matter*, 20(45):452201, nov 2008.

[59] Marianne Rotter, Marcus Tegel, Dirk Johrendt, Inga Schellenberg, Wilfried Hermes, and Rainer Pöttgen. Spin-density-wave anomaly at 140 K in the ternary iron arsenide $BaFe_2As_2$. *Physical Review B*, 78(2):020503, jul 2008.

[60] R Mittal, S K Mishra, S L Chaplot, S V Ovsyannikov, E Greenberg, D M Trots, L Dubrovinsky, Y Su, Th Brueckel, S Matsuishi, H Hosono, and G Garbarino. Ambient- and low-temperature synchrotron x-ray diffraction study of $BaFe_2As_2$ and $CaFe_2As_2$ at high pressures up to 56 GPa. *Physical Review B - Condensed Matter and Materials Physics*, 83(5):054503, feb 2011.

[61] Albrecht Mewis. Ternäre Phosphide mit $ThCr_2Si_2$ -Struktur / Ternary Phosphides with the $ThCr_2Si_2$ Structure. *Zeitschrift für Naturforschung B*, 35(2):141–145, feb 1980.

[62] Svilen Bobev, Sheng-qing Xia, Eric D. Bauer, Filip Ronning, Joe D. Thompson, and John L. Sarrao. Nickel deficiency in $RENi_{2x}P_2$ (RE=La, Ce, Pr). Combined crystallographic and physical property studies. *Journal of Solid State Chemistry*, 182(6):1473–1480, jun 2009.

[63] J. G. Bednorz and K. A. Müller. Possible high T_c superconductivity in the Ba-La-Cu-O system. *Zeitschrift für Physik B Condensed Matter*, 64(2):189–193, jun 1986.

[64] Hiroki Takahashi, Kazumi Igawa, Kazunobu Arii, Yoichi Kamihara, Masahiro Hirano, and Hideo Hosono. Superconductivity at 43 K in an iron-based layered compound $LaO_{1-x}F_xFeAs$. *Nature*, 453(7193):376–378, may 2008.

[65] Jian-Tao Han, Jian-Shi Zhou, Jin-Guang Cheng, and John B. Goodenough. A New Pnictide Superconductor without Iron. *Journal of the American Chemical Society*, 132(3):908–909, jan 2010.

[66] Jiangang Guo, Shifeng Jin, Gang Wang, Shunchong Wang, Kaixing Zhu, Tingting Zhou, Meng He, and Xiaolong Chen. Superconductivity in the iron selenide $K_xFe_2Se_2$ ($0 \leq x \leq 1.0$). *Physical Review B*, 82(18):180520, nov 2010.

[67] A. A. Kordyuk. Iron-based superconductors: Magnetism, superconductivity, and electronic structure (Review Article). *Low Temperature Physics*, 38(9):888–899, sep 2012.

[68] H. Fujii, T. Okamoto, T. Shigeoka, and N. Iwata. Reentrant ferromagnetism observed in $SmMn_2Ge_2$. *Solid State Communications*, 53(8):715–717, feb 1985.

[69] G. Venturini, R. Welter, E. Ressouche, and B. Malaman. Neutron diffraction study of $Nd_{0.35}La_{0.65}Mn_2Si_2$: A $SmMn_2Ge_2$-like magnetic behaviour compound. *Journal of Magnetism and Magnetic Materials*, 150(2):197–212, oct 1995.

[70] Vitalij Pecharsky and Peter Zavalij. *Fundamentals of Powder Diffraction and Structural Characterization of Materials*. Springer US, Boston, MA, 2009.

[71] University of London Jeremy Karl Cockcroft, Birkbeck College. $i4/mmm$ symmetry operators, 1999.

[72] Varley F. Sears. Neutron scattering lengths and cross sections. *Neutron News*, 3(3):26–37, 1992.

[73] George M. Sheldrick. Crystal structure refinement with SHELXL. *Acta Crystallographica Section C Structural Chemistry*, 71(1):3–8, jan 2015.

[74] J.W. Lynn, Y. Chen, S. Chang, Y. Zhao, S. Chi, W. Ratcliff II, B.G. Ueland, and R.W. Erwin. Double-Focusing Thermal Triple-Axis Spectrometer at the NCNR. *Journal of Research of the National Institute of Standards and Technology*, 117:60, 2012.

[75] R. W. Cheary and A. Coelho. A fundamental parameters approach to X-ray line-profile fitting. *Journal of Applied Crystallography*, 25(2):109–121, apr 1992.

[76] J A Rodriguez, D M Adler, P C Brand, C Broholm, J C Cook, C Brocker, R Hammond, Z Huang, P Hundertmark, J W Lynn, N C Maliszewskyj, J Moyer, J Orndorff, D Pierce, T D Pike, G Scharfstein, S A Smee, and R Vilaseca. MACS—a new high intensity cold neutron spectrometer at NIST. *Measurement Science and Technology*, 19(3):034023, jan 2008.

[77] Branton J. Campbell, Harold T. Stokes, David E. Tanner, and Dorian M. Hatch. ISODISPLACE : a web-based tool for exploring structural distortions. *Journal of Applied Crystallography*, 39(4):607–614, aug 2006.

[78] P. Hohenberg and W. Kohn. Inhomogeneous Electron Gas. *Physical Review*, 136(3B):B864–B871, nov 1964.

[79] W. Kohn and L. J. Sham. Quantum Density Oscillations in an Inhomogeneous Electron Gas. *Physical Review*, 137(6A):A1697–A1705, mar 1965.

[80] G. Kresse and J. Furthmüller. Efficient iterative schemes for ab initio total-energy calculations using a plane-wave basis set. *Physical Review B*, 54(16):11169–11186, oct 1996.

[81] G. Kresse and J. Furthmüller. Efficiency of ab-initio total energy calculations for metals and semiconductors using a plane-wave basis set. *Computational Materials Science*, 6(1):15–50, jul 1996.

[82] G. Kresse and J. Hafner. Ab initio molecular dynamics for liquid metals. *Physical Review B*, 47(1):558–561, jan 1993.

[83] G. Kresse and J. Hafner. Ab initio molecular dynamics for open-shell transition metals. *Physical Review B*, 48(17):13115–13118, nov 1993.

[84] P. E. Blöchl. Projector augmented-wave method. *Physical Review B*, 50(24):17953–17979, dec 1994.

[85] John P. Perdew, Kieron Burke, and Matthias Ernzerhof. Generalized Gradient Approximation Made Simple. *Physical Review Letters*, 77(18):3865–3868, oct 1996.

[86] Hendrik J. Monkhorst and James D. Pack. Special points for Brillouin-zone integrations. *Physical Review B*, 13(12):5188–5192, jun 1976.

[87] Roald Hoffmann. How Chemistry and Physics Meet in the Solid State. *Angewandte Chemie International Edition in English*, 26(9):846–878, sep 1987.

[88] Simon A J Kimber, Andreas Kreyssig, Yu-Zhong Zhang, Harald O Jeschke, Roser Valenti, Fabiano Yokaichiya, Estelle Colombier, Jiaqiang Yan, Thomas C Hansen, Tapan Chatterji, Robert J. McQueeney, Paul C Canfield, Alan I Goldman, and Dimitri N Argyriou. Similarities between structural distortions under pressure and chemical doping in superconducting $BaFe_2As_2$. *Nature Materials*, 8(6):471–475, jun 2009.

[89] Simon Peschke, Tobias Stürzer, and Dirk Johrendt. $Ba_{1-x}Rb_xFe_2As_2$ and Generic Phase Behavior of Hole-doped 122-Type Superconductors. *Zeitschrift für anorganische und allgemeine Chemie*, 640(5):830–835, apr 2014.

[90] M. V. Sadovskii, E. Z. Kuchinskii, and I. A. Nekrasov. Iron based superconductors: Pnictides versus chalcogenides. In *Journal of Magnetism and Magnetic Materials*, volume 324, pages 3481–3486. Elsevier, oct 2012.

[91] Daniel P Shoemaker, Duck Young Chung, Helmut Claus, Melanie C Francisco, Sevda Avci, Anna Llobet, and Mercouri G Kanatzidis. Phase relations in $K_xFe_{2y}Se_2$ and the structure of superconducting $K_xFe_2Se_2$ via high-resolution synchrotron diffraction. *Physical Review B*, 86(18):184511, nov 2012.

[92] Duanduan Yuan, Ning Liu, Kunkun Li, Shifeng Jin, Jiangang Guo, and Xiaolong Chen. Structure Evolution and Spin-Glass Transition of Layered Compounds $ALiFeSe_2$ (A = Na, K, Rb). *Inorganic Chemistry*, 2(21):13187–13193, nov 2017.

[93] I A Nekrasov and M V Sadovskii. Electronic structure of iron-based superconductors: from pnictides to chalcogenides and other similar systems. *JETP Letters*, 99(10):598–612, jul 2014.

[94] David C Johnston. The puzzle of high temperature superconductivity in layered iron pnictides and chalcogenides. *Advances in Physics*, 59(6):803–1061, 2010.

[95] Johnpierre Paglione and Richard L. Greene. High-temperature superconductivity in iron-based materials. *Nature Physics*, 6(9):645–658, sep 2010.

[96] Yoshikazu Mizuguchi and Yoshihiko Takano. Review of Fe Chalcogenides as the Simplest Fe-Based Superconductor. *Journal of the Physical Society of Japan*, 79(10):102001, oct 2010.

[97] X. H. Niu, S. D. Chen, J. Jiang, Z. R. Ye, T. L. Yu, D. F. Xu, M. Xu, Y. Feng, Y. J. Yan, B. P. Xie, J. Zhao, D. C. Gu, L. L. Sun, Qianhui Mao, Hangdong Wang, Minghu Fang, C. J. Zhang, J. P. Hu, Z. Sun, and D. L. Feng. A unifying phase diagram with correlation-driven superconductor-to-insulator transition for the 122 series of iron chalcogenides. *Physical Review B*, 93(5):054516, feb 2016.

[98] Qimiao Si, Rong Yu, and Elihu Abrahams. High-temperature superconductivity in iron pnictides and chalcogenides. *Nature Reviews Materials*, 1(4):16017, apr 2016.

[99] Guohe Huan, Martha Greenblatt, and K.V. Ramanujachary. Magnetic ordering in metallic $TlCo_{2x}Ni_xS_2$ ($0 \leq x \leq 2.0$) with the $ThCr_2Si_2$ structure. *Solid State Communications*, 71(3):221–228, jul 1989.

[100] Jinhu Yang, Bin Chen, Hangdong Wang, Qianhui Mao, Masaki Imai, Kazuyoshi Yoshimura, and Minghu Fang. Magnetic properties in layered ACo_2Se_2 (A = K, Rb, Cs) with the $ThCr_2Si_2$-type structure. *Physical Review B - Condensed Matter and Materials Physics*, 88(6):064406, aug 2013.

[101] Raquel Lizárraga, Sabina Ronneteg, Rolf Berger, Anders Bergman, Peter Mohn, Olle Eriksson, and Lars Nordström. Theoretical and experimental study of the magnetic structure of $TlCo_2Se_{22}$. *Physical Review B*, 70(2):024407, jul 2004.

[102] Jiming An, A. S. Sefat, D. J. Singh, and Mao-Hua Du. Electronic structure and magnetism in $BaMn_2As_2$ and $BaMn_2Sb_2$. *Phys. Rev. B*, 79:075120, Feb 2009.

[103] Yogesh Singh, M. A. Green, Q. Huang, A. Kreyssig, R. J. McQueeney, D. C. Johnston, and A. I. Goldman. Magnetic order in $BaMn_2As_2$ from neutron diffraction measurements. *Phys. Rev. B*, 80:100403, Sep 2009.

[104] D. C. Johnston, R. J. McQueeney, B. Lake, A. Honecker, M. E. Zhitomirsky, R. Nath, Y. Furukawa, V. P. Antropov, and Yogesh Singh. Magnetic exchange interactions in $bamn_2as_2$: A case study of the J_1-J_2-J_c heisenberg model. *Phys. Rev. B*, 84:094445, Sep 2011.

[105] Xiaofang Lai, Shifeng Jin, Xiao Chen, Tingting Zhou, Tianping Ying, Han Zhang, and Shijie Shen. New layered manganese selenide $KMnAgSe_2$: Structure and properties. *Materials Express*, 4(4):343–348, aug 2014.

[106] M Oledzka, K V Ramanujachary, and M Greenblatt. New Low-Dimensional Quaternary Sulfides $NaCuMS_2$ (M = Mn, Fe, Co, and Zn) with the $CaAl_2Si_2$-Type Structure: Synthesis and Properties. *Chemistry of Materials*, 10(1):322–328, jan 1998.

[107] D. Schmitz and W. Bronger. Zur Kristallchemie einiger Alkalithiomanganate und-zinkate. Mit einer Bemerkung zum $ThCr_2Si_2$. *Zeitschrift fr anorganische und allgemeine Chemie*, 553(10):248–260, oct 1987.

[108] W Bronger, H Hardtdegen, M Kanert, P Müller, and D Schmitz. Alkalimanganselenide und-telluride $A_2Mn_3X_4$–Synthese, Kristall-und Spinstruktur. *Zeitschrift für anorganische und allgemeine Chemie*, 622(2):313–318, 1996.

[109] Pinaki Das, N S Sangeetha, Abhishek Pandey, Zackery A Benson, T W Heitmann, D C Johnston, A I Goldman, and A Kreyssig. Collinear antiferromagnetism in trigonal $SrMn_2As_2$ revealed by single-crystal neutron diffraction. *Journal of Physics: Condensed Matter*, 29(3):035802, 2017.

[110] Stephanie L Brock, J.E. Greedan, and Susan M Kauzlarich. Resistivity and Magnetism of AMn_2P_2 (A = Sr, Ba): The Effect of Structure Type on Physical Properties. *Journal of Solid State Chemistry*, 113(2):303–311, dec 1994.

[111] Stephanie L. Brock, J.E. Greedan, and Susan M. Kauzlarich. A Test of the Application of Extended Hückel Calculations to the $ThCr_2Si_2$ and $CaAl_2Si_2$ Structure Types: the Case of $SrMn_2P_2$ and $BaMn_2P_2$. *Journal of Solid State Chemistry*, 109(2):416–418, apr 1994.

[112] N S Sangeetha, Abhishek Pandey, Zackery A Benson, and D C Johnston. Strong magnetic correlations to 900 K in single crystals of the trigonal antiferromagnetic insulators $SrMn_2As_2$ and $CaMn_2As_2$. *Physical Review B*, 94(9):094417, sep 2016.

[113] Lester Corliss, Norman Elliott, and Julius Hastings. Magnetic Structures of the Polymorphic Forms of Manganous Sulfide. *Physical Review*, 104(4):924–928, nov 1956.

[114] Rémy Tappero, Pierre Wolfers, and Albert Lichanot. Electronic, magnetic structures and neutron diffraction in B1and B3phases of MnS: A density functional approach. *Chemical Physics Letters*, 335(5-6):449–457, mar 2001.

[115] C G Shull, W A Strauser, and E O Wollan. Neutron diffraction by paramagnetic and antiferromagnetic substances. *Physical Review*, 83(2):333–345, jul 1951.

[116] W L Roth. Magnetic structures of MnO, FeO, CoO, and NiO. *Physical Review*, 110(6):1333–1341, jun 1958.

[117] J. M. Hastings, N. Elliott, and L. M. Corliss. Antiferromagnetic Structures of MnS_2 , $MnSe_2$, and $MnTe_2$. *Physical Review*, 115(1):13–17, jul 1959.

[118] R. D. Shannon and C. T. Prewitt. Effective ionic radii in oxides and fluorides. *Acta Crystallographica Section B Structural Crystallography and Crystal Chemistry*, 25(5):925–946, may 1969.

[119] E. E. Rodriguez, P. Zavalij, P. Hsieh, and M. A. Green. Iodine as an Oxidant in the Topotactic Deintercalation of Interstitial Iron in $Fe_{1+x}Te$. *Journal of the American Chemical Society*, 132(29):10006–10008, jul 2010.

[120] P. Zajdel, P. Hsieh, E. E. Rodriguez, N. P. Butch, J. D. Magill, J. Paglione, P. Zavalij, M. R. Suchomel, and M. A. Green. Phase Separation and Suppression of the Structural and Magnetic Transitions in Superconducting Doped

Iron Tellurides, $Fe_{1+x}Te_{1y}S_y$. *Journal of the American Chemical Society*, 132(37):13000–13007, sep 2010.

[121] E. E. Rodriguez, C. Stock, P. Zajdel, K. L. Krycka, C. F. Majkrzak, P. Zavalij, and M. A. Green. Magnetic-crystallographic phase diagram of the superconducting parent compound $Fe_{1+x}Te$. *Physical Review B*, 84(6):064403, aug 2011.

[122] C. Stock, E. E. Rodriguez, M. A. Green, P. Zavalij, and J. A. Rodriguez-Rivera. Interstitial iron tuning of the spin fluctuations in the nonsuperconducting parent phase Fe_{1+x}.Te. *Physical Review B*, 84(4):045124, jul 2011.

[123] E. E. Rodriguez, D. A. Sokolov, C. Stock, M. A. Green, O. Sobolev, Jose A. Rodriguez-Rivera, H. Cao, and A. Daoud-Aladine. Magnetic and structural properties near the Lifshitz point in $Fe_{1+x}Te$. *Physical Review B*, 88(16):165110, oct 2013.

[124] C. Stock, E. E. Rodriguez, O. Sobolev, J. A. Rodriguez-Rivera, R. A. Ewings, J. W. Taylor, A. D. Christianson, and M. A. Green. Soft striped magnetic fluctuations competing with superconductivity in $Fe_{1+x}Te$. *Physical Review B*, 90(12):121113, sep 2014.

[125] X. Zhou, B. Wilfong, H. Vivanco, J. Paglione, C. M. Brown, and E. E. Rodriguez. Metastable Layered Cobalt Chalcogenides from Topochemical Deintercalation. *Journal of the American Chemical Society*, 138(50):16432–16442, dec 2016.

[126] E. E. Rodriguez, C. Stock, K. L. Krycka, C. F. Majkrzak, P. Zajdel, K. Kirshenbaum, N. P. Butch, S. R. Saha, J. Paglione, and M. A. Green. Noncollinear spin-density-wave antiferromagnetism in FeAs. *Physical Review B*, 83(13):134438, apr 2011.

[127] Chang Liu, Takeshi Kondo, Ni Ni, A. D. Palczewski, A. Bostwick, G. D. Samolyuk, R. Khasanov, M. Shi, E. Rotenberg, S. L. Bud'ko, P. C. Canfield, and A. Kaminski. Three- to Two-Dimensional Transition of the Electronic Structure in $CaFe_2As_2$: A Parent Compound for an Iron Arsenic High-Temperature Superconductor. *Physical Review Letters*, 102(16):167004, apr 2009.

[128] Dirk Johrendt and Rainer Pöttgen. Superconductivity, magnetism and crystal chemistry of $Ba_{1x}K_xFe_2As_2$. *Physica C: Superconductivity*, 469(9-12):332–339, may 2009.

[129] J. J. Wu, J.-F. Lin, X. C. Wang, Q. Q. Liu, J. L. Zhu, Y. M. Xiao, P. Chow, and C. Jin. Pressure-decoupled magnetic and structural transitions of the parent compound of iron-based 122 superconductors $BaFe_2As_2$. *Proceedings of the National Academy of Sciences*, 110(43):17263–17266, oct 2013.

[130] E. E. McCabe, C. Stock, E. E. Rodriguez, A. S. Wills, J. W. Taylor, and J. S. O. Evans. Weak spin interactions in Mott insulating $La_2O_2Fe_2OSe_2$. *Physical Review B*, 89(10):100402, mar 2014.

[131] Yogesh Singh, A. Ellern, and D. C. Johnston. Magnetic, transport, and thermal properties of single crystals of the layered arsenide $BaMn_2As_2$. *Physical Review B*, 79(9):094519, mar 2009.

[132] M. Ramazanoglu, A. Sapkota, A. Pandey, J. Lamsal, D.L. Abernathy, J.L. Niedziela, M.B. Stone, R. Salci, D.A. Acar, F.O. Oztirpan, S. Ozonder, A. Kreyssig, A.I. Goldman, D.C. Johnston, and R.J. McQueeney. Heisenberg model analysis on inelastic powder neutron scattering data using parent and K doped $BaMn_2As_2$ samples. *Physica B: Condensed Matter*, 551:51–59, dec 2018.

[133] Abhishek Pandey, R. S. Dhaka, J. Lamsal, Y. Lee, V. K. Anand, A. Kreyssig, T. W. Heitmann, R. J. McQueeney, A. I. Goldman, B. N. Harmon, A. Kaminski, and D. C. Johnston. $Ba_{1x}K_xMn_2As_2$: An Antiferromagnetic Local-Moment Metal. *Physical Review Letters*, 108(8):087005, feb 2012.

[134] D. E. McNally, J. W. Simonson, J. J. Kistner-Morris, G. J. Smith, J. E. Hassinger, L. DeBeer-Schmitt, A. I. Kolesnikov, I. A. Zaliznyak, and M. C. Aronson. $CaMn_2Sb_2$: Spin waves on a frustrated antiferromagnetic honeycomb lattice. *Physical Review B*, 91(18):180407, may 2015.

[135] Q. D. Gibson, H. Wu, T. Liang, M. N. Ali, N. P. Ong, Q. Huang, and R. J. Cava. Magnetic and electronic properties of $CaMn_2Bi_2$: A possible hybridization gap semiconductor. *Physical Review B*, 91(8):085128, feb 2015.

[136] W. Ratcliff II, A.L. Lima Sharma, A.M. Gomes, J.L. Gonzalez, Q. Huang, and J. Singleton. The magnetic ground state of. *Journal of Magnetism and Magnetic Materials*, 321(17):2612–2616, sep 2009.

[137] C.A. Bridges, V.V. Krishnamurthy, S. Poulton, M.P. Paranthaman, B.C. Sales, C. Myers, and S. Bobev. Magnetic order in $CaMn_2Sb_2$ studied via powder neutron diffraction. *Journal of Magnetism and Magnetic Materials*, 321(22):3653–3657, nov 2009.

[138] V.V. Bannikov, I.R. Shein, and A.L. Ivanovskii. Trends in structural, electronic properties and Fermi surface topology of 15 tetragonal $ThCr_2Sir_2$-type phases $AFer_2Chr_2$, where A=Li, Na, K, Rb, and Cs; Ch=S, Se, and Te, as parent systems of new ternary ironchalcogenide superconductors. *Computational Materials Science*, 60:1–6, jul 2012.

[139] Carlos Mujica, Jaime Páez, and Jaime Llanos. Synthesis and crystal structure of layered chalcogenides [$KCuFeS_2$ and $KCuFeSe_2$]. *Materials Research Bulletin*, 29(3):263–268, mar 1994.

[140] Hechang Lei, Emil S. Bozin, Kefeng Wang, and C. Petrovic. Antiferromagnetism in semiconducting $KFe_{0.85}Ag_{1.15}Te_2$ single crystals. *Physical Review B*, 84(6):060506, aug 2011.

[141] Fan Sun, Zhongnan Guo, Ning Liu, Kun Lin, Da Wang, and Wenxia Yuan. $KFeCuTe_2$: a new compound to study the removal of interstitial Fe in layered tellurides. *Dalton Transactions*, 46(11):3649–3654, 2017.

[142] Junbao He, Yu Fu, Yumin Leng, Benyuan Ma, Xuyan Liu, Xiaoxu Ji, Aihua Wang, Chunhua Ma, Xiaohua Zhao, Yawen Hu, Zhiwen Lu, Dawei Zhou, and Ping Zhang. Transport and Magnetic Properties of $K_{0.8}Fe_{2x}$ Cu_x $Se_2(0$ x $2)$ System. *Journal of Superconductivity and Novel Magnetism*, 28(1):219–222, jan 2015.

[143] Bianbian Wang, Zhongnan Guo, Fan Sun, Jun Deng, Jiawei Lin, Dan Wu, and Wenxia Yuan. The transition between antiferromagnetic order and spin-glass state in layered chalcogenides $KFeAgCh_2$ (Ch = Se, S). *Journal of Solid State Chemistry*, 272:126–130, apr 2019.

[144] Jaime Llanos, Antonio Buljan, Carlos Mujica, and Rafael Ramírez. Electron transfer and electronic structure of $KCuFeS_2$. *Journal of Alloys and Compounds*, 234(1):40–42, feb 1996.